Risk Assessment using Image-Based Hemodynamic Modeling of Patients with Coronary Artery Aneurysms caused by Kawasaki Disease

Sengupta, Dibyendu

2013

UNIVERSITY OF CALIFORNIA, SAN DIEGO

Risk Assessment using Image-Based Hemodynamic Modeling of Patients with Coronary Artery Aneurysms caused by Kawasaki Disease

A dissertation submitted in partial satisfaction of the requirements for the degree of Doctor of Philosophy

in

Engineering Sciences (Mechanical Engineering)

by

Dibyendu Sengupta

Committee in charge:

Professor Alison L. Marsden, Chair
Professor Jane C. Burns
Professor Andrew M. Kahn
Professor Sutanu Sarkar
Professor Juan C. Lasheras
Professor Geert W. Schmid-Schoenbein

2013

The Dissertation of Dibyendu Sengupta is approved and it is acceptable in quality and form for publication on microfilm and electronically:

Chair

University of California, San Diego
2013

DEDICATION

This Dissertation is dedicated to my parents, Mr. Subhas Sengupta and Mrs. Debjani Sengupta whose tremendous suppor0t and sacrifice have helped me achieve my goals.

TABLE OF CONTENTS

LIST OF FIGURES

LIST OF TABLES

ACKNOWLEDGMENTS

This research would not have been possible without the support and guidance of my advisor, Professor Alison Marsden. She has always been believed in me and motivated me during various challenging phases of the project. Her scientific outlook, innovative ideas and rational approach towards solving a complicated engineering problem have taught me how to tackle complex research projects in an effective manner without getting overwhelmed. I particularly appreciate the patience and trust that she offered when I was exploring new ideas and principles. Whenever I was stuck with a research problem, her sharp intuitions and intelligent research ideas have helped me solve it in an efficient manner. I am truly indebted to Professor Marsden for helping me enrich my knowledge in engineering and science and advising me in the right direction.

Professor Jane Burns has also been instrumental for the success of this project. Without her, it would have been impossible for me to enter the medical community from a completely engineering background. She helped me understand various biological challenges. Her enthusiasm towards using various computational tools to solve problems in medicine has ensured that the gap between the two communities can be easily bridged.

I am also greatly thankful to Dr. Andrew Kahn who has advised me throughout this project. His insightful thoughts about the simulation methods and assumptions have been crucial in making this project a success. His expertise in the field of medical imaging also added a new dimension to this research. I learnt a lot through the various discussions with Dr. Kahn.

In addition, I greatly appreciate the contributions and the time commitment of my other committee members, Professor Juan Lasheras, Professor Sutanu Sarkar and Professor Geert Schmid-Schoenbein. The class in Continuum Mechanics taught by Professor Lasheras laid the foundation in mechanics while the CFD class taught by Professor Sarkar provided deep insights into the numerical methods for solving various computational problems in my first year of graduate school. I also wanted to thank both Professor Lasheras and Professor Sarkar for their constant encouragements whenever I met them.

I would also like to thank all of my present and past labmates for making the days in graduate school a fun as well as a learning experience. In particular, I wanted to thank Dr. Sethuraman Sankaran for the discussions about the implementation of the lumped parameter boundary conditions and Dr. Weiguang Yang for the discussions regarding Simvascular. Furthermore, I wanted to thank my other labmates Mahdi Esmaily Moghadam, Chris Long and Abhay Ramachandra for the various discussions about linear solver, finite elements and

simulations methods. I also appreciate the help provided by Dr. Hyun Jin Kim with the coronary simulations, Dr. Shawn Shadden with his expertise on particle tracking simulations and Dr. Nathan Wilson for the questions regarding Simvascular. This project was supported by the funding provided by NIH R21 grant (Grant Number – HL102596A).

Finally, I would like to thank my beloved wife Sreeparna for supporting me during the various difficult phases of graduate school. Her constant encouragements and humor comforted me through the nervous moments and helped me stay focused throughout my graduate studies.

VITA

2008	Bachelor and Master of Technology (Dual Degree), Aerospace Engineering, Indian Institute of Technology, Kharagpur
2008-2009	Department Fellowship, Mechanical and Aerospace Engineering Department
2009	Master of Science, Engineering Sciences (Mechanical Engineering) University of California, San Diego
2009-2010	Interdisciplinary collaboratories fellowship to carry out research in collaboration with Mechanical and Aerospace Engineering and the Medical School at University of California, San Diego
2009-2010	Howard Hughes Medical Institute (HHMI) Fellowship for applying engineering techniques to medicine
2010-2013	Research Assistant, Department of Mechanical and Aerospace Engineering, University of California, San Diego
2013	Doctor of Philosophy, Engineering Sciences (Mechanical Engineering) University of California, San Diego

PUBLICATIONS

Sengupta D., Burns J. C., Kahn A. M., Sankaran S., Shadden S. C., Marsden A. L., “Image-based modeling of hemodynamics in coronary artery aneurysms caused by Kawasaki disease”, BMMB, November, 2011.

Sengupta D., Kahn A. M., Shirinsky O., Lyskina G. A., Burns J. C., Marsden A. L., “Thrombotic risk stratification using computational modeling in patients with coronary artery aneurysms following Kawasaki disease”, Circulation Journal, in review.

SELECTED PRESENTATIONS

Sengupta D., Kahn A. M., Burns J. C., Marsden A. L., “Image-based modeling of hemodynamics in coronary aneurysms caused by Kawasaki disease”, ASME Summer Bioengineering Conference, 2011, Farmington, PA, USA.

Sengupta D., Kahn A. M., Burns J. C., Marsden A. L., “Patient specific hemodynamic simulations in coronary artery aneurysms caused by Kawasaki disease”, ASME Summer Bioengineering Conference, 2010, Naples, FL, USA.

Sengupta D., Kahn A. M., Burns J. C., Marsden A. L., “Exposure time computations performed on a patient with coronary artery aneurysms”, Meeting on Congenital Heart Disease, 2010 La Jolla, CA,

Sengupta D., Marsden A. L., “A computational investigation of Murray’s Law using derivative free optimization”, ASME Summer Bioengineering Conference, 2009, Squaw Valley, CA.

ABSTRACT OF THE DISSERTATION

Risk Assessment using Image-Based Hemodynamic Modeling of Patients with Coronary Artery Aneurysms caused by Kawasaki Disease

by

Dibyendu Sengupta

Doctor of Philosophy in Engineering Sciences (Mechanical Engineering)

University of California, San Diego, 2013

Professor Alison L. Marsden, Chair

Kawasaki Disease (KD) is the leading cause of acquired heart disease in children and can result in life-threatening coronary artery aneurysms in up to 25% of patients. These aneurysms put patients at risk of thrombus formation, myocardial infarction and sudden death. Clinicians must therefore decide which patients should be treated with anticoagulant medication and/or surgical and percutaneous intervention. Current recommendations regarding initiation of anticoagulant therapy are based on anatomy alone with historical data suggesting that patients with aneurysms ≥ 8mm in diameter are at highest risk of thrombosis. Given the multitude of variables that influence thrombus formation, we postulate that hemodynamic data derived from patient-specific blood flow simulations will better predict the risk of thrombosis than maximum diameter alone.

Firstly, a finite element framework with a lumped parameter boundary condition was implemented following a circuit analogy. A patient-specific case study was carried out to study the abnormalities in hemodynamics arising due to the presence of the aneurysms in the coronary arteries. Furthermore, simulations were performed on a virtual normal control model created from the same CT image data to demonstrate order of magnitude variation of several local hemodynamic quantities despite no differences in global flow and pressure waveforms between the two models.

Secondly, blood flow simulations were performed on patient-specific models on a cohort of KD patients with coronary aneurysms and one KD patient with no coronary aneurysms. Key hemodynamic quantities including shear stress and residence times were computed in addition to geometric parameters and compared to the corresponding values in the normal vessels with no aneurysms. The findings uncovered various non-intuitive relationships between the flow parameters and geometry relating to the risk of thrombosis. The study suggested that a clinical risk index based on simulation and geometric data could be used to select patients for anticoagulant therapy.

To our knowledge, we performed the first cardiovascular simulations for KD patients with coronary aneurysms. This thesis lays the framework for the construction of a simulation based clinical risk index by considering a larger cohort of patient data that may be clinically useful in patient management for KD patients with coronary aneurysms.

Chapter 1

1. Introduction

1.1 Motivation

Kawasaki Disease is an acute self limited vasculitis occurring primarily in children less than 5 years of of age[1]. KD is the leading cause of acquired heart disease in children[2]. Each year over 5500 cases of KD are diagnosed in the US alone[2]. Japan has the highest incidence of KD in the world with 1 in every 185 children affected by the disease[3]. The symptoms of KD evolve over the first 10 days of illness. It is challenging to diagnose patients with Kawasaki Syndrome quickly and often the patients are not diagnosed within the first 10 days of fever onset[4]. Coronary artery aneurysms occur in about 20-25% of the untreated cases[5]. The number is however reduced to about 3-5% by the application of Intravenous Immunoglobulin (IVIG)[6] within the first 10 days of fever onset.

There are currently very limited clinical data to aid clinicians in the treatment of patient with coronary artery aneurysms caused by KD. KD patients with coronary artery aneurysms are at increased risk of thrombus formation and myocardial infarction, heart failure and death[7]. Long term patient management of KD patients with regards to antiplatelet therapy, systemic anticoagulation, percutaneous intervention such as stenting, rotational ablation and coronary artery bypass surgery is challenging[8]. Moreover, the vasculopathy of the young adults with coronary artery aneurysms caused by KD is markedly different from that of other atherosclerotic diseases. So the traditional patient management for treating atherosclerotic diseases does not apply for KD patients with aneurysms. Since most patients with KD are otherwise healthy, clinicians are faced with the difficult choice of exposing patients to treatment risks, or waiting and watching, knowing that a sudden adverse cardiac event may have serious or even deadly consequences.

Current AHA guidelines for anticoagulation therapy in KD patients with coronary aneurysms are only based on the aneurysm diameter. The guidelines are based on Level of Evidence C (expert opinions, case studies or standard of care)[8]. According to the guidelines, patients with giant aneurysms (aneurysm diameter > 8mm) are treated with systemic anticoagulation[9]. However, for patients with coronary aneurysms less than 8mm in diameter, the treatment is less straightforward. The current guidelines do not take into account the hemodynamic features associated with KD patients with coronary aneurysms. As a result, these guidelines may cause either undertreatment of patients with coronary aneurysmal diameters less than 8mm or over aggressive treatment of those with diameters more than 8mm. We hypothesize that analysis of flow features inside coronary aneurysms have the potential to reveal quantitative, and often non-intuitive hemodynamic characteristics that cannot be obtained from standard clinical imaging modalities.

Computer simulations of patient-specific hemodynamics have advanced greatly in recent years. Various sophisticated computational methods are proving to be useful both as diagnostic as well as analysis purposes for adult and pediatric cardiovascular disease. Simulations provide a means to obtain crucial hemodynamic information, which cannot be easily obtained from conventional imaging modalities. Some critical hemodynamic quantities such as recirculation times[10], flow distributions in blood vessels[11], optimization of surgical grafts[12, 13] are currently only possible to obtain using simulation methods since they are not obtainable from standard imaging modalities. Further, these techniques can be performed using completely non-invasive procedures, which makes them more powerful.

Despite recent advances, computational methods suffer from various drawbacks including several assumptions of the model. Advancements in the field of computing has enabled more realistic calculations by incorporating more complicated mathematical models into the computational methods. Blood flow simulations on patient-specific models have the ability to extract clinically relevant hemodynamic information that assist clinicians in performing virtual surgical optimization[11], design patient-specific optimal ventricular assist device[14], patient-specific simulation of blood flow in coronary artery bypass grafts[15], blood flow simulations in abdominal aortic aneurysms[16] as well as cerebral aneurysms[17].

Despite rapid strides in computational simulations there has been little effort to use these technology on KD patients with coronary aneurysms. There is significant potential to apply modern computational tools to aid clinicians in a better patient management for KD patients with coronary aneurysms. This thesis focuses on using state of the art computational and numerical methods to perform patient-specific modeling of KD patients with coronary aneurysms in order to understand the role of hemodynamics in thrombotic risk.

1.2 Prior Work on Blood Flow Simulations

This subsection primarily describes the sate of the art computational models that are presently employed in the cardiovascular system with a special emphasis on the models relating to the coronary vasculature.

The human circulatory system consists of a complex network of arteries, arterioles, veins and capillaries that supply oxygenated blood and nutrition to all parts of the human body and remove deoxygenated blood and excretory wastes from various parts of the human body. Blood flowing through this complex network of blood vessels is driven by a central pumping chamber – the human heart. From the point of view of physics, simulation of blood flow through this complex network of blood vessels is challenging due to the following reasons

i) There is a large variation of Reynold’s number. For example, as the blood flows from the arteries such as the aorta to the capillaries there is several order of magnitude change in the Reynold’s Number.

ii) The wall of the blood vessels is compliant. CFD simulations assuming rigid wall may not yield accurate results, as they do not account for wave propagation or reflection, and more sophisticated coupled-fluid structure formulations need to be employed.

iii) Patient specific modeling typically leads to the truncation of several smaller vessels that needs to be modeled by sophisticated boundary conditions to model the downstream vascular network.

1.2.1 Lumped Parameter Model

Boundary conditions are of paramount importance in blood flow simulations. The patient-specific models that are use in blood flow simulations usually do not include many of the smaller vessels including the capillaries that cannot be clearly observed in a clinical scan (MR or X-Ray CT). In such situations approximations need to be made by using reduced order mathematical models that can mimic the influence of the smaller vessels. These mathematical models lump a group of smaller vessels into a model equation, and are called lumped parameters models. Lumped parameter models serve as the boundary condition for the blood flow simulations. While the lumped parameter models were based on a circuit analogy, there are other approaches in the blood flow simulations. Some of the particularly important methods include the usage of one dimensional non-linear wave propagation method[18] and the effective implementation of the impedance boundary condition that can capture the flow and pressure waves in the arterial tree[19].

Lumped parameter models are based on the analogy between an electrical circuit system and pressure driven flow system. Similar to electrical systems, which consist of voltage sources, resistances, capacitances and inductances, a pressure driven flow inside the human circulatory system can also be modeled with these components. In this context, the pressure plays the role of the voltage driving the flow rate, which is analogous to the flow of current. The resistances model the dissipative forces, the capacitance models compliance of vessel wall while inductance models the inertial effects in the simulation.

Typically the smaller vessels contribute to the high downstream resistance, which are implemented as a boundary condition in the CFD framework using the equation $P = QR$ where P is the outlet pressure, Q is the flow at the outlet and R is the downstream resistance. While, the capacitance modeling the compliance of the vessels relates the pressure to the flow in the following manner $dP/dt = Q/C$ where C represents the modeled capacitance of the vessel. Finally, the inductance modeling the inertial effects is relates the pressure to the flow rate as $P = L\ dQ/dt$ where L is the inductance of the vessel. Using the lumped parameter formulation, the entire domain is decomposed into a computational domain and an analytic domain as shown in Figure 1.1. The 3D computational domain where the Navier-Stokes equations are solved is coupled to the analytic 0D domain through the boundary interface of the computational domain as shown in the figure. The lumped parameter network is applied in the analytic 0D domain and the entire coupled formulation is solved using a stabilized finite element method[19, 20]. Using the lumped parameter boundary condition one can generate physiologic flow and pressure waveforms[21-23].

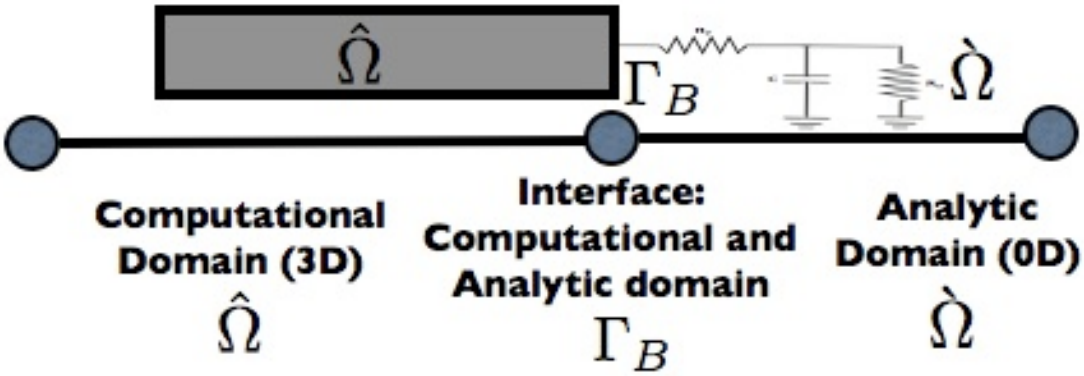

Figure 1.1: Coupled multidomain formulation where the 3D computational domain is coupled to the 0D analytic domain through the boundary surface

One of the most frequently used lumped parameter models is the Windkessel lumped parameter model which was developed to identify the afterload of the heart[24] and model the downstream resistance and compliance of the blood vessels[25]. All arteries are compliant vessels and the is usually modeled by a capacitance of the Windkessel model while the resistance of the downstream vessels including that of the capillaries are modeled by a resistance. The three element Windkessel model has been used in this study to model the boundary conditions of various arterial outlets. The three element Windkessel model comprises of a proximal resistance, a capacitance and a distal resistance[25]. A typical three-element Windkessel RCR boundary condition circuit is shown in Figure 1.2 which consists of a proximal resistance R_P, a distal resistance R_D and a capacitance C. The relationship between pressure and flow rate for the RCR circuit is obtained by solving an ODE and is given as follows where Q(t) represents the flow and P(t) represents the pressure at the outlet of the RCR circuit.

$$P(t) = [P(0) - R_P Q(0)]e^{-\frac{t}{R_D C}} + R_P Q(t) + \int_0^t \frac{e^{-\frac{t-\tilde{t}}{R_D C}}}{C} Q(\tilde{t}) d\tilde{t}$$

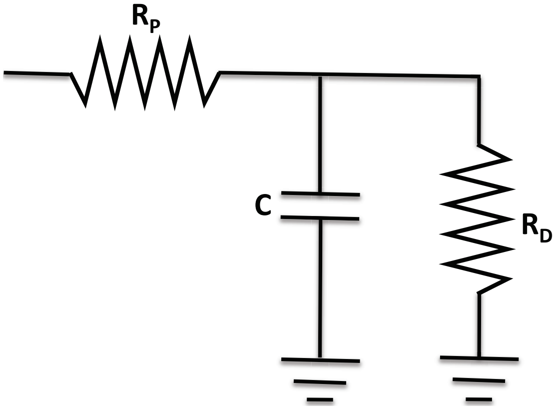

Figure 1.2: Typical Windkessel RCR circuit

Lumped parameter models that are used in cardiovascular simulations have also validated through in-vivo experiments[26] to predict global cardiovascular features. Furthermore, the impedance of the arterial tree has been modeled in previous research[27]. Simulations with the help of lumped parameter models has also enabled the optimization of grafts which are essential in Fontan surgery[13, 28]. Such boundary conditions have the potential to be optimized effectively under patient specific conditions to match clinical parameters.

1.2.2 Lumped Parameter Heart Model

The human heart is a complex pump triggered by electrical and mechanical responses and is the source of systemic and venous circulation. A significant research effort has been made to develop reduced order mathematical models to mimic the actins of the human heart.

Lumped parameter heart models were first motivated by the canine studies[29, 30] done to estimate the normalized elastance function of the heart. The normalized elastance function estimates the ventricular contraction and relaxation. The elastance function is normalized based on the maximum elastance value and the time between the onset of systole and diastole.

Furthermore, it was observed that the normalized elastance function for all the hearts collapses into a single curve. Using the normalized elastance the ventricular pressure can be obtained as a function of the ventricular volume. Furthermore, it was also shown in a later study that a similar behavior exists for the human heart with the normalized elastance function having the same form for a wide range of human hearts[31].

A lot of efforts have been made towards the development of a lumped parameter heart model for the human heart. Recent work by Kim et al[32] provided a lumped parameter model for the human heart inspired by studies done on canine by considering the interactions of the heart with the systemic and venous circulation[33]. These lumped parameter models include the resistance and inductances that can model the viscous and intertial effects as well.

1.2.3 Lumped Parameter Coronary Vasculature Model

The coronary circulation is closely linked to the contraction of the human heart. The coronary arteries supply oxygenated blood and nutrition to the heart muscles (the myocardium). So a healthy coronary artery is of extremely important for the heart to function properly. The coronary flow is influenced by the systemic circulation caused by the pumping action of the heart as well as the contraction and the relaxation of the myocardium.

Modeling coronary arteries presents particular challenges that are not readily addressed with standard simulation methods. Standard simulation boundary conditions, such as resistance, cannot capture coronary flow and pressure behavior, in which flow and pressure are out of phase. This effect is particularly significant in the left coronary artery (LCA). During systole, the resistance of the coronary bed increases and restricts blood flow through the LCA. During diastole, coronary resistance decreases, and blood flow is maximized. While, in principle, it is possible to model this phenomenon with time-varying impedance boundary conditions, a lack of information on the patient-specific coronary waveform makes the impedance spectrum difficult to obtain. In recent work, novel lumped parameter boundary conditions were developed for modeling coronary flow together with a coupled lumped parameter heart model, which we build upon in the present study.[34]

Numerous reduced order mathematical models have been developed to study the interaction of coronary arteries and the cardiac muscles. One of the most effective means of modeling the coronary circulation is through the usage of the intermyocardial pumps. The varying elastance models are used to compute the intermyocardial pressures that are provide the impedance caused in the coronary flow during systole[35]. This model was able to explain the relationship between pressure and flow in a coronary vasculature. This model has been adopted by many researchers to compute the global flow features in the coronary arteries[36-38].

Patient-specific modeling of KD patients with aneurysmal coronary arteries needs to have a robust framework for simulating the coronary circulation. Blood flow simulations in such three-dimensional model appropriate boundary conditions for the simulation to serve as a good predictive model. Furthermore, appropriate lumped parameter models need to be employed as the boundary conditions for such simulations, which is crucial for a good hemodynamic prediction. Kim et al.[34] have developed a technique to couple the complex interaction of the coronaries with cardiac impedance as well as the arterial impedance by the usage of a lumped parameter heart model. This work has been built based on such boundary conditions. However, in this work the parameters for such boundary conditions were computed on a patient specific basis, which may provide a basis for an effective clinical tool in future work.

1.2.4 Blood Flow simulations in three dimensions

Computational solutions of the Navier Stokes equations have evolved as a powerful tool to study the complex blood flow patterns in the cardiovascular system. A significant research effort has been directed towards bridging the gap between engineering and medicine. Simulation methods provide means to compute flow features that cannot be readily obtained experimentally or by traditional imaging modalities.

Computer simulations of hemodynamics in patient-specific geometries have advanced in recent years and are now being widely used in the study of cardiovascular disease. Hemodynamic quantities such as flow distribution, wall shear stress, particle residence times, and exercise conditions can be easily obtained from simulations. Simulations have played a key role in the study of congenital heart defects,[12, 39, 40] abdominal and cerebral aneurysms,[16, 41] and bypass grafts[42].

1.2.5 Equations for Blood Flow Simulations

The blood flow simulations are governed by the Navier Stokes Equation. Rigid wall assumption was assumed in the simulations. Moreover, blood can be considered as a Newtonian or Non-Newtonian fluid depending on the physics of the flow. The flow conditions in the systemic circulation causes high shear rates in the larger arteries such as the aorta. Under such flow conditions, blood is generally treated as a Newtonian fluid[43]. However, in the small arterioles and the capillaries blood should not be treated as a Newtonian fluid.

The three dimensional blood flow equations consists of the momentum balance and mass balance equations for an incompressible fluid. These equations need to be solved with suitable boundary and initial conditions. The boundary Γ of the spatial domain Ω is split into a Dirichlet boundary condition Γ_g and Neumann boundary condition Γ_h. The following represent the momentum and continuity equations

$$\rho \vec{v_{,t}} + \rho \vec{v} \cdot \nabla \vec{v} = -\nabla p + div(\tilde{\tau}) + \vec{f} \qquad (1.1)$$

$$div(\vec{v}) = 0 \qquad (1.2)$$

$$\vec{v}(\vec{x},t)=\vec{g}(\vec{x},t) \text{ where } \vec{x}\in\Gamma_g \tag{1.3}$$

where $\tilde{\tau}=2\mu\tilde{D}$ with $\tilde{D}=\frac{1}{2}(\nabla\vec{v}+\nabla\vec{v}^T)$

$$\vec{t}_{\vec{n}}=[-p\tilde{I}+\tilde{\tau}]\cdot\vec{n}=\vec{h}(\vec{v},p,\vec{x},t) \text{ where } \vec{x}\in\Gamma_h \tag{1.4}$$

$$\vec{v}(\vec{x},0)=\vec{v}_0(\vec{x}) \text{ where } \vec{x}\in\Omega \tag{1.5}$$

This set of equations is solved to obtain the fluid velocity and pressure distribution. Simulations of blood flow in patient specific geometric models has been proven to be a powerful tool in predicting outcomes of surgery[15, 40, 44] as well as in planning alternate treatment strategies[11, 45].

Computational fluid dynamics techniques have not been previously applied to KD patients with coronary aneurysms. Analyzing the hemodynamics using these state of the art computational methods may now open up new horizons for better patient management of KD al patients with coronary aneurysms. Clinicians currently rely on basic geometric measurements such the aneurysmal diameters to make decisions about patient treatment with anticoagulation therapy. In the absence of evidence-based guidelines for patient management, these computational tools may be able to provide clinicians with additional, often non-intuitive information relating to flow features. The risk of thrombosis in the KD patients is influenced by hemodynamics in addition to the geometry. Our driving hypothesis is that hemodynamics may provide additional means to quantify patient risk of thrombosis, through correlations between simulations and hemodynamic data.

Chapter 2

2. Image-based modeling of hemodynamics in coronary artery aneurysms caused by Kawasaki disease

2.1 Introduction

In this chapter, we present the first patient-specific computational simulations of blood flow in a subject with KD using physiologic boundary conditions and a patient-specific model of the aorta and coronary arteries. The downstream boundary condition takes into account the coronary microcirculation and myocardial contractility via a lumped parameter model. We measured the effect of local geometry on velocity patterns, wall shear stress (WSS), oscillatory shear index (OSI) and particle residence times, each of which are postulated to strongly affect the propensity for thrombus formation. By creating a patient-specific virtual control model, we also quantitatively compare and contrast hemodynamics in the aneurysmal and normal coronary artery.

While aneurysms can be imaged to obtain anatomical information, there are currently no available clinical tools to predict the risk of coronary artery thrombosis or myocardial infarction. Imaging flow in the coronary arteries non-invasively using phase contrast magnetic resonance imaging (MRI) is possible, but is technically challenging because the coronary arteries are small and mobile, with maximum displacements in the right and the left coronary arteries of about 16mm and 10mm respectively.[46, 47] CT angiography can now be performed with relatively low radiation doses to non-invasively image coronary artery anatomy,[48] but provides no hemodynamic information. Despite evidence that hemodynamics, including wall shear stress and flow stagnation, are closely linked to inflammation and risk of thrombosis, clinical decisions are currently typically made based on anatomy alone.

This work builds upon recent advances in simulation technology, including sophisticated lumped parameter boundary conditions,[23, 49, 50] increasing anatomic realism,[39] particle tracking,[10] and virtual surgery optimization.[45] Special coronary boundary conditions were applied in conjunction with the heart model to model the flow and pressure in the coronaries[32, 34, 51]. We also quantify the effects of flow recirculation in the aneurysm by computing particle residence times at locations along both coronary arteries.[52]

In this study we quantified hemodynamic parameters of likely clinical relevance for assessing the thrombotic risk in a patient with KD, using anatomic data obtained by multi-detector computed tomography (CT). From simulation results, we obtained the first detailed quantitative, time-dependent values of shear stress and residence times using realistic flow conditions in a coronary aneurysm caused by KD. We created a virtual control model by artificially constructing a model of normal coronary anatomy for the same patient to compare normal and pathological hemodynamics.

2.2 Methods

2.2.1 Subject data

The subject suffered KD at the age of 3 yrs. and developed giant coronary artery aneurysms. Anatomic data were obtained from a clinically-indicated CT angiogram (64-slice CT General Electric), acquired in 2006 when the patient was 10 years old. The patient has been maintained on warfarin with therapeutic INR between 2.0-2.5 and aspirin (81 mg/day). He currently has no ischemic symptoms. This study was approved by the Institutional Review Board at UCSD, and written subject assent and parent consent were obtained for the imaging and simulation studies.

2.2.2 Model Construction

Four steps were performed to construct patient specific three-dimensional geometric models from CT image data. These steps were: 1) creation of centerline paths in each vessel of interest, 2) segmentation of the vessel lumen using 2D level set methods, 3) lofting the 2D segmentations to create a solid model of the desired vasculature and 4) meshing of the solid model using unstructured tetrahedral mesh for use in the finite element flow solver. Models are created using a customized version of the open sourced Simvascular software package[53] (simtk.org).

A virtually healed control case was created by replacing the aneurysmal regions with normal coronary geometry, keeping the rest of the anatomy unchanged. This allowed for direct comparison of hemodynamic changes between the normal and pathological states. As the aneurysm was located in the proximal coronary region, normal coronary diameters for this patient were determined assuming Z-score (normalized diameter) values of 0 and using the body surface area (BSA) of the patient based on the following regression equations.[54]

$$\begin{aligned}
\text{LMCA} &= 0.31747 \cdot (\text{BSA}^{0.36008}) - 0.02887 \\
\text{pLAD} &= 0.26108 \cdot (\text{BSA}^{0.37893}) - 0.02852 \\
\text{pRCA} &= 0.26117 \cdot (\text{BSA}^{0.39992}) - 0.02756
\end{aligned}$$

where LMCA, pLAD and pRCA represent the left main coronary artery, proximal left anterior descending coronary artery and proximal right coronary artery, respectively. The above relations were used to prescribe the diameter of the normal coronaries approximately 3-4 cm distal to the ostia. Linear interpolation was used to taper the vessels between this point and normal region distal to the aneurysm. The arch anatomy and coronary geometry distal to the aneurysms were left unchanged and only the diameter of the proximal aneurysmal regions were changed to the corresponding normal values. The maximum diameters in the aneurysmal regions of the KD model were 1.14 cm in the LAD and 1.08 cm in the RCA, which were almost 3 times the normal values.

2.2.3 Simulation Methods

A finite element mesh was constructed for each model using the commercial software Meshsim (Symmetrix, Inc, Troy, NY). Adaptive meshing was used based on the Hessian of the velocity field, with a minimum mesh size of 0.2mm to ensure mesh convergence of the solutions.[55] Resulting meshes had over 3.5 million elements for both the normal and the KD model. Simulations were run for 6 cardiac cycles until the pressure fields at the inlet and outlet did not change more than 1% from the previous cycle. Simulations of 6 cardiac cycles took about 26 hours to complete on 60 processors. A custom stabilized 3-D finite element Navier-Stokes solver was used following our previous work.[25] The fluids solver and boundary conditions we employ have been thoroughly validated in prior work through *in vitro* experiments using rigid and compliant physical phantoms, with abdominal aortic aneurysm, patent thoracic artery, and stenotic thoracic artery geometries. Results have shown good agreement between numerically simulated and experimentally measured velocity fields and pressure waveforms in rigid and deformable geometries.[56, 57]

Blood was modeled as a Newtonian fluid with a density of 1.06gm/cc and dynamic viscosity of 0.04 dynes/sq cm for all simulations. We assumed the walls to be rigid in all cases. A time step size of 1ms was chosen to satisfy the stability condition.[58] In order to prevent divergence due to backflow at the outlets of the model, additional stabilization terms were used at the outlet nodes in the fluid solver[14, 59] acting only during periods of flow reversal.

2.2.4 Boundary Conditions

Coronary artery downstream boundary conditions are crucial for modeling the physiology of the coronary circulation and microcirculation. Coronary boundary conditions are applied at each coronary outlet of the model, and standard RCR (Windkessel) boundary conditions[60] are applied at the outlets of the aorta and branch vessels. Details of the boundary conditions and their implementations are described below.

2.2.5 Inlet Boundary Condition

A typical aortic waveform is applied at the inlet of the aorta (Figure 2.1), as a Dirichlet boundary condition. The flow waveform is scaled to match the cardiac output and the heart rate of the patient obtained from echocardiographic and clinical data.

2.2.6 Coronary Boundary Conditions

Blood flow at the inlet to the coronaries is driven by a combination of the aortic pressure and downstream coronary resistance. However, during systole, the distal coronary resistance increases substantially due to increasing intra-myocardial pressure resulting from the contraction of the heart. The intra-myocardial pressure depends on the aortic flow and ventricular pressures. Hence, there is a complex interaction between the flow at the coronary outlets and the aortic flow at the inlet, which must be captured accurately by the numerical model.

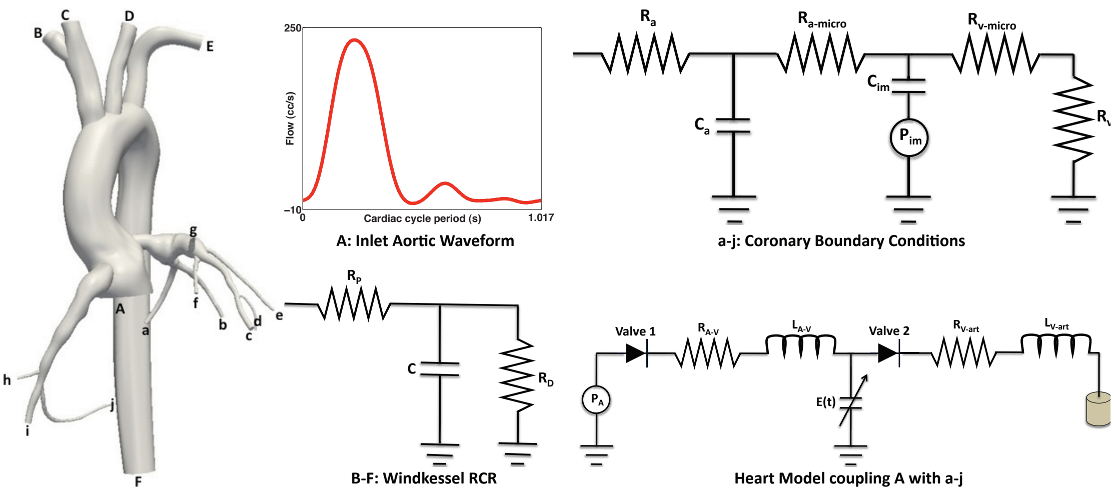

Figure 2.1: Boundary conditions imposed at the inlet (A) and outlet (F) of the aorta, the outlets of the aortic branches (B-E), and the outlets of the left and right coronary arteries (a-j), which are coupled to the lumped parameter heart model shown. The waveform shown is imposed on the aortic inlet.

A circuit analogy lumped parameter network (LPN) is constructed to model coronary flow and pressure (Figure 2.1) following previous work.[34] The model is comprised of resistors that model the effect of viscosity and downstream pressure, capacitors that model the vessel compliance, and a time-varying pressure to model the contracting ventricle. This model is governed by a set of ordinary differential equations with a known analytic solution, as described in Appendix I. This equation is implicitly coupled to the coronary outlet boundaries in the finite element solver.

The LPN coronary model has seven parameters that must be tuned to match clinical and literature data. These are the arterial resistance (R_a), microcirculation compliance (C_a), microcirculation resistance ($R_{a\text{-micro}}$), myocardial compliance (C_{im}), venous microcirculation resistance ($R_{v\text{-micro}}$), venous resistance (R_v) and intra-myocardial pressure ($P_{im}(t)$). The intramyocardial pressure is determined from the ventricular pressures obtained from a lumped parameter heart model, as described in the next section.

Values of the LPN parameters are first determined for the normal coronary model, and the same values are then applied to the KD model. This choice is justified by the observation that the distal coronary geometry is unaffected in the KD case, and the diameter compares well with normal values. Our methodology to choose parameter values is detailed in the following paragraphs.

The total coronary flow was assumed to be 4% of the cardiac output of the patient[34, 61] and the flow percentages to the right and left coronaries were chosen to be 40% and 60% of the total coronary flow,[62] respectively. The flow split to individual coronary outlet branches in the LCA and RCA was weighted according to the outlet areas.

The total resistance ($R_a + R_{a\text{-micro}} + R_{v\text{-micro}} + R_v$) at each coronary outlet was initially estimated by the ratio of the mean pressure to the mean flow through that vessel, where the mean blood pressure is determined by (SBP + 2*DBP)/3. SBP and DBP are the systolic and the diastolic blood pressure, respectively, as measured in the clinic.

The relative values of resistances (R_a, $R_{a\text{-micro}}$, $R_{v\text{-micro}}$ and R_v) and capacitances (C_a and C_{im}) were fixed using literature data.[34] The total resistance and capacitance values for the LCA and RCA were then tuned over multiple flow simulations such that the total coronary flow matched the target values, and the peak systolic to diastolic flow ratio matched typical values for normal patients.[63]

The detailed derivation of the ODE for the LPN circuit is derived below with $P_a(t)$ and $P_c(t)$ representing the nodal pressures and $Q_a(t)$ and $Q_m(t)$ representing the branch currents as shown in Figure 2.2. Also it was assumed in the derivation that $R_v = R_v + R_{v\text{-micro}}$. The governing ODE's for the LPN is as follows.

$$P - P_a = R_a Q \tag{1}$$

$$\frac{dP_a}{dt} = \frac{Q_a}{C_a} \tag{2}$$

$$P_a - P_c = (Q - Q_a) R_{am} \tag{3}$$

$$\frac{dP_c}{dt} - \frac{dP_{im}}{dt} = \frac{Q_m}{C_{im}} \tag{4}$$

$$P_c = R_v (Q - Q_a - Q_m) \tag{5}$$

Using equations (2), (4) and (5) we obtain,

$$\begin{aligned} P_c &= R_v Q - R_v C_a \frac{dP_a}{dt} - R_v C_{im} \frac{dP_c}{dt} + R_v C_{im} \frac{P_{im}}{dt} \\ \Rightarrow R_v C \frac{dP_a}{dt} &= R_v Q - P_c - R_v C_{im} \frac{dP_c}{dt} + R_v C_{im} \frac{dP_{im}}{dt} \end{aligned} \tag{6}$$

From equations (2) and (3) we obtain,

$$P_c = R_{am} C_a \frac{dP_a}{dt} + P_a - R_{am} Q \tag{7}$$

$$\Rightarrow \frac{dP_c}{dt} = R_{am} C_a \frac{d^2 P_a}{dt^2} + \frac{dP_a}{dt} - R_{am} \frac{dQ}{dt} \tag{8}$$

Finally from equations (7), (8) and (6) we arrive at the following ODE

$$R_v R_{am} C_{im} C_a \frac{d^2 P_a}{dt^2} + (R_v C_a + R_{am} C + R_v C_{im}) \frac{dP_a}{dt} + P_a = (R_v + R_{am}) Q + R_v R_{am} C_{im} \frac{dQ}{dt} + R_v C_{im} \frac{dP_{im}}{dt} \quad (9)$$

From equation (9), using $P_a = P - R_a Q$ we arrive at the final equation in Appendix I.

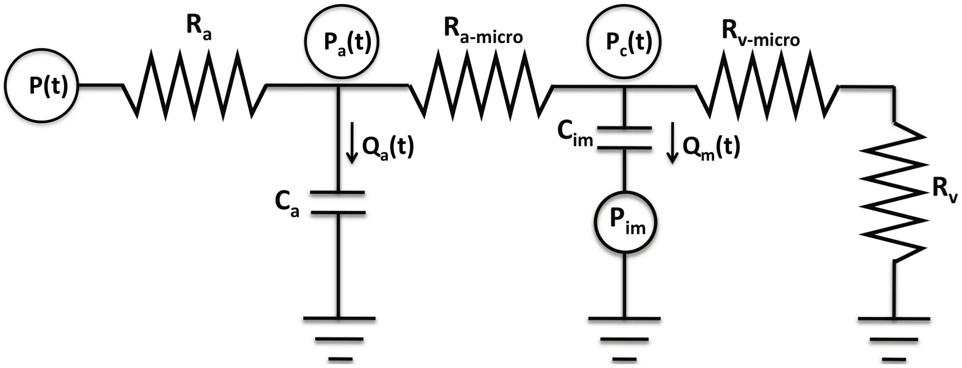

Figure 2.2: Lumped parameter network for coronary boundary condition

2.2.7 Lumped parameter heart model

The LPN coronary models were connected to a lumped parameter heart model[32] on the right and left (Figure 2.1) via the intramyocardial pressure. In the heart model, the inductances model inertial effects and the diodes model the valves. The left heart model parameters include the left atrial pressure (P_{LA}), mitral valve, atrio-ventricular valvular resistance ($R_{A\text{-}V}$), atrio-ventricular inductance ($L_{A\text{-}V}$), aortic valve, ventriculo-arterial valvular resitance ($R_{V\text{-}art}$), ventriculo-arterial inductance ($L_{A\text{-}art}$) and left ventricular pressure. The left ventricular pressure is modeled with a normalized time varying elastance function.[31] From the normalized elastance function, a patient specific elastance function is computed from the patient's blood pressure, heart rate and cardiac output. Parameters in the right heart model are similar.

The intra-myocardial pressure is obtained from the ventricular pressures using appropriate weights, as discussed in Appendix I. The parameter values for the heart model are chosen to match the pulse pressure and the cardiac output of the patient. The patient had a blood pressure of 105/52 and a BSA of $1.16m^2$ at time of scan. His stroke volume, cardiac output and

BSA were 66.8 mL/sec, 4.1L/min and 1.33m^2, respectively one year after the scan, and were scaled to the time of scan according to the BSA,[64] to be 58mL and 3.4L/min, respectively. The corresponding cardiac cycle period and heart rate for the patient were 1.02 sec and 59 beats per minute. These parameters along with the applied aortic flow waveform are used to determine patient specific ventricular pressures by solving the lumped parameter heart model circuit separately. The differential equations governing the lumped parameter heart model are given in Appendix I.

2.2.8 RCR boundary conditions

RCR boundary conditions were applied at all other outlets to model the remaining downstream vasculature. The target mean flow through each outlet was fixed based on the branch area.[65] The total resistance of all the outlets was calculated as the ratio of mean pressure to mean flow. The relative values of proximal resistance to total resistance were fixed at 15.6%.[16] The total capacitance values were tuned to match the measured blood pressure of the patient.

2.2.9 Exposure Time Computations

A high density of massless particles was injected virtually into in the right and the left coronary artery vasculature and the particle paths were tracked in the domain following the velocity field. As a measure of particle residence time, the average time spent by the particles in each mesh element was calculated to provide a means to localize and quantify regions of recirculation. Using this procedure, the time spent by all the particles in each element was normalized by the element volume and the total number of particles released, to obtain the cumulative exposure time (CET).[52] We hypothesize that CET is a clinically significant parameter in quantifying recirculation or stagnation in the flow field. Both vigorously recirculating particles and slow moving particles contribute to CET, as both increase the likelihood of thrombosis in regions of separated flow. Details of the CET formulation are described in Appendix II.

2.3 Results

Figure 2.3 shows the CT data with giant aneurysms in the right and left coronary arteries of the patient and the reconstructed models of both the diseased and the virtually created normal coronary artery models. Simulations were performed both with the virtual control normal model and the diseased KD model using identical boundary conditions.

2.3.1 Flow and pressure

Figure 2.4 compares flow and pressure at the outlets of the normal and the diseased coronary arteries. Results confirmed that flow at outlets C and D in the LCA and RCA peaks during diastole, whereas flow at all other outlets peaks during systole. Thus the boundary conditions have captured the expected physiologic behavior of coronary flow. The high intramyocardial pressure during systole impeded the systolic flow through the coronary arteries while the low intramyocardial pressure during diastole maintained a high diastolic flow through them. The flow and pressure waveforms (Figure 2.4) and mean values (Table 2.1) in the LCA and RCA for the normal and KD cases were nearly identical. The minimum and maximum aortic pressures obtained from the simulation were 106 mmHg and 49 mmHg, which compared well with the patient blood pressure of 105/52 mmHg.

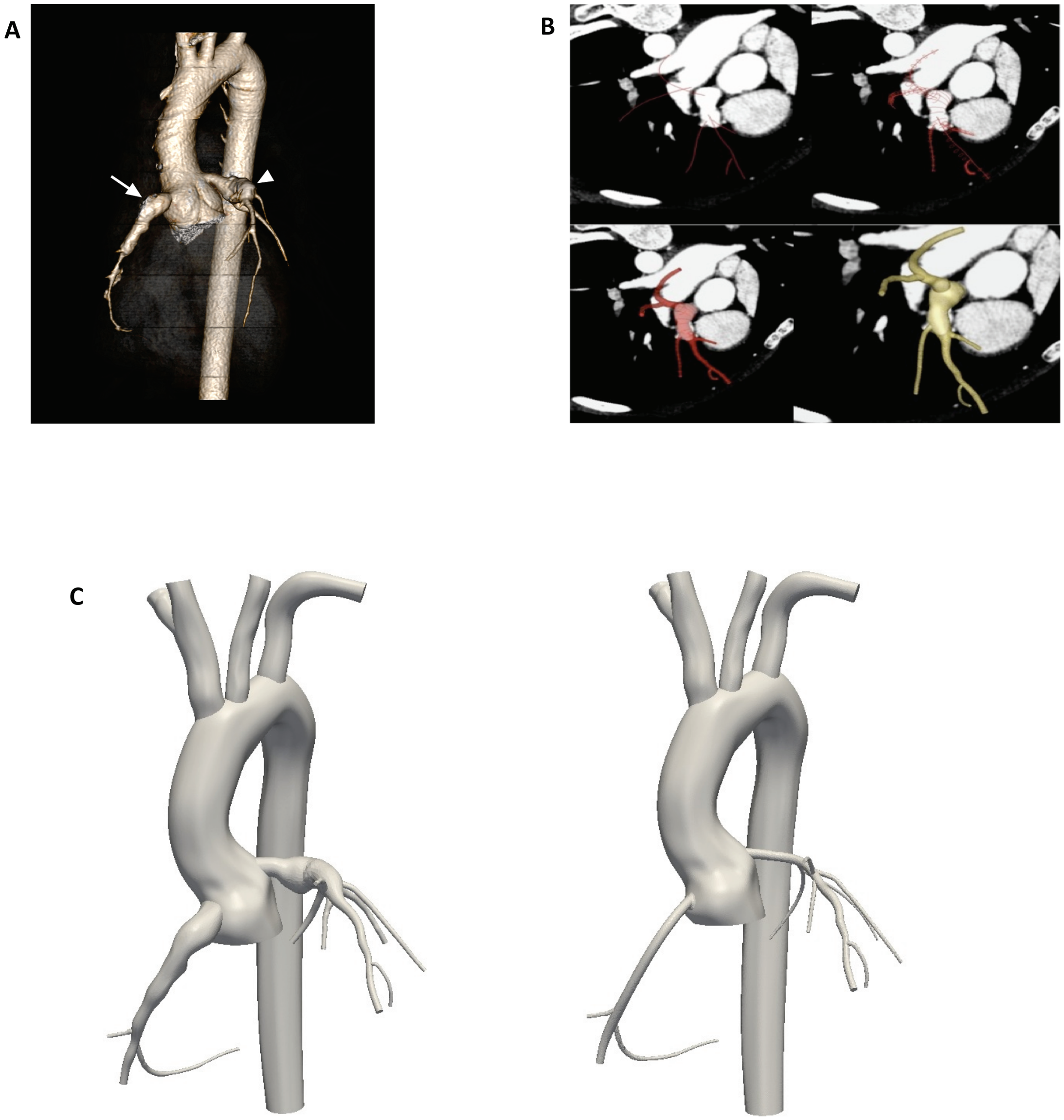

Figure 2.3: Image data and model construction for a 10-year old KD patient: A) Three-dimensional reconstruction of CT data showing giant aneurysms of the proximal right (arrow) and left main and proximal left anterior descending (arrowhead) coronary arteries B) Four steps of model construction are a) Creating paths, b) Creating segmentations, c) Lofting geometry and d) Meshing C) KD patient specific model (left) and virtual control constructed from the same data (right).

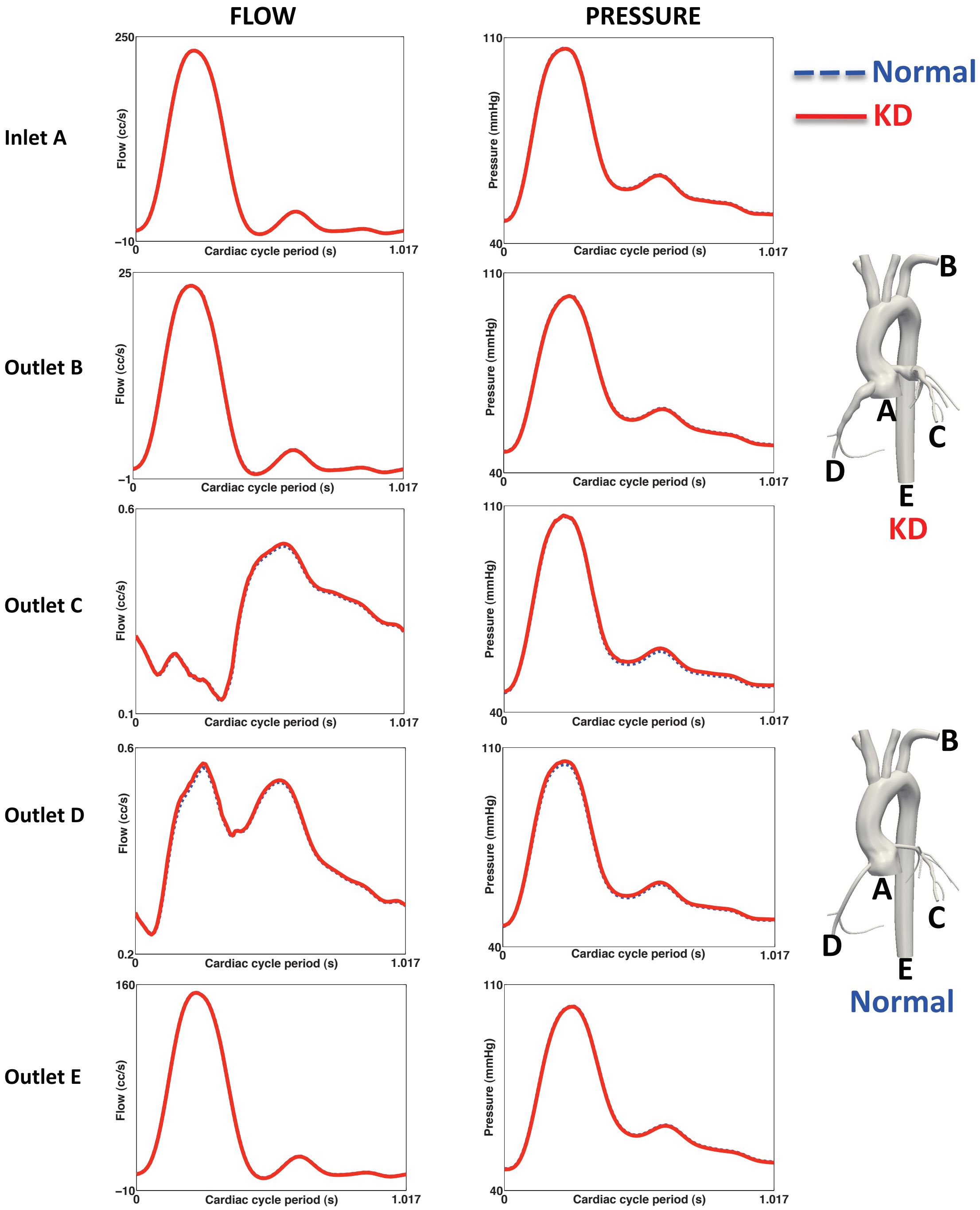

Figure 2.4: Flow and pressure waveform comparison for the normal and KD model over one cardiac cycle at different outlets. The aneurysmal geometry results in no significant changes to aortic or coronary flow and pressure compared to the normal case.

2.3.2 Velocity

The velocity in the left coronary, left circumflex and the left anterior descending artery was maximum during diastole even when the velocity in all the other branches was much lower (Figure 2.5). Velocity in the aneurysms of both the left and right coronaries remained persistently low throughout the cardiac cycle when compared to that of the normal coronary simulation. The flow pattern also exhibited substantial recirculation in the aneurysms.

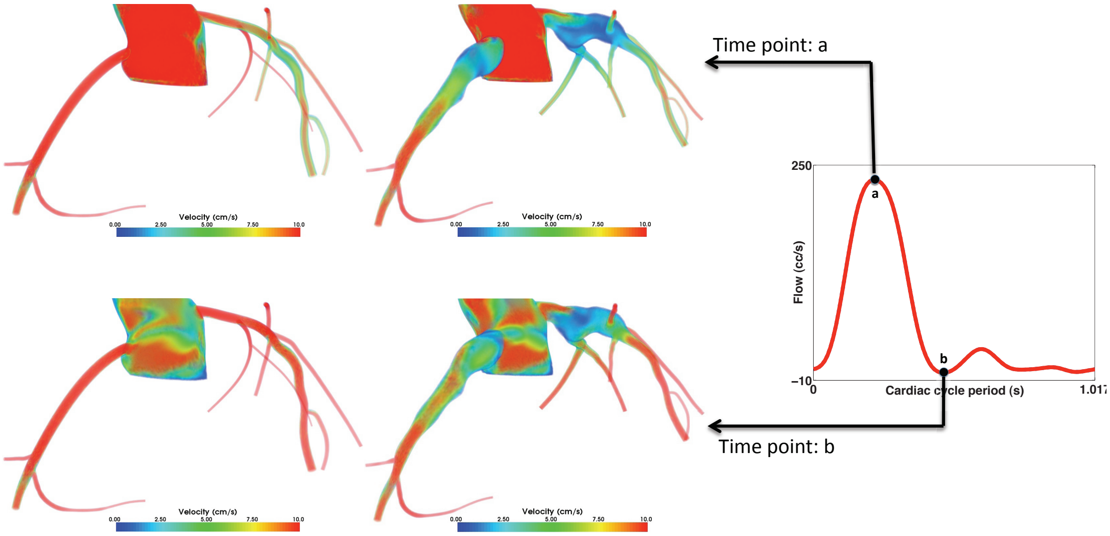

Figure 2.5: Comparison of volume rendered velocity at different points in the cardiac cycle for the KD and normal models. Flow stagnation is evident in the KD model throughout the cardiac cycle.

Table 2.1: Flow data in LCA and RCA for the normal and KD simulations

	Mean LCA flow throughout the cardiac cycle (% of cardiac output)	Mean RCA flow throughout the cardiac cycle (% of cardiac output)	Total coronary flow throughout the cardiac cycle (% of cardiac output)	Mean LCA flow throughout the cardiac cycle (% of total coronary flow)	Mean RCA flow throughout the cardiac cycle (% of total coronary flow)
Normal	2.52	1.70	4.22	59.71	40.29
KD	2.76	1.72	4.48	61.60	38.40

Table 2.2: WSS and OSI values in normal and KD models

	WSS (dynes/ sq cm)			OSI		
	Mean	Max	Min	Mean	Max	Min
LAD: KD	3.81	4.52	0.05	0.090	0.430	0.004
LAD: Normal	27.15	40.10	11.36	0.002	0.080	0.000
RCA: KD	2.95	5.43	0.05	0.083	0.420	0.007
RCA: Normal	17.10	39.64	6.70	0.001	0.070	0.000

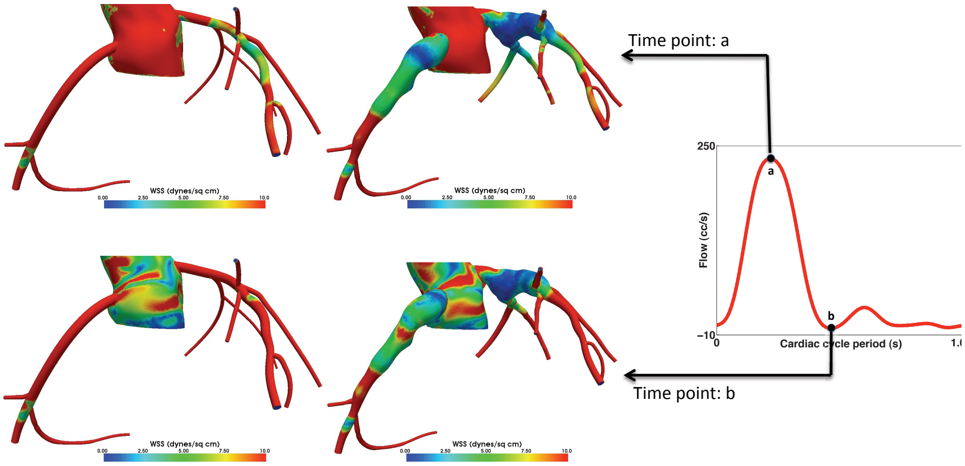

Figure 2.6: Comparison of WSS at different points in the cardiac cycle for the KD and normal models.

2.3.3 Wall Shear Stress

Wall shear stress and oscillatory shear index[66] (OSI) contours are shown in Figure 2.6 and Figure 2.7 respectively. There was a significant reduction in WSS in the aneurysmal parts due to flow recirculation and stagnation (Figure 2.6). Values of OSI range from 0 in undisturbed flow with unidirectional shear stress vectors to 0.5 with disturbed flow and oscillatory shear stress vectors. Flow recirculation led to high values of OSI in the aneurysmal region compared to the normal coronary arteries where the OSI was almost zero throughout the length of the cardiac cycle (Figure 2.7). Thus the aneurysmal regions are accompanied by a highly oscillatory and low shear stress compared to the normal model. The time-varying WSS for the normal and KD cases are shown in Figure 2.8 for several locations along the length of the LAD and RCA. WSS values varied significantly from the proximal aneurysmal to the distal normal locations throughout the cardiac cycle. By comparison, in the aneurysmal parts of the KD model, the WSS values were nearly an order of magnitude lower than in the normal model. Distal to the aneurysm, there was little difference between the KD and normal WSS curves, confirming that the effect on WSS in the KD case is locally confined. Values in the simulated normal coronary artery models were in the range of previously reported normal values.[67-69] A comparison of WSS at different locations in the KD model showed a significant jump from the aneurysmal to the distal region. (Figure 2.9)

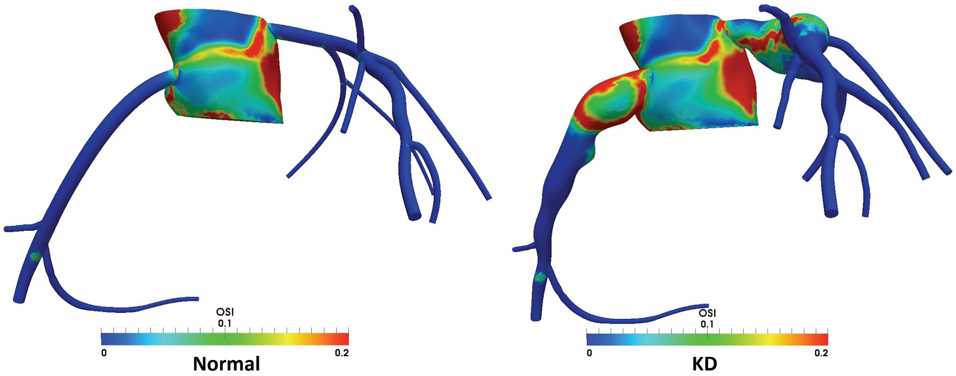

Figure 2.7: Comparison of OSI between the KD and normal models.

The mean, maximum and minimum values of WSS and OSI in the aneurysmal regions in the LAD and RCA of the KD model are presented in Table 2.2. The corresponding values in the similar regions of the normal model are also shown. The WSS and OSI values in the normal coronary arteries are about an order of magnitude higher than in the KD model. The OSI in the normal model is nearly zero indicating nearly unidirectional floFigure 2.10 compares the spatial and temporal mean WSS and the lumen radius along the length of the RCA and LAD between the KD and the normal model. Distal to the aneurysmal region in the KD model, there is a sudden narrowing of lumen diameter back to normal value. WSS gradients, which are a measure of the two-dimensional stretch of endothelial cells lining the arterial wall are also computed. Figure 2.11 quantifies the spatial and temporal mean WSS, WSS gradients and OSI vs. radius along the length of the RCA and LAD in the KD model. Due to the narrowing of the lumen radius in the regions distal to the aneurysms, there was a sharp increase in WSS gradient and a drop in OSI. The average WSS gradient increased from 5.50 dynes/cm^3 and 4.85 dynes/cm^3 in the aneurysmal regions of the LAD and RCA, respectively, to 17.50 dynes/cm^3 and 25 dynes/cm^3 at the outlets of the aneurysms. The WSS gradient in the normal coronary artery model over the same region did not fluctuate much, with values of 18.5 dynes/cm^3 in the LAD and 24.40 dynes/cm^3 in the RCA.

2.3.4 Particle Tracking

Particle tracking simulations performed in the LCA and RCA of the KD model revealed that about 32% of the particles remained in the LCA and 28% remained in the RCA after the first cardiac cycle. Nearly all the particles were flushed out of the domain after 5 cardiac cycles. By comparison, the corresponding simulations performed on the model with normal coronary arteries revealed that only 6% of the particles remained in the LCA and 11% of the particles remained in the RCA after the first cardiac cycle and all particles in both the LCA and RCA were completely flushed out within just 1.3 cardiac cycles.

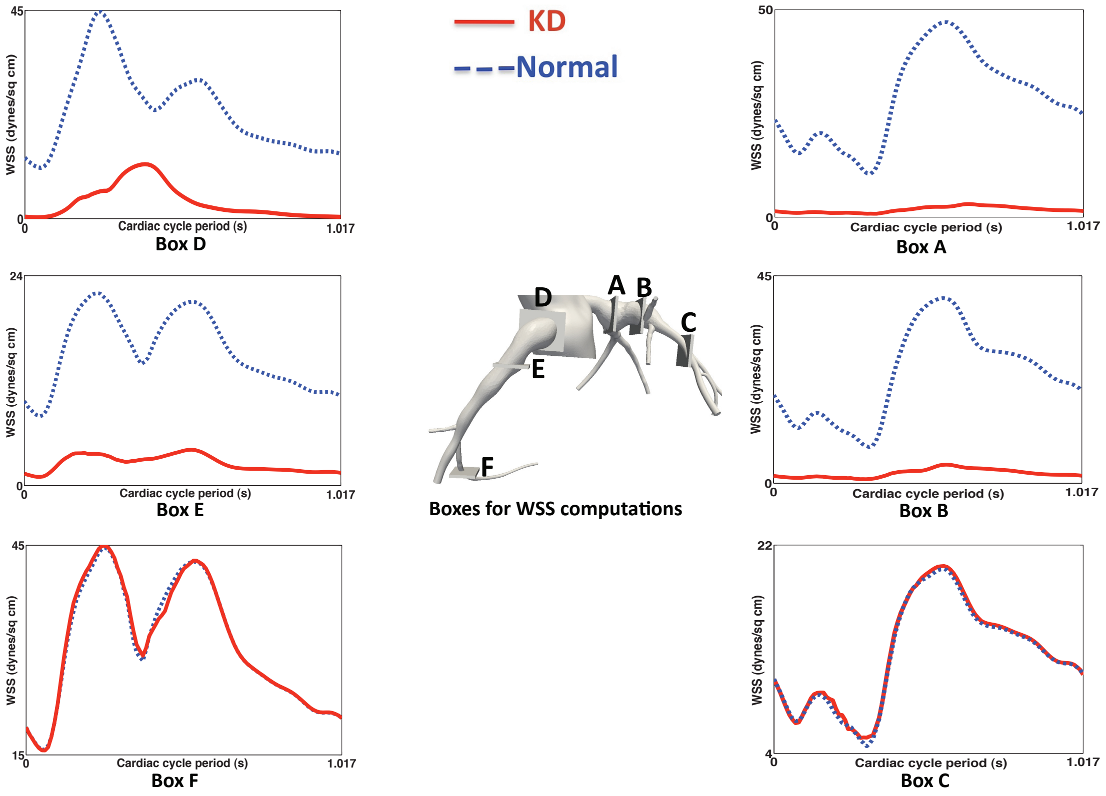

Figure 2.8: Comparison of time varying and spatially averaged WSS for the KD and normal models at different locations in the RCA (left column, Boxes D-F) and LAD (right column, Boxes A-C)

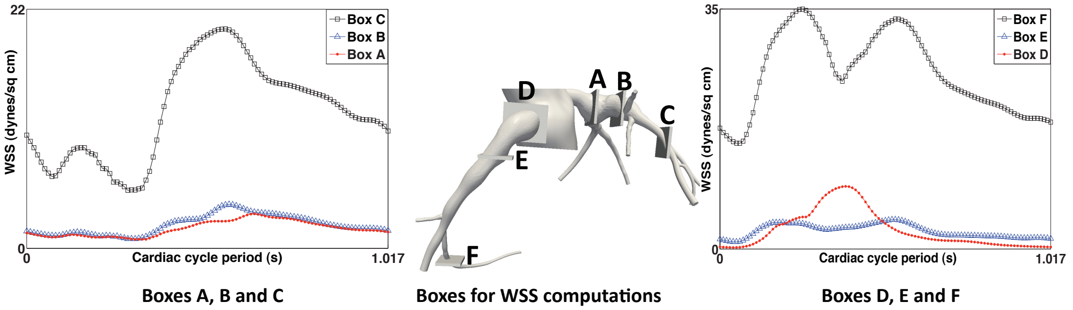

Figure 2.9: Comparison of the time varying and spatially averaged WSS magnitude within the KD model at different locations in the LAD (right, Boxes A-C) and RCA (left, Boxes D-F).

The cumulative exposure time (CET) plots at different locations throughout LAD and RCA are shown in Figure 2.12. In the aneurysmal region, the CET was high (indicated by red) and progressively decreased with sudden decrease of radius and increasing velocity. We confirmed an inverse relationship between magnitudes of CET and velocity. Figure 2.13 illustrates the variation of average CET with the lumen radius indicating that the aneurysmal region had a higher CET compared to the distal region. Increasing CET values along the length of the coronaries also correlated with decreasing WSS values, with correlation coefficients of -0.64 (RCA) and -0.50 (LAD) while decreasing WSS values correlated with larger lumen radius with a correlation coefficient of -0.86 (RCA) and -0.77 (LAD) (Figure 2.12). The higher values of CET and lower values of WSS indicated substantial flow recirculation in the aneurysmal regions.

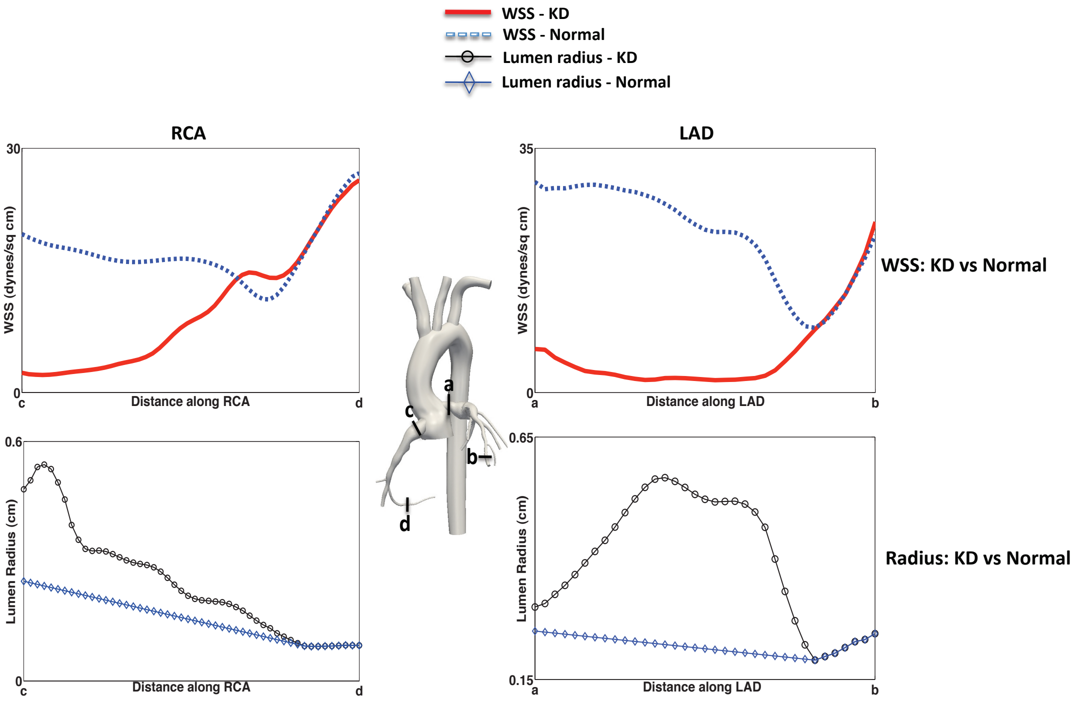

Figure 2.10: Comparison of mean WSS (top row) and Lumen Radius (bottom row) for the KD and normal models along the LAD (right) and RCA (left). In all the plots, variation of parameters are obtained from points a to b in the LAD and c to d in the RCA, where distance is measured along the vessel centerline from the ostium.

Distal to the aneurysm, as the WSS suddenly increased, the CET also decreased, as shown in the correlation plots.

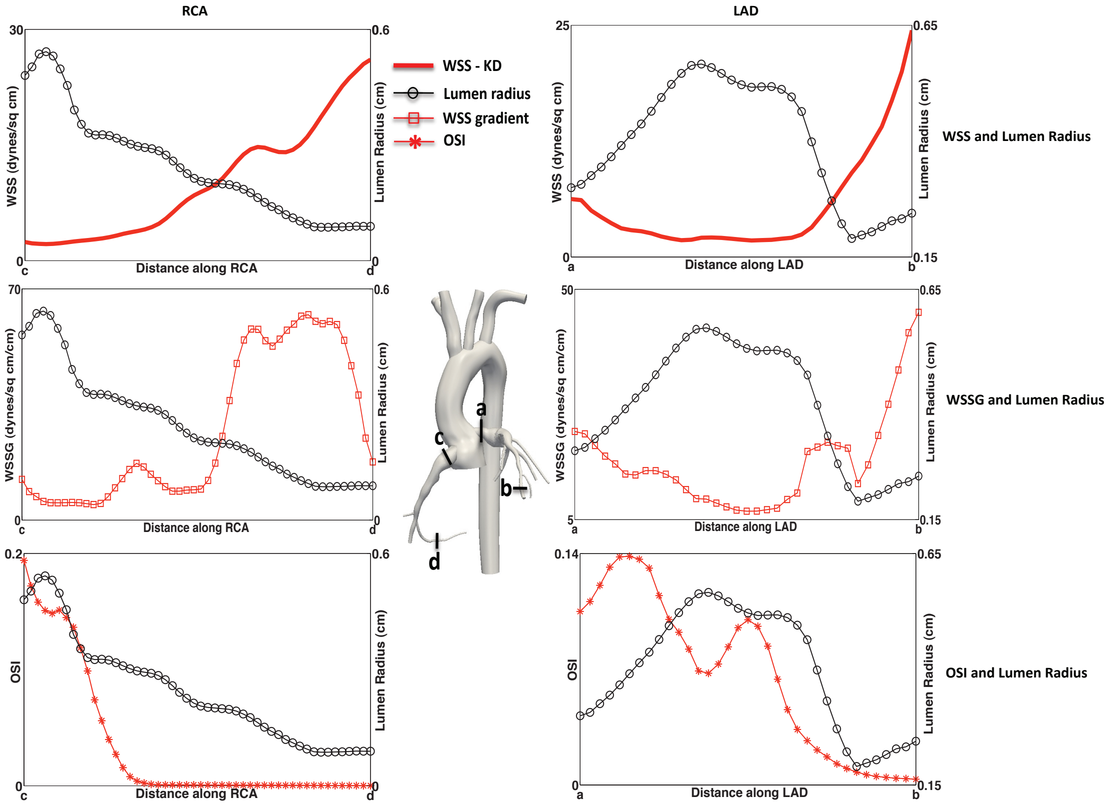

Figure 2.11: Variation of WSS and lumen radius for the KD model in the LAD (top, right) and RCA (top, left), variation of WSSG and lumen radius for the KD model in the LAD (middle, right) and RCA (middle, left) and variation of OSI and lumen radius for the KD model in the LAD (bottom right) and RCA (bottom left). In all the plots, variation of parameters are obtained from points a to b in the LAD and c to d in the RCA, where distance is measured along the vessel centerline from the ostium.

2.4 Discussion

We report the first patient-specific, finite element simulations using custom boundary conditions incorporating clinical data to characterize hemodynamics in aneurysms caused by KD.

Simulations revealed highly altered hemodynamic conditions and permitted direct comparison with a virtual control case based on the same patient.

Simulation methods provide a powerful means to obtain quantitative measures of potentially relevant clinical parameters that cannot be readily obtained by conventional imaging modalities. We have demonstrated that modeling with LPN boundary conditions produces realistic physiologic flow conditions in the coronary arteries, and that these simulations can provide detailed quantitative data for an individual KD patient. As expected, the presence of aneurysms in our model did not affect the global blood flow and pressure waveforms, since coronary artery resistance is dominated by the distal coronary circulation. However, local parameters related to thrombus formation were strongly affected. Quantitative comparisons of WSS, WSS gradients, OSI, and particle residence times in aneurysms were made between the KD and normal models under physiologic flow conditions. Results showed that WSS is decreased, while WSS gradients, OSI, and residence times are increased in the aneurysmal regions, which is expected due to the sudden increase of lumen radius. These are consistent with increased risk of thrombus formation and inflammation. Although, these results are qualitatively intuitive, the current framework provides a means of quantifying these hemodynamic parameters accurately in a patient-specific setting.

WSS levels were an order of magnitude lower in the aneurysmal region of the KD model compared to the normal model, which were in the range of values previously reported.[67-69] Experiments using rabbit endothelium demonstrated that reduced levels of WSS varying from 0.77 to 2.79 dynes/sq cm were associated with thrombus formation.[70] Further, results from experiments in parallel plate flow chambers revealed that low shear stress values of 4 dynes/ sq cm induced extensive platelet aggregation.[71] The mean WSS values for our aneurysm model (2.95-3.81 dynes/sq cm) may well be in a range associated with thrombotic risk. *In vitro* experimentation to correlate WSS levels with likelihood of thrombosis should be a subject of future investigation.

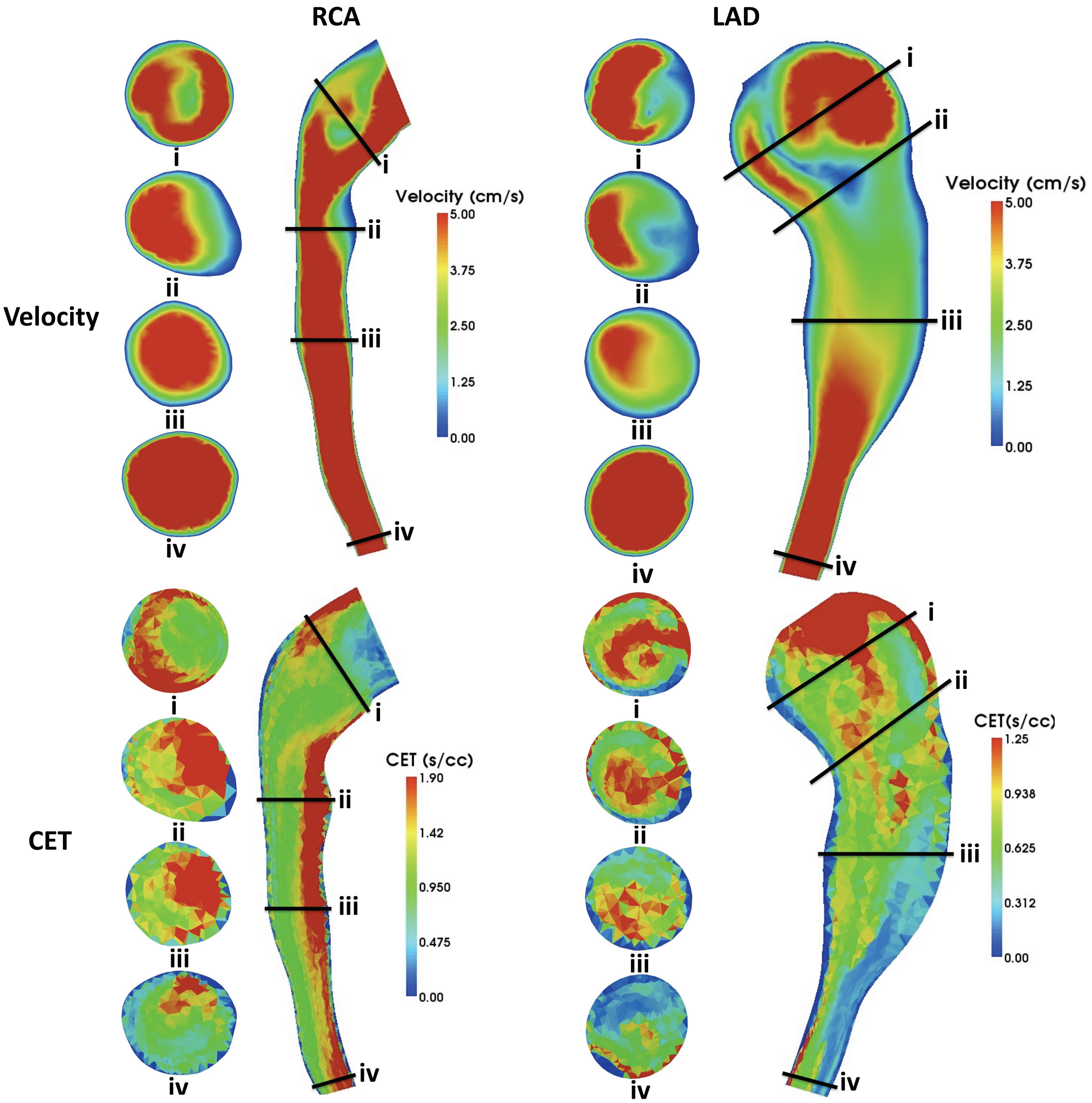

Figure 2.12: Velocity (top row) and CET (lower row) at different slices in the RCA (left) and LAD (right). Areas of high CET (red) correlate with areas of lower velocity (blue).

Compared to the normal model, OSI was an order of magnitude higher in the aneurysmal region of the KD model, indicating increased flow recirculation. *In vivo* studies using porcine aorta demonstrated that disturbed flow (presumably with elevated OSI) leads to a proinflammatory transcription profile in endothelial cells.[72] Additional *in vitro* studies using bovine endothelial cells revealed that slowly oscillating (1 Hz) shear stress with an amplitude of 3 dynes/sq cm (equal to the upper limit of OSI of 0.5) induced expression of monocyte chemoattractant protein-1 and increased binding of monocytes to the endothelium.[73] Average OSI values (0.08-0.09) in the aneurysmal regions in our simulations were elevated compared to the values in the normal model, which were uniformly zero in the corresponding region. These studies suggest that the combination of these slightly elevated OSI values in the KD model together with low shear values of may create conditions sufficient to elicit an inflammatory response and thrombosis.

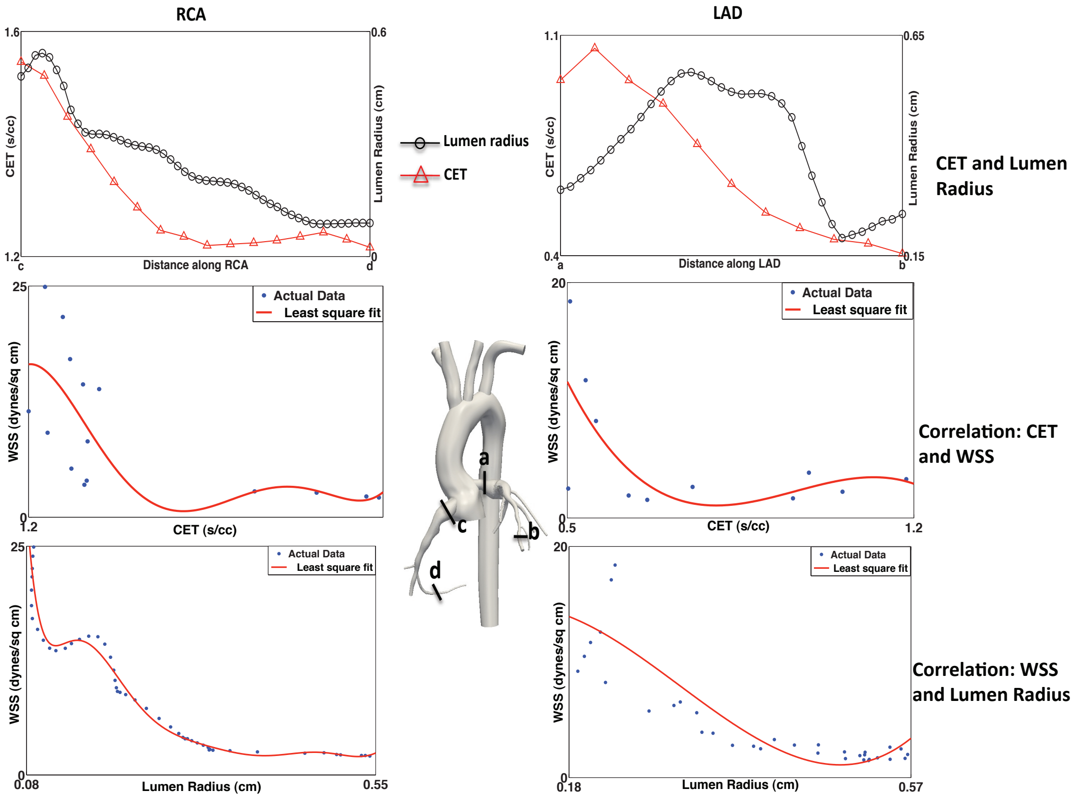

Figure 2.13 Variation of CET and lumen radius for the KD model in the LAD (top right) and RCA (top left), correlation of CET and mean WSS for the KD model in the LAD (middle left) and RCA (middle right) and correlation of lumen radius and mean WSS for the KD model in the LAD (bottom left) and RCA (bottom right). In all the plots, variation of parameters are obtained from points a to b in the LAD and c to d in the RCA, where distances is measured along the vessel centerline from the ostium.

Results demonstrated that WSS gradients are elevated at the outlet of the aneurysm. Previous work examining WSS gradients has shown that high gradients result in the upregulation of inflammatory markers[74] in endothelial cells, as well platelet aggregation leading to thrombosis.[75] *In vitro* experiments demonstrated that localized thrombosis is accompanied by an increase in WSS from 9.6 dynes/sq cm to over 20.4 dynes/sq cm.[75] This compares favorably to the increase in WSS values from the body of the aneurysm to the outlet in the KD model (3.81

dynes/sq cm to 12.60 dynes/sq cm in LAD and 2.95 dynes/sq cm to 14.20 dynes/sq cm in RCA). The simulated levels of WSS and WSS gradient values support the clinical observation that the aneurysms are prone to thrombosis and inflammation.[9]

Particle tracking simulations revealed that 30% of particles re-circulated in the coronary aneurysm for at least one full cardiac cycle, with some particles remaining in the domain for as long as 5 cardiac cycles. This is significantly longer than in the normal coronary artery model, in which all particles were washed from the domain within 1.3 cardiac cycles. CET values, a measure of re-circulation time, were approximately 1.3–2.0 times higher in the aneurysmal region. High values of CET also correlated with regions of low WSS, again suggesting a high risk for thrombosis in these regions. *In vitro* measurements of particle recirculation and residence times are difficult to perform due to several factors including inaccurate quantification of the number of particles in the model, rapid washing out of particles from the domain, difficulties in accurate measurement of dye recirculation times, and challenges in uniformly seeding the particles without altering the flow field.[76] However, in the present computational method, these problems can be overcome and an accurate representation of the *in vivo* behavior can be obtained.

The primary focus of this work was to investigate hemodynamic parameters such as WSS, WSSG, OSI and CET that could inform physicians about risk of thrombus formation and vessel wall inflammation in specific patients. Data from autopsy studies of KD patients demonstrate that thrombosis of aneurysms associated with inflammation in the arterial wall is common.[77] In patients with giant aneurysms such as our subject, there is consensus that systemic anticoagulation reduces morbidity and mortality.[9] However, in patients with smaller aneurysms (<8mm), management decisions are less straightforward. The AHA guidelines for the management of KD patients with coronary artery aneurysms were only based on Level of Evidence C (expert opinion, case studies, or standard of care).[8] In addition, there are no quantitative data indicating how the actual shape of the aneurysm affects the clinical risk of thrombus formation. The same techniques presented here could also be applied to patients with smaller aneurysms with a range of shapes. Using this framework, simulated perturbations can be made in the coronary anatomy to systematically study the effects of specific geometric changes on the hemodynamics. Hence these techniques could provide a framework for evaluating how the size and shape of coronary aneurysms affect the hemodynamics, which would be useful in risk stratifying patients and choosing optimal treatment strategies. Furthermore, these same techniques could also be applied to evaluate coronary artery hemodynamics based upon the anatomic data in patients with other coronary artery pathologies.

Limitations of this work include the assumption of a Newtonian fluid, which could be addressed in future work by implementation of non-Newtonian models[78] or multiscale modeling of clot formation to predict onset of thrombus.[79] An additional limitation is the assumption of rigid arterial walls in the simulation, which does not account for the significant motion and curvature changes of the coronary arteries during the cardiac cycle. In addition, the effect of calcium accumulation in the arterial wall that is a frequent sequelae of the inflammation was not considered in our model.[80] This could be addressed in future work through the use of fluid structure interaction methods, which could be extended to incorporate variable properties of the vessel wall including calcification.[81] There are limited data on flow split percentages to the left and right coronary arteries and the relationship of the intra-myocardial pressures to the left and right ventricular pressures, and these are possible minor sources of error. For validation of these models, it may be possible to use MRI with phase-contrast imaging to measure coronary artery flow.

In summary, we have utilized patient-specific data to create a simulation framework that allows assessment of velocity, WSS, WSS gradients, OSI and CET. Future application of this technique will include modeling the effects of arterial wall calcification and aneurysm shape and location on flow dynamics, assessing patient-specific risk for thrombosis, and planning interventions including stent placement and bypass grafting. This work presents a step towards developing such a framework.

Chapter 3

3. Patient specific modeling of multiple Kawasaki Disease patients with coronary aneurysms and comparison with clinical outcomes

3.1 Introduction

In chapter 2 we observed that simulations can provide critical hemodynamic information linked to thrombotic risk, including wall shear stress (WSS), particle recirculation time, and oscillatory shear index (OSI), which are difficult or impossible to obtain from standard imaging modalities. Simulations have been used extensively in other clinical applications such as congenital heart disease[12, 39, 82, 83], abdominal aortic aneurysms[16], cerebral aneurysms[84-86], virtual surgery optimization[45] and coronary artery bypass grafts[15, 87] and there has been growing recent interest in the use of simulations as a diagnostic tool in the coronary arteries[88]. The study in chapter 2 also demonstrated that custom downstream coronary boundary conditions, along with a lumped parameter heart model[31, 34] effectively captured the physiologic coronary circulation. Further, it was shown that the presence of aneurysms did not produce significant changes in the global flow and pressure waveforms. However, order of magnitude changes in local hemodynamic quantities, including wall shear stress, wall shear stress gradients, oscillatory shear index, and particle residence times were observed.

Coronary aneurysm shape varies greatly among patients, and can be saccular, fusiform, or have a string-of-pearls appearance. While aneurysms can be imaged to obtain detailed anatomical information, there are currently no available clinical tools to predict the risk of coronary artery thrombosis or myocardial infarction. Imaging flow in the coronary arteries non-invasively using phase contrast magnetic resonance imaging (MRI) is possible, but is technically challenging because the coronary arteries are small and mobile, with maximum displacements in the right and the left coronary arteries of about 16mm and 10mm respectively[46, 47]. CT angiography can now be performed with relatively low radiation doses to non-invasively image coronary artery anatomy[48], but provides no direct hemodynamic information. Limited flow information can be obtained invasively through cardiac catheterization, but this is typically limited to global flow and pressure waveforms. It is therefore desirable to obtain the missing hemodynamic information through the use of patient-specific simulations.

In this chapter, we applied patient specific modeling to a cohort of five KD patients with aneurysms and one KD patient with normal coronary arteries. This work incorporates recent advances in simulation technology, including sophisticated lumped parameter boundary conditions[89], increasing anatomic realism[51] and particle tracking[10]. An iterative tuning algorithm was developed to match patient specific clinical parameters for the boundary conditions. We calculated key hemodynamic quantities that are postulated to be surrogates for thrombotic risk and compared these hemodynamic measurements with patient outcomes, including incidence of thrombosis and myocardial infarction. We also compared conditions among aneurysms of different shapes from more saccular to more fusiform. This comparison uncovered surprising and non-intuitive relationships between aneurysm diameter, the currently accepted standard for treatment decisions, and hemodynamic quantities linked to thrombus formation. Our results show that large anatomical differences, even in aneurysms with the same maximum diameter, can lead to drastically different hemodynamic conditions, and likely different thrombotic risk. These data suggest that patient-specific computational analysis based on CT imaging could be used to construct a clinical index to risk-stratify patients.

3.2 Methods

3.2.1 Subject Data

Six KD patients were modeled in this pilot study, of whom five had coronary aneurysms (A-E) and one (F) did not, and served as the control. A brief clinical history was collected for all patients (Table 3.1), and clinical data used for simulations was obtained at or near the time of the performance of the CT angiogram that was used for the patient specific modeling (supplemental Table 3.1). Patient-specific geometry was obtained from clinically-indicated CT angiograms, with patient A-D and F imaged at UCSD (CT750 HD 64-slice CT scanner, GE Medical, Milwaukee, WI), and patient E imaged at Sechenov First Moscow State University (Aquilion ONE 320 slice CT scanner, Toshiba, Tokyo, Japan). This study was approved by the Institutional Review Board at UCSD and First Moscow State University, and written subject consent or assent and parental consent were obtained as appropriate for the imaging and simulation studies.

Table 3.1: Clinical Data collected for patients A-F.

Patient ID	Blood Pressure (mmHg)	Cardiac Output (L/min)	Stroke Volume (mL)	Heart Rate (bpm)	Body Surface Area (m^2)
A	105/52	3.4	58.00	59	1.16
B	108/67	4.9	83.20	59	1.79
C	140/82	5.5	91.67	60	2.10
D	96/57	5.2	112.80	46	1.97
E	90/55	4.3	41.00	105	0.76
F	123/81	3.8	90.47	42	1.70

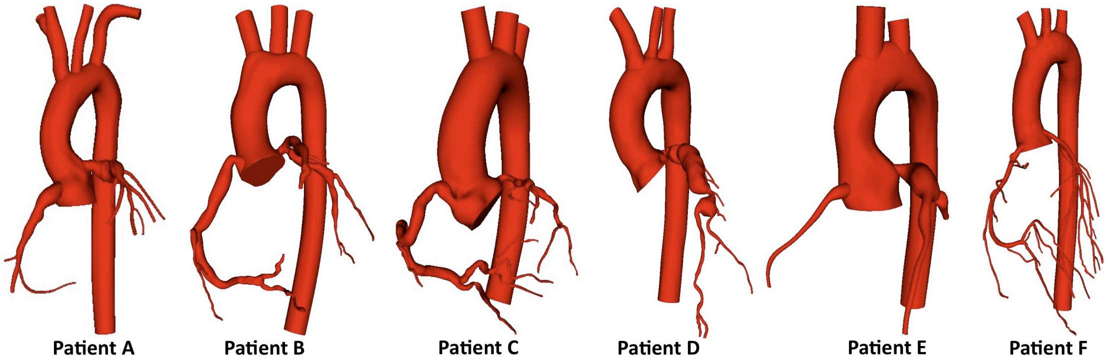

Figure 3.1: Patient specific models constructed from CT image data for KD patients with aneurysms (A-E) and one without (F).

3.2.2 3D Anatomical Models

Patient-specific 3D anatomic models were constructed from the CT image data using a customized version of the open source Simvascular software package following our previous work[51]. Three steps were used to reconstruct 3D geometric models from the CTA: (i) creation of centerline paths for vessels of interest (ii) segmentation of the vessel lumen through a combination of pixel intensity thresholding and level set methods, and (iii) lofting the segmentations to construct a final 3D model. Anatomy in the models included all left and right coronary artery branches resolved in the image data, the ascending and descending aorta, and the subclavian arteries. Figure 3.1 shows the reconstructed models for all patients. Patient D had an occluded right coronary artery and the RCA was excluded from the model as no contrast filling was observed in the CT image data. A finite element mesh was constructed for each patient specific model using the commercial software Meshsim (Symmetrix, Inc, Clifton Park, NY). We employed mesh adaptation with Hessian-based error estimators with an average mesh size of approximately 0.2mm to ensure mesh convergence[55] and resulting meshes had on average over 3 million elements.

3.2.3 Simulation Methods

Blood flow dynamics are governed by the following strong form of the Navier-Stokes equations:

$$\rho(\vec{v}_{,t} + \vec{v} \cdot \nabla \vec{v} - f) = -\nabla p + \nabla \cdot \tau \qquad \forall x \in \Omega. \quad (1)$$

$$\forall x \in \partial_g \Omega \ : v_i = g_i. \quad (2)$$

$$\forall x \in \partial_h \Omega \ : -pn + \tau_{ji} n_j = h_i. \quad (3)$$

where Ω represents the 3D domain, ρ is the density if blood, v is the blood velocity, p is the pressure, n is the normal to the vessel wall, τ is the stress on the wall, f are the body forces (neglected here), t represents time and x denotes space. The Neumann and Dirichlet boundaries are denoted by $\partial_h\Omega$ and $\partial_g\Omega$ respectively, and the values of the traction and velocity are denoted by h and g respectively.

The corresponding weak form is given by

$$\int \rho \vec{w} \cdot (\vec{v}_{,t} + \vec{v} \cdot \nabla \vec{v} - f) d\Omega = \int \vec{w} \cdot (-\nabla p + \nabla \cdot \tau) d\Omega$$

Blood flow simulations were run with a custom finite element Navier-Stokes solver. The flow solver uses the second order accurate generalized alpha method for time discretization, and spatial stabilization is achieved utilizing a SUPG method, enabling the use of linear finite elements[90]. A custom linear solver in the finite element solver combined the generalized minimum residual and conjugate gradient methods with a resistance-based preconditioner for improved efficiency. Blood is modeled as a Newtonian fluid with density 1.06g/cc and a dynamic viscosity of 0.04 dynes/cm^2, and walls are assumed to be rigid, though we use capacitance elements in each of the outlets to capture the global effect of wall compliance. Simulations were run for 6 cardiac cycles, at which time the cycle-to-cycle variations in the pressure field were less than 1%. Additional backflow stabilization terms acting only during the periods of flow reversal were used to prevent simulation divergence due to backflow following our recent work[51].

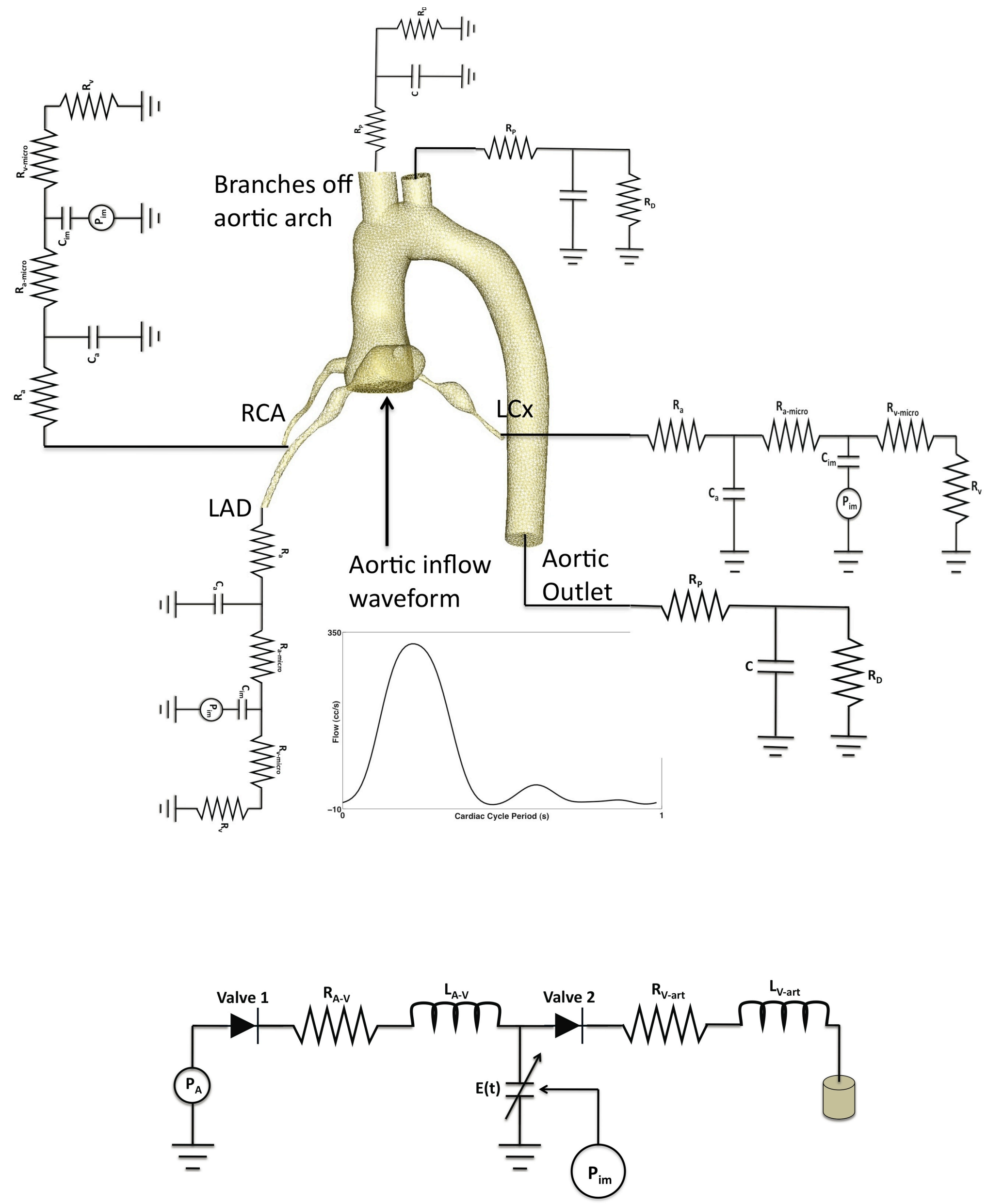

Figure 3.2: Lumped parameter boundary condition.

3.2.4 Boundary Conditions

The choice of boundary conditions is critical in hemodynamics simulations, and this is particularly true for coronary arteries since pressure and flow waveforms are out of phase due to changing resistance during cardiac contraction. In addition, measuring coronary flow directly with phase contrast MRI remains an area of active research, so that a patient specific flow waveform cannot be applied directly at the coronary inflow boundary. To properly model coronary physiology, specialized lumped parameter boundary conditions are applied at the outlets of the coronary arteries, following the work of Kim et al[32, 34] using the coupled multidomain method[25] and applied by our group in a case study of KD[51].

At the aortic inflow face, a volumetric flow waveform (i.e. Dirichlet boundary condition) was applied. For patients C and D, the aortic flow waveform was obtained from phase contrast MRI measurements and directly imposed on the aortic inflow face. For all other patients, a typical aortic waveform was scaled to match the cardiac output and heart rate of the respective patients.

At all coronary outflow faces, lumped parameter coronary boundary conditions are applied, which are coupled to a lumped parameter heart model. The lumped parameter coronary circulation model (Figure 3.2) consists of resistors and capacitors that model the viscous and compliance effects of the coronary arterial bed. The ordinary differential equation (ODE) governing this circuit and analytic solution for the ODE is derived in the previous chapter. The corresponding analytic solution for the ODE is given in Appendix I.

The equation is coupled monolithically, as a Neumann boundary condition, to the 3D domain using the coupled multidomain method, introduced by Vignon et al[25] and following the work of Kim et al.

The lumped parameter heart model (Figure 3.2) contains resistors, inductors, diodes, and time varying elastance functions modeling the viscous, inertial and contractive effects of the myocardial muscles and the valves. The heart model is used off-line to solve for the myocardial pressure, which is then imposed in the lumped parameter coronary network to drive changes in vascular resistance with cardiac contraction. The boundary condition parameter values are tuned to match the patient specific clinical data shown in Table 3.1, details of which are outlined in the following section. In all models, the total coronary bed resistance was tuned such that mean coronary flow was approximately 4% of the total cardiac output. Left and right coronary artery resistances were then tuned so that the right/left flow split was approximately 40%/60% of the total coronary flow[62]. Resistances of the individual coronary outlets were then weighted to be inversely proportional to the outlet area of each vessel. Capacitance values were chosen to match previously reported resistance to capacitance ratios for the coronary arteries[34, 51, 91]. Parameter values were iteratively tuned by running successive hemodynamic simulations until the target patient blood pressure, the assumed flow splits in the coronary arteries, a the target ratio obtained from the literature[63] between the systolic and diastolic peak in the coronary flow waveform were obtained. The coupled coronary and lumped parameter heart models captured the typical physiologic flow features of the coronary circulation, with maximum flow during diastole and minimum flow during systole, which is especially pronounced in the left coronary artery.

At all other outlets, i.e. the aorta and subclavian vessels, Windkessel RCR boundary conditions were applied[25, 60]. Resistances were estimated as the ratio of mean pressure to mean flow, using patient blood pressure as a target value. The relative resistance values at different outlets, as well as ratios of proximal to distal resistances and capacitance values were tuned to match patient specific blood pressure measurements and literature data as in the previous chapter.

3.2.5 Choice of patient specific parameters

The choice of patient specific parameters for the boundary condition is crucial in the coronary simulation on a patient-specific model. In order to match the patient specific clinical parameters, a tuning algorithm is used which will be described in this section. The tuning algorithm is a combination of 0D tuning without performing CFD simulations and 0D-3D tuning by subsequently performing CFD simulations on the entire coronary vasculature. This kind of approach reduces the time for tuning the boundary condition parameters in coronary simulations.

The left and the right ventricular pressures are first computed for generating the intramyocardial pressure (P_{im}). In order to generate the ventricular pressure, offline 0D MATLAB scripts are used to solve the heart model circuit as shown in Figure 3.2. In order to compute the left ventricular pressure, the patient's stroke volume, end systolic volume, end diastolic volume, heart rate, cardiac output and the blood pressure are used from the clinical records. The set of ODE's as shown in Appendix I are then solved using the MATLAB script by assuming a normalized elastance function given by Senzaki et al[31]. The normalized elastance function is scaled by the patient's heart rate and the ratio of patient's ventricular pressure and ventricular volume. The left atrial pressure (P_{LA}) in the heart model circuit is tuned to match the patient's maximum blood pressure. The cardiac cycle period is proportional to the inductance, L_{AV} and it is tuned to match the patient's heart rate. The rest of the circuit components including the resistances (R_{AV} and $R_{V\text{-}art}$) and the inductance ($L_{V\text{-}art}$) are tuned to match the end systolic and end diastolic volume of the patient. A typical simulated ventricular pressure and pressure-volume loops are shown in Figure A1. A code snippet for ventricular ejection along with the relevant ODE and valve open/close testing functions are provided in appendix I.

The next step after generating the ventricular pressure is to obtain the RCR parameters for the non-coronary outlets in the patient specific model. In order to obtain the correct RCR parameters, another MATLAB script is used which is given in Appendix I. Correct RCR boundary conditions are critical in achieving accurate patient blood pressure in the CFD simulations. Three parameters in the MATLAB are tuned to achieve this – *res_scale, cap_scale* and *ratio*. The overall total resistance obtained by the ratio of mean patient blood pressure and the mean patient flow rate is used as a first guess to tune the *res_scale* parameter. The other two parameters, *cap_scale* and *ratio* are subsequently tuned to change the time constant ($\tau = R_DC$) of the circuit and match the difference between the patient's maximum and minimum blood pressure to the estimated difference between the minimum and maximum pressure from simulation. The *res_scale* parameter is eventually changed to scale the simulated pressure to match the clinical blood pressure of the patient. The resistances and capacitances at individual outlets are weighted according the area of each outlet. The script also generates the *"rcrt.dat"* which is required by CFD flowsolver.

The final step in the process of generating the boundary condition parameters file is the creation of the *"cort.dat"* which is essential for running coronary flow simulations using the finite element flowsolver. As described in the previous section, the total coronary flow is targeted to be 4% of the cardiac output[34, 51] and the left and right flow split in the coronaries is assumed to be 60% and 40% respectively[51] yielding a total flow of 2.4% of the cardiac output in the left and 1.6% of the cardiac output in the right coronary arteries. Furthermore, a target systolic to diastolic peak flow ratio of 0.37 (±0.12) in left coronary and 0.97 (±0.58) in right coronary are assumed following the work of Marcus et al[63]. The intramyocardial pressure (P_{im}) used in the left and right coronary outlets is calculated from the ventricular pressures as discussed in Appendix I. The parameters in coronary boundary condition tuned based on these clinical parameters. Two separate MATLAB scripts are used to solve the 0D LPN for the coronaries – one for the left and the other for the right, each of which produces the file *"cort_lca.dat"* and *"cort_rca.dat"* which is finally merged into *"cort.dat"* used in the CFD solver. An example script is provided in Appendix I for estimating the parameters for the left coronary circuit. The important parameters used for tuning the flow through the coronary outlets are – *res_scale, cap_scale_cim* and *cap_scale_ca.* The *res_scale* is used for tuning the overall flow percentage in the left or the right coronary. After achieving the desired flow percentage, the parameters for capacitance scaling *cap_scale_cim* and *cap_scale_ca* are used to obtain the desired shape of the coronary flow waveform by tuning for the target systolic to diastolic peak flow ratio.

After generating the *"rcrt.dat"* and *"cort.dat"*, patient-specific CFD simulations are run for the 3D-0D coupling in a parallel environment. Typically, the boundary condition parameter values obtained directly from the 0D MATLAB scripts, over-predicts the actual pressure as obtained from the 3D CFD simulations due to the non-linear terms present in the Navier-Stokes equations. While, the flow in the coronaries are usually under-predicted by the 0D code and CFD simulations reveal a higher flow percentage than the desired value. Hence, the boundary conditions are further tuned using the same MATLAB scripts by increasing the resistance for the RCR and lumped parameter coronary circuits. Multiple 3D simulations are run in this manner until the desired patient-specific clinical parameters are obtained.

The mesh size for a typical patient-specific simulation is about 4 million and it is computationally very expensive to perform multiple CFD simulations to estimate correct parameters for the LPN. However, using this approach of estimating LPN parameters by separately solving the 0D equations without considering the 3D CFD equations, one can greatly reduce the number of simulations needed to obtain the desired boundary condition parameters. Typically, the target LPN parameters are obtained within three CFD runs using this approach. Each CFD run usually takes about 36 hours to complete on 64 processors.

3.2.6 Lagrangian Particle Tracking

Particle residence times were quantified using Lagrangian particle tracking. A high density of mass-less particles was released in the proximal region of each coronary vessel and particles were tracked over multiple cardiac cycles. Particles were assumed to be massless, and effects of diffusion were neglected owing to the short residence time of the particles in the computational domain. The advection scheme used a Runge–Kutta– Fehlberg integration algorithm with a maximum error tolerance of 10^5 and linear interpolation of the velocity data in space and time. As a measure of blood flow stagnation and recirculation, two quantities were calculated from simulations. First, we computed the percentage of particles remaining in the coronary vasculature after one, five and ten cardiac cycles. Second, we computed the total number of cardiac cycles required for all particles to completely wash out of the coronary vessels. Increased values of these two parameters indicate high recirculation time and flow stagnation, which is hypothesized to be linked to a higher risk of thrombosis.

3.2.7 Geometric Parameters and Aneurysm Shape Index

Three geometric parameters were determined from the patient specific models. The first was the maximum aneurysm diameter. The second was an aneurysm shape index, which we defined to classify aneurysm geometries on a continuous scale from more saccular to more fusiform. A representative aneurysm length was defined as the ratio of total aneurysmal volume to maximum aneurysmal area. The total aneurysm volume included all regions in the coronary arteries in which the diameter was greater than a Z-score value of zero. The aneurysm shape index was then defined as the non-dimensional ratio of the aneurysm length to the maximum aneurysmal diameter. A high aneurysm shape index indicates a more fusiform shape, while low shape index value indicates a more saccular shape. The third, aneurysm sphericity (Ψ), was defined using the following equation:

$$\Psi = \frac{\pi^{\frac{1}{3}}(6V)^{\frac{2}{3}}}{A}$$

where V is the aneurysm volume and A is the surface area. Low aneurysm sphericity indicates a more fusiform shape while higher aneurysm sphericity indicates a more saccular shape, where $\Psi = 1$ is a perfect sphere.

3.2.8 Hemodynamic parameters:

In addition to particle tracking**,** several additional hemodynamic parameters were computed, including WSS, WSSG, and OSI. Wall shear stress is computed in a post-processing step from the velocity and pressure fields of the Navier–Stokes solution. Rearranging the weak form in equation (1), with velocity and pressure solutions $v^i = \sum_A N_A v^i_A$ and $p = \sum_A N_A p$ we have

$$\int_{\Gamma_g} \vec{w} \cdot t d\tau = \int \vec{w} \cdot \rho(\tilde{v}_{,t} + \tilde{v} \cdot \nabla \tilde{v} - f) d\Omega + \int \nabla \vec{w} : (-\tilde{p} I + \tau) d\Omega - \int_{\Gamma_h} \vec{w} \cdot t d\tau$$

The weighting function, w is non-zero only at the surfaces where the WSS is to be computed. Choosing w to be the surface shape functions, we solve for the boundary tractions.

Two additional quantities of interest are derived from the WSS solution, τ(x,t). First, OSI is defined as

$$\mathrm{OSI} = 0.5\left(1 - \frac{\int_0^T \tau(x,t)}{\int_0^T |\tau(x,t)|}\right)$$

and is an indicator of the directionality of the flow[66]. OSI has minimum value of 0, corresponding to uni- directional traction, and maximum value of 0.5, corresponding to zero mean traction with equal time spent in both directions.

Wall shear stress gradients quantify the spatial variations in hemodynamic forces on the vessel wall. WSSG quantifies the magnitude of shear-stress gradients using the average wall shear direction and its in-plane (plane of the wall) normal. Off-diagonal coupled- derivatives, such as gradient of mean wall shear normal to the wall, are neglected since they have been shown to have little clinical relevance. The formulation for computation of WSSG is given below.

$$\tau^G(x,t) = \sqrt{\left(\left(\frac{\partial}{\partial s_1}\tau_1\right)^2 + \left(\frac{\partial}{\partial s_2}\tau_2\right)^2\right)}$$

From the velocities the tractions are given by $t_i = \sigma_{ij}n_j$ and the shear stress is given by $\tau_i(x,t) = t_i - (t_k n_k)n_i$. The WSS is further decomposed into two in-plane components along the unit vectors $s_1(x)$, which is parallel to the mean wall shear traction, and $s_2(x)$, which is orthogonal to s_1 in the plane of the wall. These two components of WSS are given by $\tau_1 = \tau.s_1$ and $\tau_2 = \tau.s_2$ and the corresponding WSSG is defined as the equation given above.

Finally the mean WSSG is obtained from

$$\bar{\tau}^G(x) = \frac{1}{T}\int_0^T \tau^G(x,t)dt$$

3.3 Results

3.3.1 Flow and pressure waveforms

Typical aortic flow and pressure waveforms are shown in Figure 3.3, and typical flow waveforms at the outlets of the LAD and RCA are shown in Figure 3.4, both for patient B. The coronary flow waveforms confirm that the lumped parameter boundary conditions captured the expected coronary physiologic features. The flow waveforms of both the LAD and RCA peaked during diastole, when coronary resistance is at a minimum. Simulated aortic pressure waveforms

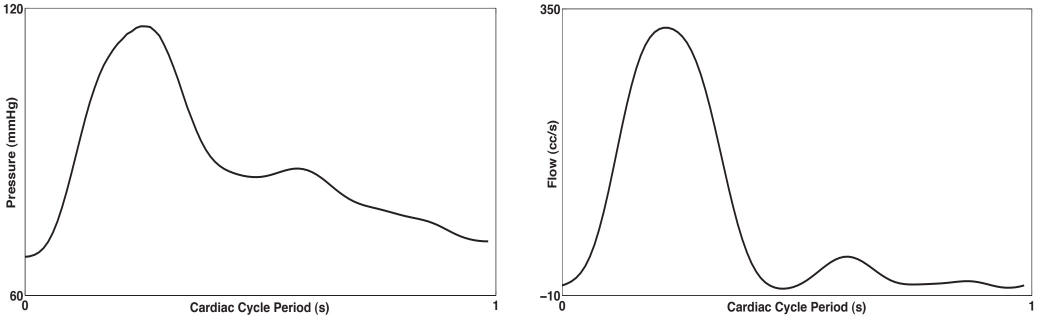

Figure 3.3: Typical aortic inflow waveform (right) and aortic pressure at the inlet (left) of patient B.

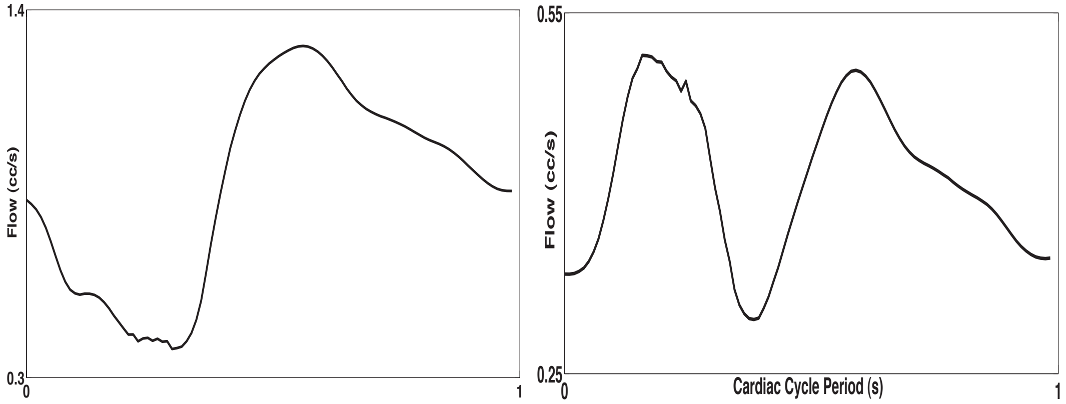

Figure 3.4: Typical simulated LAD (left) and RCA (right) flow waveforms in patient B, showing increased coronary flow during diastole.

matched the clinical systolic and diastolic blood pressure data for all patients, and shape agreed with clinical observation. As reported previously, there was no significant difference between the global flow and pressure waveforms of KD patients with aneurysms and the normal control model[51].

3.3.2 Hemodynamic parameters

Minimum coronary flow occurred during diastole, as expected, and this was particularly pronounced in the LCA. This led to persistently low velocities in the aneurysmal regions of the coronary arteries. Figure 3.5 compares the systolic, diastolic and time-averaged velocities in all patient-specific models. The presence of the aneurysms in patients A-E caused substantial flow stagnation and recirculation, with persistently lower velocities compared to control patient F.

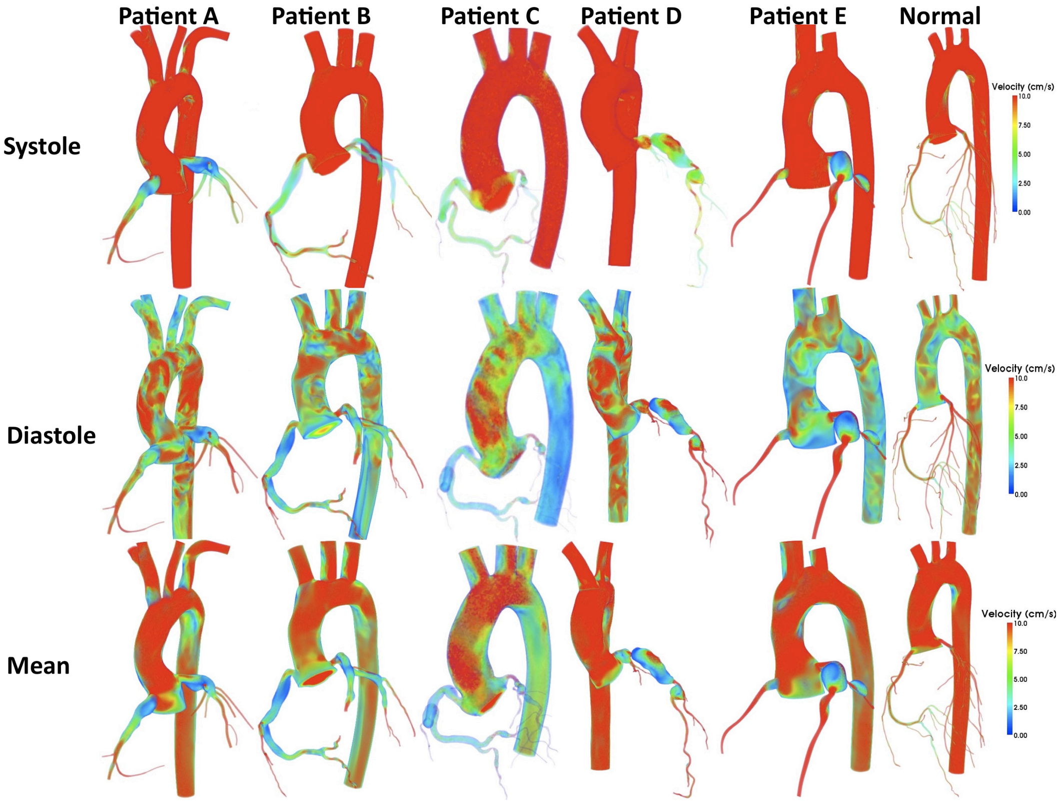

Figure 3.5: Volume rendered velocity magnitude for all patients during systole (top), diastole (middle), and time averaged (lower).

Contours of mean wall shear stress (WSS), oscillatory shear index (OSI), and wall shear stress gradient (WSSG) for all models are shown in Figures 3.6, 3.7, and 3.8, respectively. The WSS remains about an order of magnitude lower in the aneurysmal regions of patients A-F compared to vessels with no aneurysms (patient F and the RCA of patient E). Distal to the aneurysms, where coronary artery diameters return to normal, the WSS also returns to the normal range, verifying that the aneurysms cause only localized disturbances in hemodynamics. The aneurysmal regions are associated with higher than normal values of OSI (Figure 3.7). Distal to the aneurysms, as well as in Patient F and the RCA of Patient E, OSI values are near zero, indicating that the flow is unidirectional. Figure 3.9 shows WSS vs. time for one cardiac cycle at the location of maximum aneurysm diameter, indicating that aneurysmal regions are associated with an order of magnitude reduction of WSS in all subjects, with some patient variability in waveform shape.

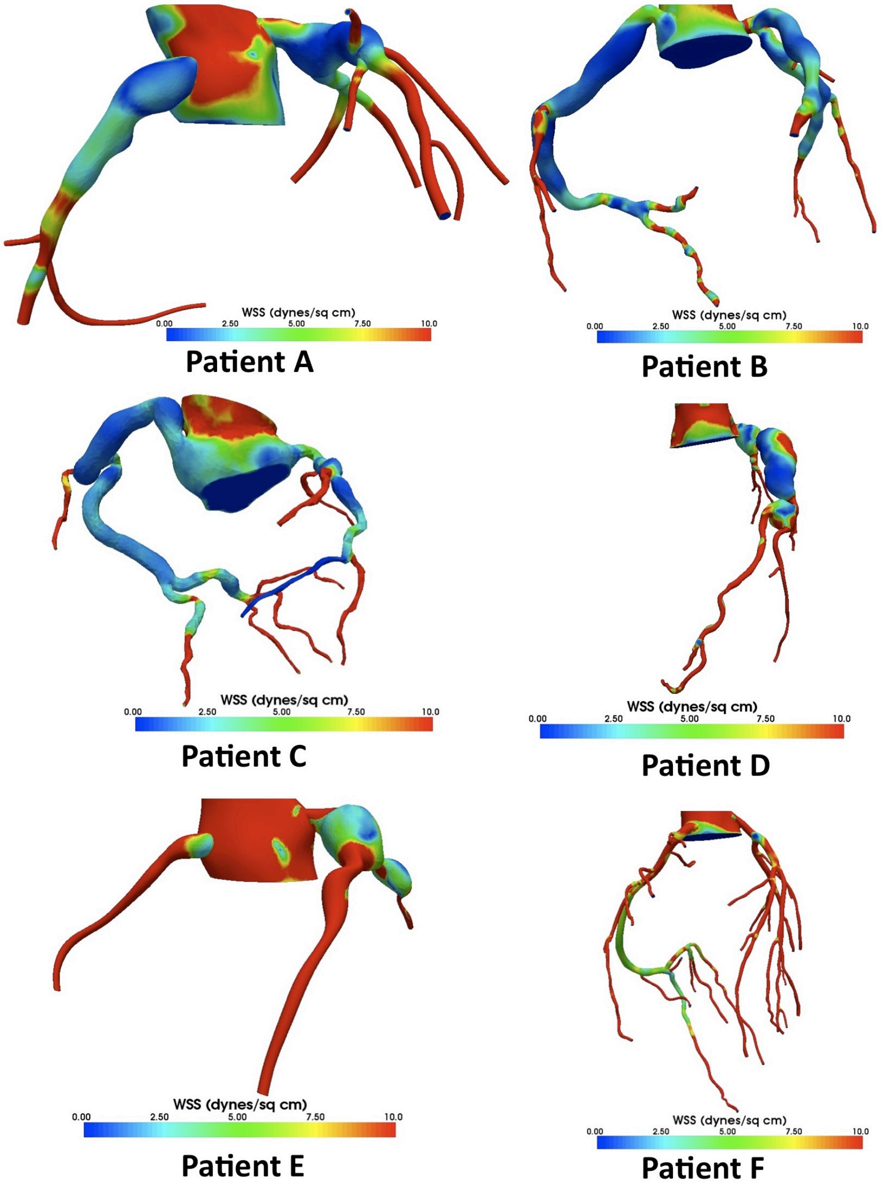

Figure 3.6: Mean wall shear stress in all patient specific models, showing lower values in aneurysmal regions, and large variation among patients.

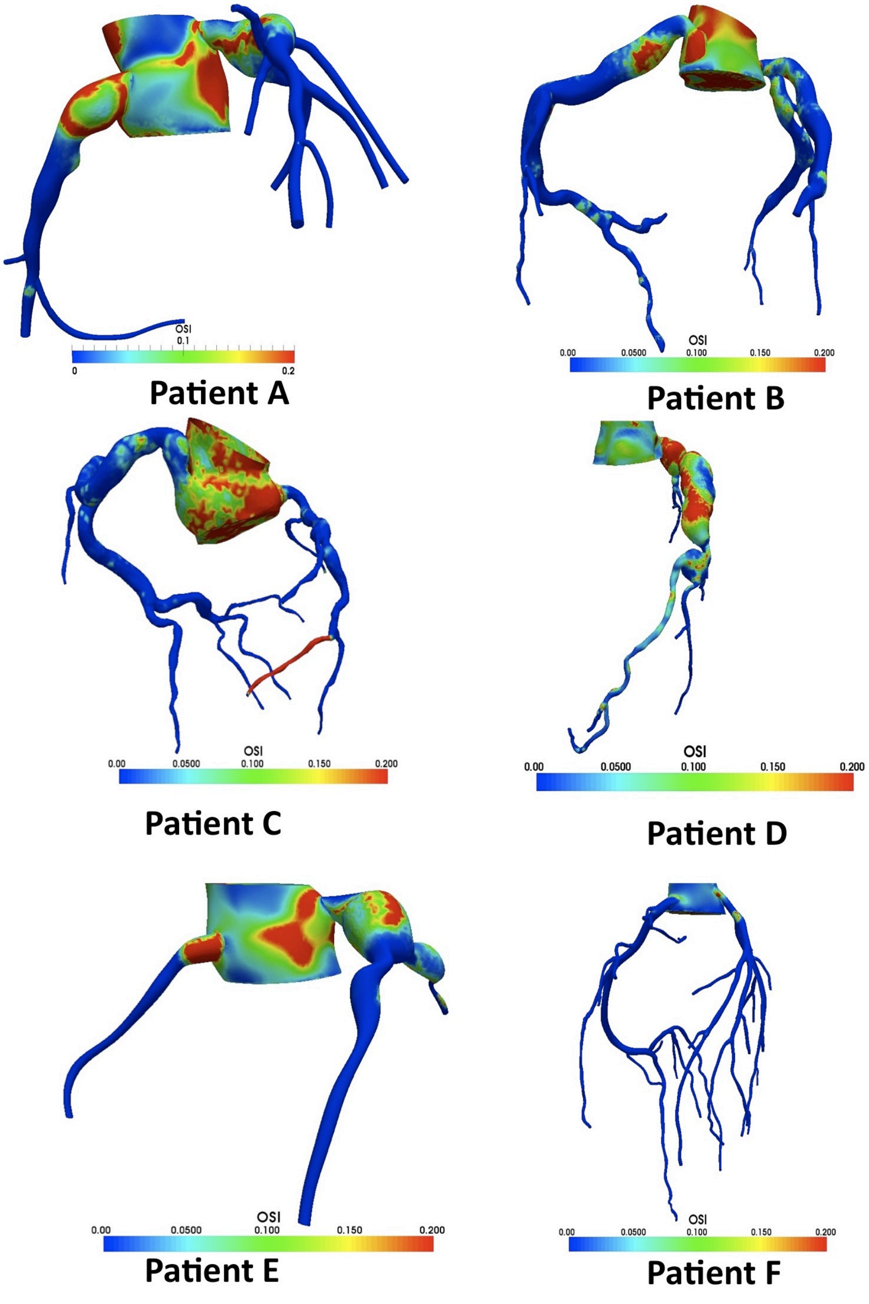

Figure 3.7: Oscillatory shear index in all patient models, showing increased OSI in aneurysmal regions compared to normal.

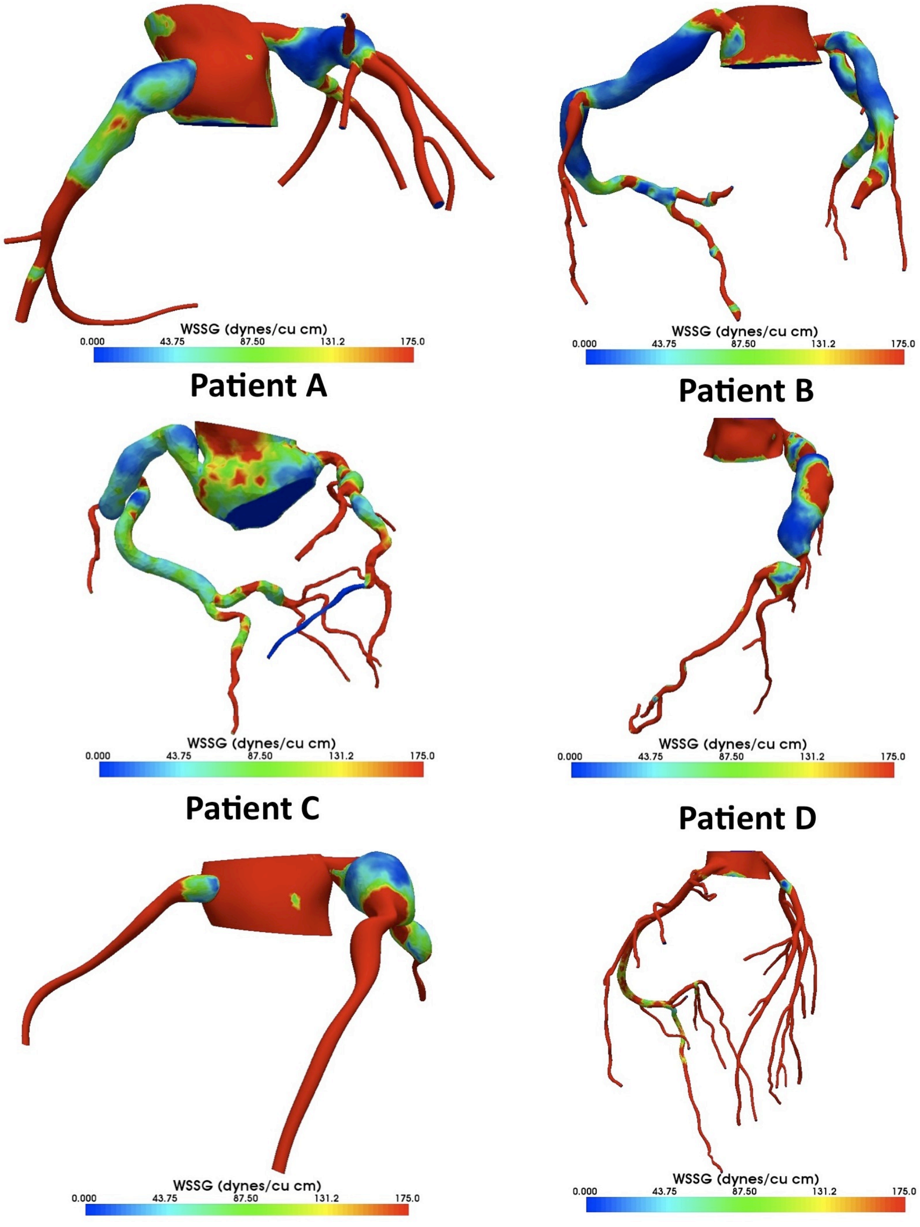

Patient A **Patient B**

Patient C **Patient D**

Patient E **Patient F**

Figure 3.8: WSSG in all patient models, showing increased WSSG variation in aneurysmal models compared to normal.

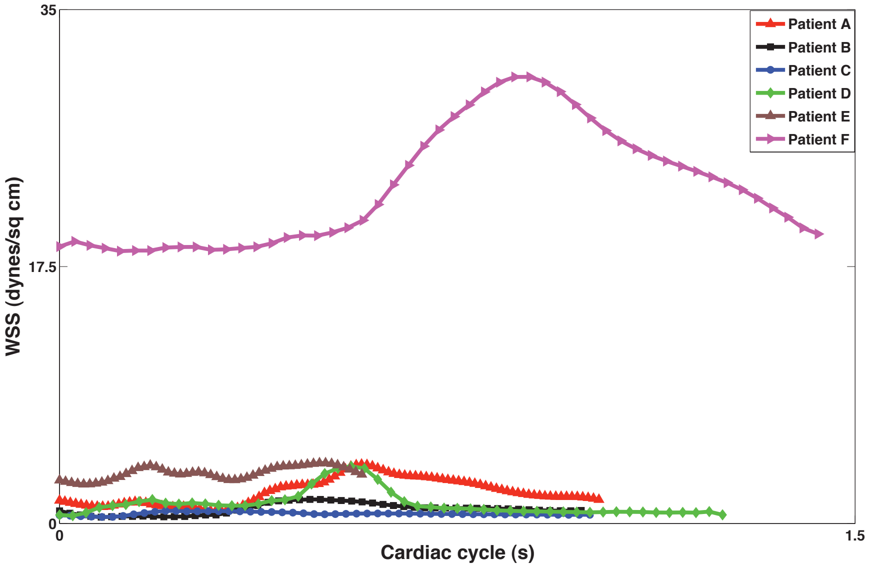

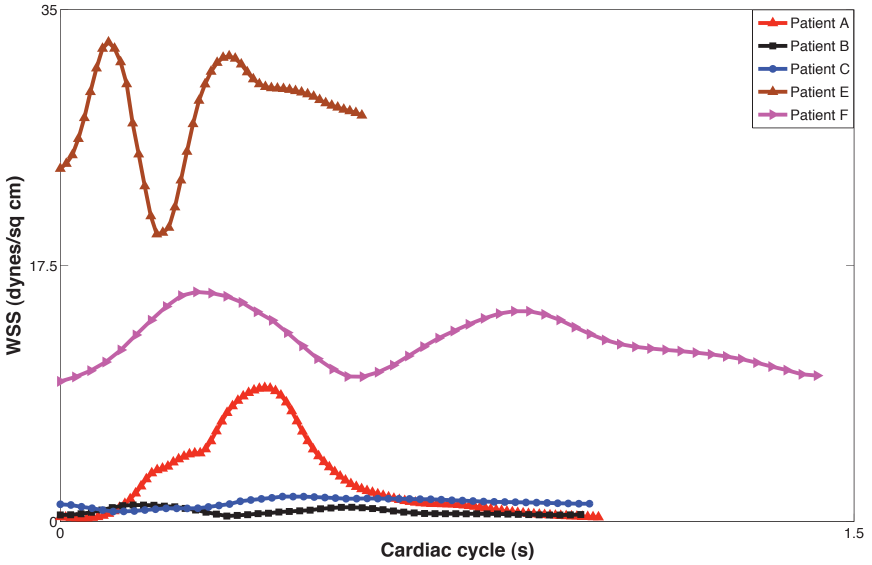

Figure 3.9: Wall shear stress vs. time, for one cardiac cycle, in all models shows much lower values in aneurysmal regions compared to normal in both LAD (top) and RCA (bottom).

3.3.3 Comparison with clinical data

Hemodynamic and geometric quantities were extracted from simulation results during post processing, and are summarized in Table 3.2, together with accompanying clinical outcomes data. There were a total of 6 patients, with 14 coronary arteries studied (including LAD, LCX, and RCA, Table 3.2). Patient D had a fully occluded RCA that was not modeled. LCX vessels for patients A, B, and E were quantified separately because they were aneurysmal, as listed in the table. For other patients (C, D, F) with normal LCX vessels, only the RCA and LCA parameters were quantified. There were 3 normal vessels considered, the RCA and LCA of patient F, and the RCA of patient E. Hemodynamic parameters in Table xx include the WSS at the maximum diameter, averaged WSS in the aneurysms, percent of particles remaining after 1, 5, and 10 cardiac cycles, and the number of cardiac cycles required for all particles to wash out of the model. Geometric parameters are maximum diameter, aneurysm shape index, and aneurysm sphericity.

Clinical outcomes data are listed in Table 3.3 as binary values (yes = 1, no = 0) for occurrence of thrombosis, myocardial infarction, surgical intervention, and percutaneous intervention.

Mean values of the above quantities were compared for the following groups of arteries. We first compared hemodynamics in normal arteries (N=3) vs. those with aneurysms (N=11). Next, to compare *within* the aneurysmal group, arteries with aneurysms were divided into: those with thrombosis (N=6) vs. those without thrombosis (N=5). Comparisons of mean values for these groups are summarized in Figures 3.10 and 3.11.

Aneurysmal arteries had significantly lower WSS than normal arteries (4.9 for aneurysmal vs. 20.9 for normal, $P<0.01$). Aneurysmal arteries also required significantly more cardiac cycles for particles to exit the domain (6.1 for aneurysmal vs. 1.1 for normal, $P<0.01$). Aneurysmal arteries had lower WSS gradients (37.6 for aneurysmal vs. 67 for normal) and higher

OSI (0.047 for aneurysmal vs. 0.01 for normal). Velocity fields also showed regions of stagnant flow that persisted throughout the cardiac cycle in aneurysmal regions, which were not observed in normal arteries.

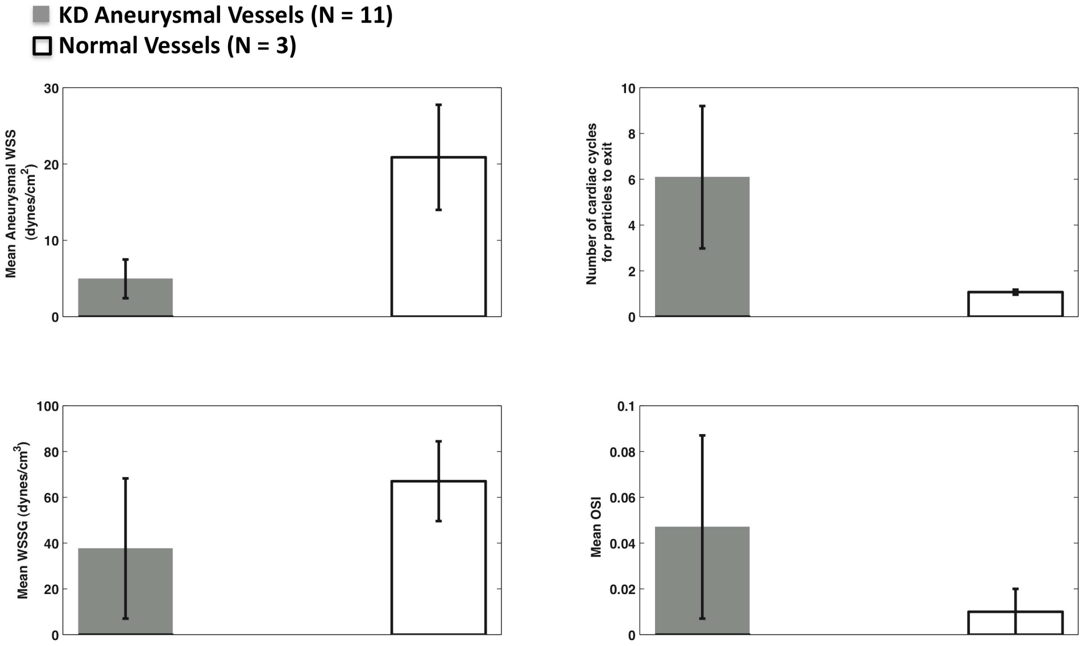

Figure 3.10: Comparison of hemodynamic parameters between aneurysmal (N = 11) and normal (N = 3) vessels in KD patients

Figure 3.11 compares geometric and hemodynamic parameters for the thrombosed and non-thrombosed groups. Aneurysms with thrombosis required twice as many cardiac cycles (mean 7.8 vs. 4.0, 95% difference) for particles to exit the aneurysm domain in simulation, and had 108% lower mean WSS (1.5 compared to 3.2 dynes/cm^2) at maximum diameter compared to aneurysms without thrombosis. WSS was also 32% lower for the thrombosis group when measured over the entire aneurysm. Mean WSSG was 45% lower while mean OSI was 67% higher in the entire aneurysm of the thrombosis group. Figure 3.11 compares the hemodynamic variation of hemodynamic parameters between the KD aneurysmal and the normal vessels, showing significant variation in these quantities.

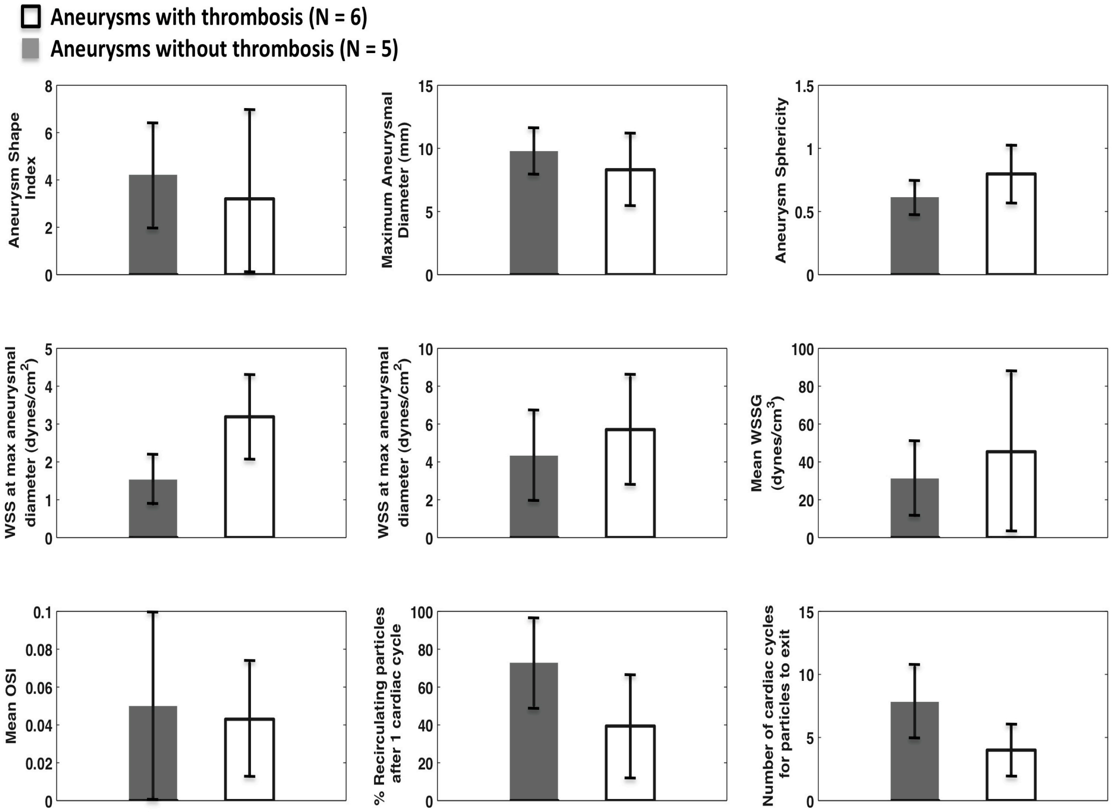

Figure 3.11: Comparison of hemodynamic and geometric parameters for thrombosed (N=6) and non-thrombosed (N=5) aneurysms in KD patients.

Thrombosed vessels had a 30% lower sphericity index than non-thrombosed vessels, and a 24% higher aneurysm shape index. There was a 15% difference between maximum diameters of arteries with thrombosis (10.8mm) and without thrombosis (8.8mm).

Following our performing simulations for patient B, this patient became symptomatic and was found through follow-up CT imaging to have developed thrombosis in both left and right coronary arteries. A comparison of WSS predicted by simulations is shown in Figure 3.12, together with pre- and post- thrombosis CT imaging data. We qualitatively observe that the locations of thrombosis formation correlate well with regions of lowest WSS in simulations in both left and right coronaries. We also observe that patient B had the highest particle recirculation times, and the lowest value of WSS in the RCA among all patients in the cohort (Table 3.2). This patient subsequently underwent coronary bypass surgery.

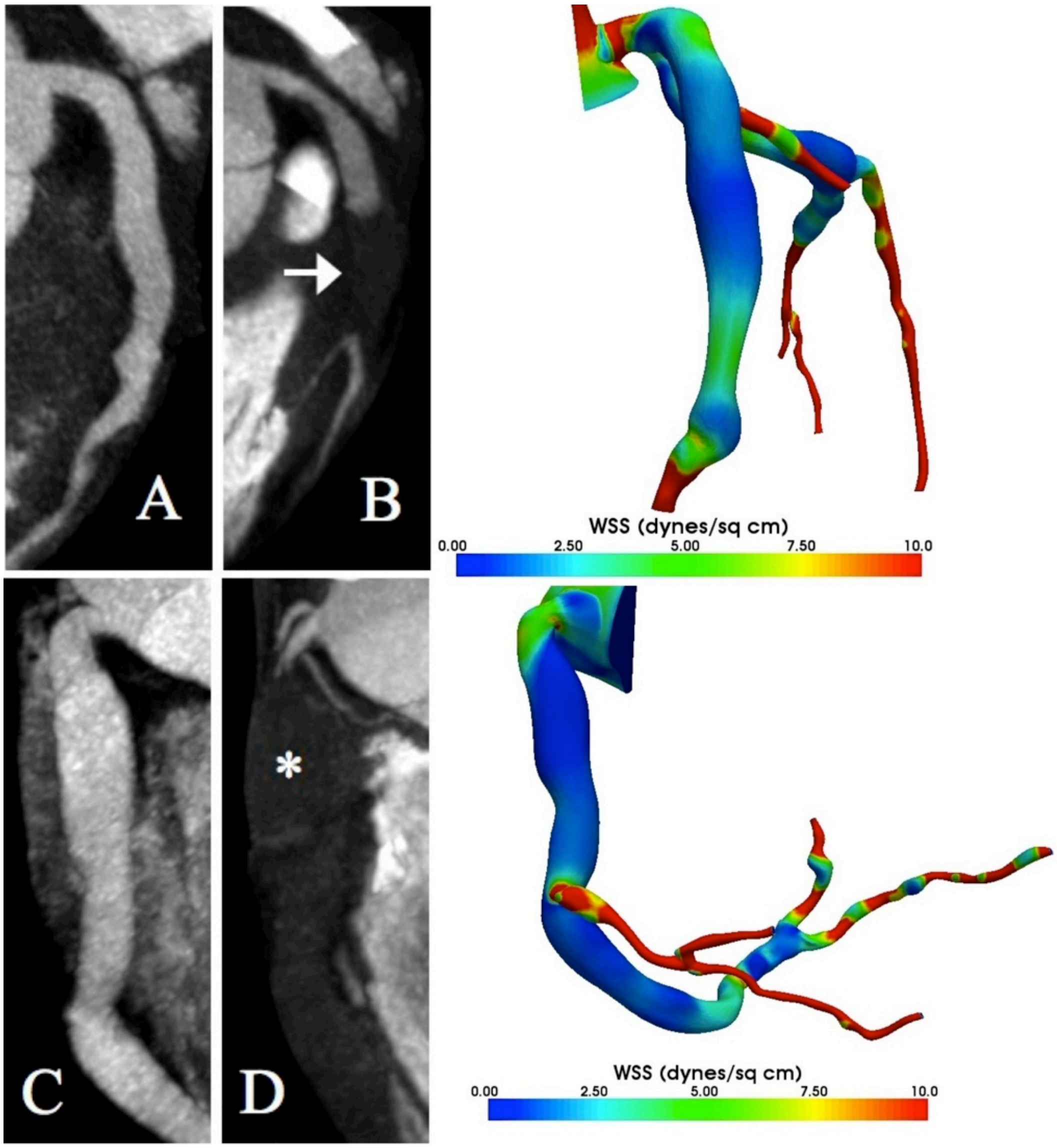

Figure 3.12: Pre-and post thrombosis CT imaging in patient B (left) and simulation results showing correlation between WSS predictions in simulation and locations of thrombosis.

Table 3.2: Representative hemodynamic and geometric parameters for the initial set of KD patients, with corresponding clinical outcomes data.

Patient ID	Vessel	Geometric Parameters			Hemodynamic Parameters						Thrombosis (yes/no)
		Max Aneurysmal Diameter (cm)	ASI	Ψ	Mean WSS at max diameter (dynes/ cm^2)	Mean WSS in aneurysm (dynes/cm^2)	Percent of particles after			Number of cycles particles recirculate	
							1 cardiac cycle	5 cardiac cycles	10 cardiac cycles		
A	LAD	1.14	1.38	0.83	2.75	3.2	32	0	0	4	1
A	LCX	0.64	1.27	0.75	2.47	4.53	18	0	0	3	0
A	RCA	1.08	1.38	0.77	3.45	4.05	28	0	0	5	0
B	LAD	0.95	4.93	0.68	1.65	2.22	82	51	0	10	1
B	LCX	0.7	5.35	0.56	1.13	3.18	75	41	0	8	1
B	RCA	1.03	6	0.51	0.92	2.8	98	63	16	12	1
C	LAD	0.87	1.58	0.48	1.33	7.86	71	10	0	6	1
C	RCA	0.96	9,86	0.48	1.85	3.09	82	17	0	7	0
D	LAD	1.18	6.09	0.61	1.43	6.72	79	16	0	7	1
E	LAD	1.03	1.25	0.88	3.5	6.6	49	0	0	3	0
E	LCX	0.44	2.34	1.11	4.72	10.21	20	0	0	2	0
E	RCA	0.16	-	-	-	28.07	5	0	0	1	0
Normal	LAD	0.35	-	-	-	20.2	9	0	0	1.2	0
Normal	RCA	0.32	-	-	-	14.35	14	0	0	1	0

Table 3.3: Clinical history of the cohort of patients.

Patient ID	Clinical Outcomes		
	Myocardial Infarction (yes/no)	Percutaneous Intervention (yes/no)	CABG (yes/no)
A	0	0	0
B	0	1	1
C	1	1	0
D	1	1	0
E	0	1	0
F	0	0	0

3.4 Discussion

Patient-specific modeling allows for computation of spatial and temporal variations in hemodynamic quantities that cannot be readily obtained through conventional clinical imaging modalities. Using computational modeling, we showed that the presence of aneurysms in the coronary arteries of KD patients leads to severely abnormal flow conditions, including low WSS and high particle residence times that appear to be linked to increased risk of thrombosis. This study is the first to apply patient-specific modeling to compare flow conditions in a cohort of KD patients using realistic aneurysm geometries. In agreement with our previous study, we identified significant order of magnitude differences between aneurysmal and normal coronary flow conditions. We also confirmed our previous finding that the presence of aneurysms does not change the global flow and pressure waveforms.

This study suggests several surprising relationships between flow conditions, aneurysm geometry, and clinical outcomes. First, simulations confirmed that flow conditions are markedly different among patients, even among those with similar aneurysm diameters. This calls into question the current clinical practice of using a single diameter measurement to determine thrombotic risk and the need for anticoagulant medication.

Second, our results suggest that hemodynamic parameters, or a combination of hemodynamic and geometric parameters, may be better predictors of thrombotic risk than maximum aneurysm diameter alone. When comparing differences between the thrombosis and non-thrombosis groups, the maximum diameter had the smallest percentage difference (15%) between the two groups of all the parameters examined. The largest percentage differences between the two groups were in WSS and number of cardiac cycles required for particles to exit the simulation domain. These findings are contrary to current AHA guidelines that rely solely on aneurysm diameter as a predictor of thrombotic risk[8]. While all but one aneurysm in this group was >8mm (Table 2), several large aneurysms had lower than average PRT and higher WSS.

Hence, criteria for anti-coagulation based on geometry alone may lead to unnecessary anticoagulation in patients with large diameter aneurysms as well as failure to anticoagulate patients at higher risk of thrombosis due to unfavorable hemodynamic parameters.

Furthermore, our results suggest that some patients such as patient B, may be at particularly high risk of thrombosis, and importantly may still be at risk even with systemic anticoagulation. Such patients may benefit from more additional medical therapy such as more intensive anticoagulation with a higher target INR and/or more intensive anti-platelet therapy and more intensive monitoring such as serial CT angiograms to assess for the presence of thrombus. In addition, the role of the new oral thrombin or Factor Xa inhibitors (dabigatran, rivaroxaban and apixaban) in KD remains to be determined. The assessment of patient-specific hemodynamics presented here may be of use in the design of clinical trials to evaluate these newer agents in KD patients.

Finally, our results suggest that fusiform aneurysms may confer a higher risk for thrombosis than previously appreciated, which goes counter to current clinical thinking that larger diameter, saccular aneurysms pose the highest risk. The sphericity index was lower for patients who developed thrombosis, suggesting that more fusiform aneurysms may actually have higher propensity for thrombus formation compared to saccular aneurysms. Additional patients with small and medium aneurysms are needed for comparison to strengthen these findings.

The correspondence between locations of low WSS for patient B and the subsequent location of thrombosis are a promising indicator of the predictive ability of the proposed simulation methodology. This patient had the lowest shear stress values and the highest particle residence times among all patients in the cohort. This patient’s unique history provided a valuable opportunity to compare simulation predictions with patient outcome.

Prior clinical studies have also examined the relationship between wall shear stress and aneurysm shape and have raised awareness of the importance of abnormal hemodyanmics. A

2007 study of Ohkubo et al. estimated WSS from flow wire measurements in 111 KD patients, classified into giant aneurysm, aneurysm, and normal groups[92]. WSS levels were correlated with the presence of thrombus detected by intravascular ultrasound. Over 90% of aneurysms were found at left coronary branching sites, with significantly reduced WSS in giant aneurysms with disturbed flow. However, the accuracy of measuring maximum velocity using flow wires remains a challenge, as WSS values were estimated by assuming laminar steady flow in a circular pipe, and thus could not fully account for the complex geometry or flow variations among patients.

We recognize several strengths and limitations to our study. First, the computational methodology represents the state of the art in cardiovascular modeling, employing physiologically realistic coronary boundary conditions and incorporating patient specific anatomy and clinical data. Second, this paper provides the first quantitative comparison of flow conditions in aneurysms of KD patients with subsequent patient outcomes. Third, these results suggest that a prospective clinical study is warranted to construct a clinical index based on simulation data that could be used to better select patients for anticoagulant therapy. Hemodynamic data could then be used in the future to replace or augment the current AHA guidelines, leading to better selection criteria for anticoagulation therapy in KD patients.

The major limitation of this study is the small sample size. A larger cohort and substantial computational effort will be required to demonstrate significance in comparisons of patients with and without thrombus. A limitation in expanding the cohort size and in creating a useful clinical tool is the time- and labor-intensive procedure for the model construction and simulations. In the future, these protocols could be streamlined by improved methods for automated image segmentation, further advances in high performance computing such as the use of GPU computing, and efficiency gains by improving the computational solver methodology. Limitations of the modeling methods include the use of rigid walls, a Newtonian flow model, and the assumptions required for assignment of lumped parameter boundary condition values. While previous studies have found differences in WSS between rigid and deformable wall simulations[84] with small WSS differences in the coronaries. However a full FSI study should be performed in future work using realistic coronary artery material properties to quantify these differences. While we have provided justification for the necessary assumptions related to our choice of coronary boundary condition values, a comprehensive uncertainty quantification study should be performed, following methods proposed in recent work[93]. Finally, because this was a retrospective study, some variability in medical treatment and timing of imaging studies was unavoidable. Although we note that all patients with aneurysms in the study were treated with anticoagulant therapy prior to the imaging studies with no major changes in treatment during the study period, we do not have clinical details regarding INR target, monitoring of INR, or patient compliance.

This study provided the first quantitative evidence that current AHA guidelines for determining thrombotic risk based on aneurysm diameter in patients with aneurysms caused by Kawasaki disease may be inadequate. More accurate patient selection for anticoagulation could avoid unnecessary treatment in some patients with large aneurysms, while identifying other at-risk patients who would benefit from systemic anticoagulation. A larger cohort is needed to construct a statistically significant clinical index to validate these findings.

Chapter 4

4. Preliminary Studies

4.1 Luminal Intensity as a measure of Recirculation

Patient specific computational simulations are typically an expensive process both from the perspective of time and computational requirements. When contrast agent is injected in a vessel, there is usually no decay in the mean luminal intensity if there is no abnormality in the shape of the vessel (no aneurysm or stenosis) and no obstruction in the blood flow. However, in the presence of abnormalities in the shape of the vessel caused either by stenosis or aneurysms, the luminal intensity obtained from the CT scan may decay in the regions distal to the abnormality. Recent work by Choi et al[94] showed that using the luminal intensity of the contrast agent in a CT scan of a coronary vessel, it is possible to estimate the degree of stenosis. In this work, it was shown that normal coronary arteries have little change in the value of the luminal intensity along the length of the coronaries. However, for a stenotic coronary artery, it was shown that there is a significant decrease in the luminal intensity. One may be able to use a similar method of luminal intensity calculation to estimate the degree of recirculation in the aneurysmal regions of the KD patients with coronary aneurysms.

For KD patients with coronary aneurysms, in the previous two chapters it was shown that the aneurysmal regions are associated with a high degree of recirculatory or sluggish flow. Contrast based X-Ray CT on these patients were performed by injecting a contrast agent[95]. The presence of the recirculatory or sluggish flow may cause the contrast agent to be trapped in the aneurysmal regions of the coronary arteries. This is likely to result in high intensity levels in the aneurysmal regions compared to the distal parts of the coronary arteries that have normal diameters. By correlating the luminal intensity along the length of the coronaries with a metric of recirculation time such as the cumulative exposure time (CET)[10, 51] as discussed in chapter two, it may be possible to estimate the degree of recirculation in the aneurysms without requiring a simulation for each patient.

An automated 2D level set segmentation method was implemented following the work of Sandhu et al[96] to perform 2D segmentation of the coronary geometry as shown in Figure 4.1. Using this method, the mean luminal intensity was calculated in the coronary arteries along the RCA and LAD of patient A at intervals of 2mm. Figure 4.2 shows the absolute values of the luminal intensity in both RCA and LAD. While both the plots show that the luminal intensity sharply decreases along the length of the RCA and LAD vessels, the decrease is much higher in case of the LAD compared to RCA. Figure 4.2 shows the normalized plot of the luminal intensity compared to the normalized CET values both plotted along the lengths of the RCA and LAD of patient A. The degree of flow recirculation in the LAD was higher than that in the RCA as indicated by the fact that the drop in CET values form the proximal aneurysmal to the distal normal parts was more severe in the LAD than in the RCA. The normalized mean luminal intensity also showed a correspondingly larger decrease in values of intensity levels are higher in the LAD compared to the RCA. Normalized CET and normalized luminal intensity had a high correlation coefficient (LAD – 0.91 and RCA – 0.68).

This is a novel approach of obtaining hemodynamic information directly from the CT scan. The luminal intensity measurements can be easily clinically obtained through conventional imaging modalities. Using the correlation of the mean luminal intensity with the hemodynamic metric for flow recirculation time, one can provide insights into the flow characteristics in the coronary artery aneurysms without performing expensive computational simulations.

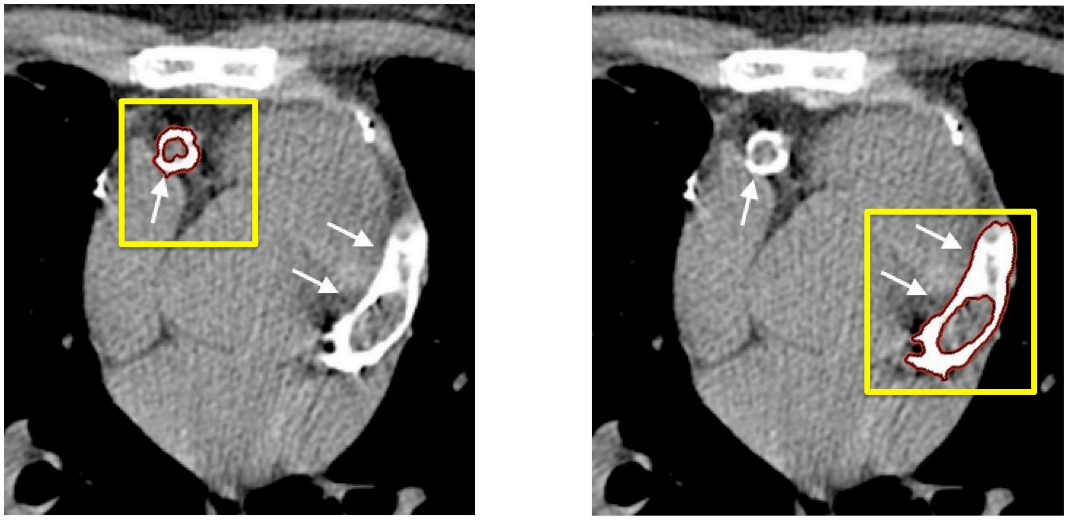

Figure 4.1: Automated level set segmentation using the zero level set function in RCA (right) and LAD (left).

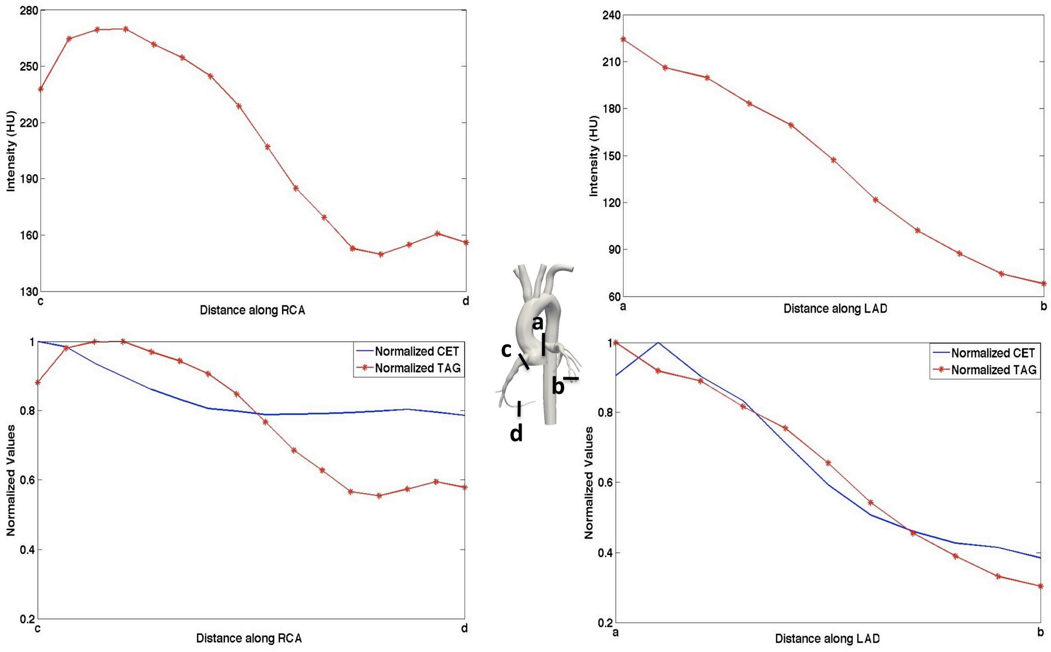

Figure 4.2: Mean luminal intensity along the length of RCA (top left) and LAD (top right). Normalized mean luminal intensity and normalized mean CET in RCA (bottom left) and LAD (bottom right) showing a strong correlation between recirculation time and high luminal intensity in the aneurysmal regions. In all the plots, variation of parameters are obtained from points a to b in the LAD and c to d in the RCA, where distance is measured along the vessel centerline from the ostium.

4.2 Statistical Model for Thrombotic Risk Probability

Patient specific computational simulations in coronary arteries provide insights into the hemodynamic characteristics of KD patients with aneurysms that have not been established in previous research. In chapter 4, geometric quantities such as maximum aneurysmal diameter, aneurysm shape index and aneurysm sphericity were quantified along with local hemodynamic quantities such as WSS and particle recirculation were quantified for the cohort of KD patients and compared to the corresponding clinical outcomes. Results showed that there might be a correlation between several key geometric and hemodynamic quantities and the presence of thrombus formation. Statistical models may be used to uncover the relationships between the hemodynamic and geometric quantities and the risk of thrombosis[97]. However, in order to perform the statistical analysis in a statistically significant manner, a sufficiently large number of patient-specific simulations need to be performed.

Among the various statistical models, logistic regression[98] typically can serve as a good model to predict the risk of thrombosis based on the hemodynamic and geometric factors. The presence or absence of thrombosis in a patient can be quantified by a binary variable (y) with y=1 or 0 representing the occurrence or non-occurrence of thrombosis. The incidence of thrombosis (y) depends on the geometric and hemodynamic quantities denoted by the vector **x**. The probability of thrombus formation (y=1) can be modeled by logistic regression using the following equation.

$$P(y=1|\mathbf{x},\beta)=\frac{1}{1+e^{-(\beta_0+\sum_{j=1}^{d}\beta_j x_j)}}$$

The weight vector β in the above equation is obtained numerically using stochastic gradient ascent method[98]. Regularization was also used to avoid overfitting of the data.

However, in order to obtain statistically significant results for the probability of risk of thrombus formation, larger number of patient data with about 100 patients will be required. Despite the lack of statistical significance, an effort was made in the thesis to create a framework for carrying out statistical analysis by creating a JAVA based logistic regression routine. The routine was also embedded in Android App called Kawasaki Disease (Figure 4.3). As shown in Figure 4.3, the app consists of several fields where one can enter the geometric and hemodynamic parameters for a patient and on pressing the “Calculate Risk Probability” tab, the app runs the logistic regression code with the training of the weights of regression being performed with the database of existing geometric and hemodynamic data obtained from all the patient-specific simulations.

In order to test the probability of thrombotic risk using the limited simulation results logistic regression was performed using the data in Table 3.2. The corresponding weights were trained using stochastic gradient update rule that is given by the following equation.

$$\hat{\beta} = \mathrm{argmax}_{\beta} L - \mu||\beta||_2^2$$

where L = $\Sigma_{i:y=1}$ log(P(y=1|**x**,β) + $\Sigma_{i:y=0}$ (1- log(P(y=1|**x**,β)) is the log-likelihood function, $||\beta||_2^2$ is the additional penalty function prescribed for regularization and the constant μ represents the trade-off between the log-likelihood and the penalty function. Using, these relationships, the final update rule for β is as follows.

$$\beta_j := \beta_j + \lambda \frac{\partial}{\partial \beta_j}[L - \mu \sum_j \beta_j^2] := \beta_j + \lambda[(y - P(y = 1|x, \beta)x_j - 2\mu\beta_j]$$

The parameter λ is called the learning rate and is adaptively chosen during the iteration process. Based on the results of geometric and hemodynamic data on 14 vessels for 5 patients in Table 3.2, a subset of 12 vessels were chosen to train the weights using logistic regression and stochastic gradient method[98]. The estimated weights were then used to compute the thrombotic risk probability of two remaining vessels – one of the vessels being the RCA of patient B and the other being the LAD of patient E. Table 4.1 lists the risk of probability of thrombus formation using both hemodynamic and geometric parameters. Although, the probability values are not statistically significant, usage of the hemodynamic parameters along with the geometric parameters gives a much better estimate for the thrombotic risk probability. As shown in Table 4.1, RCA of patient B underwent thrombosis based on the clinical records. While the probability risk of thrombosis based only on the geometry was 0.41, using both the geometric and hemodynamic parameters it was almost twice with a probability of 0.74. Table 4.1 also reveals that the LAD of Patient E did not undergo thrombosis despite having large aneurysms. The probability of thrombosis for this vessel using only geometry was 0.41 while it was lower when both hemodynamics and geometry was considered with a probability of 0.38. Although the numbers for probabilities are not conclusive to determine the thrombotic risk of a KD patient with aneurysms, they show that hemodynamic factors along with the geometry may play a significant role in the construction of a clinical risk index.

The lack of a larger number of patient-specific geometric and hemodynamic data led to statistically insignificant results from the logistic regression. In order to perform the analysis with a statistically significant outcome (p-value less than 0.05), at least 100 KD subjects need to be considered to obtain the geometric and hemodynamic data with a sufficient number of patients (~25%) developing thrombosis. Furthermore, sensitivity and specificity of the probability values need to be performed to test the discriminative accuracy of the method.

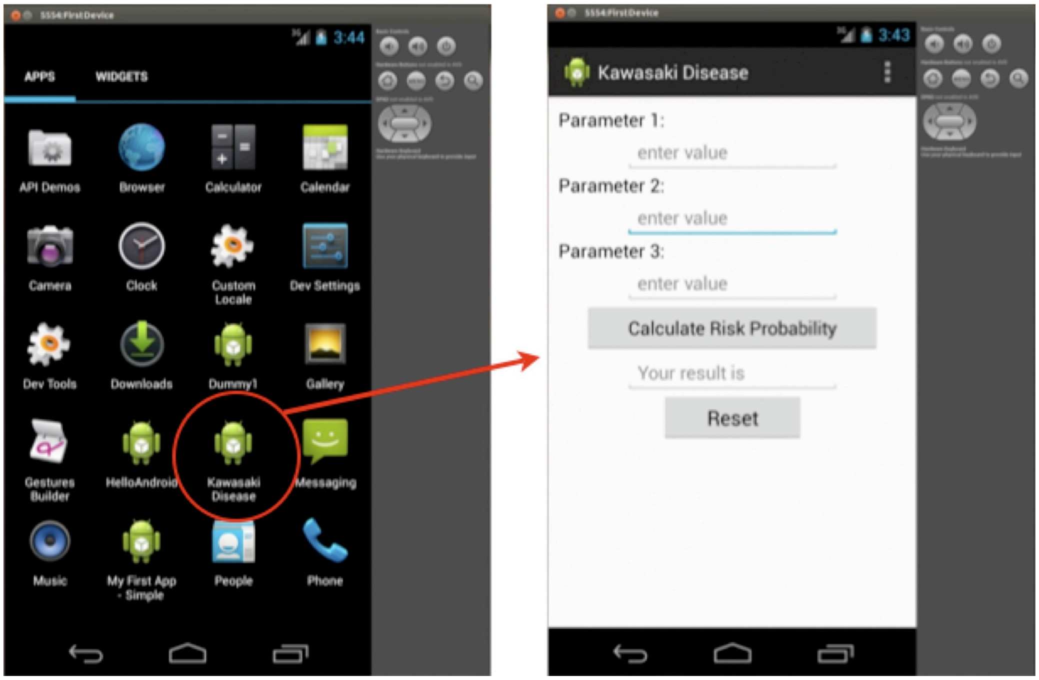

Figure 4.3: Kawasaki Disease App on the Android Emulator performing the logistic regression.

Table 4.1: Probability of thrombus formation using geometric and hemodynamic parameters obtained using logistic regression with the cohort of patient-specific simulations.

Vessel	Thrombosis Probability using Geometry and Hemodynamics	Thrombosis Probability using Geometry	Thrombosis Probability using Hemodynamics	Actual Clinical Record of Thrombosis
Patient B - RCA	0.74	0.41	0.71	1
Patient E - LAD	0.38	0.41	0.34	0

4.3 Effect of Deformable Wall

All patient specific simulations have been performed in this thesis using the assumption of rigid vessel wall. However, arterial walls are deformable and they typically undergo deformation in membrane mode, which causes variation in the flow, and pressure waveforms. To assess the impact of wall deformation, preliminary simulations were performed using fluid structure interaction methods of Figueroa et al[20]. Following this method, a linearized kinematics approach was used to simulate the coupled fluid structure system using a monolithic coupling[20, 25] assuming small wall displacements. The method is computationally much less expensive compared to conventional Arbitrary Lagrangian Eulerian (ALE) method[81, 84]. However, this approach yields correct results only for small wall displacements (less than 10% of the original diameter). A membrane formulation is used to describe the mass and stiffness of the solid.

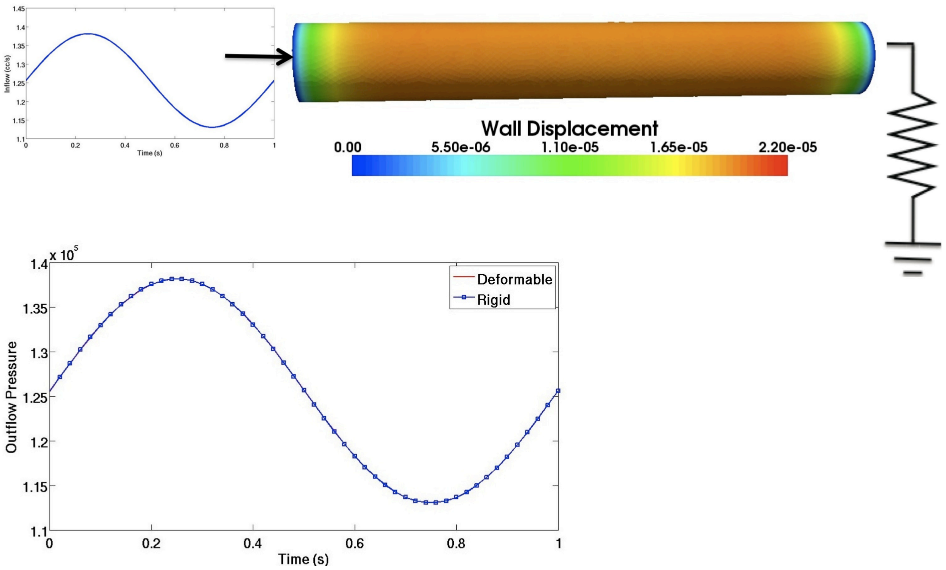

Figure 4.4: Sinusoid flow waveform being applied with resistance boundary condition at outlet. Maximum computed wall displacement matched theoretical value. No difference in outlet pressure waveform due to high elastic modulus and low thickness.

Firstly a model validation problem was performed on a cylinder of radius, a=0.2 cm, a prescribed uniform thickness, h=0.002 cm and an elastic modulus, E = 10^{10} dynes/cm^2. A sinusoid inflow waveform of $Q = 1.256 + 0.1256\sin(2\pi t)$ cc/sec was applied at the inlet and a resistance boundary condition with resistance, R = 100,000 dynes-sec/cm^5 is applied at the outlets as shown in Figure 4.4. The geometric and the structural parameters such as the radius, thickness and elastic modulus were not in the physiologic range. However, the values were in the range such that theoretical wall displacements can be obtained using linear theory. The hoop stress ($\sigma_{\theta\theta}$) for the thin wall cylindrical structure is obtained by $\sigma_{\theta\theta} = Pa/h$ where P is the normal pressure, a is the radius of the cylinder and h is the thickness of the cylinder. Further using $\sigma_{\theta\theta} = E\Delta r/a$, the theoretical wall displacement can be easily obtained. Figure 4.4, shows that due to high value of the elastic modulus, there was no difference in the pressure waveform at the outlet between the rigid and the deformable simulation. However, the computed wall displacements at maximum pressure difference of P = 12560 dynes/cm^2 matched well with the theoretical wall displacements of 2.3x10^{-5} cm obtained using linear theory.

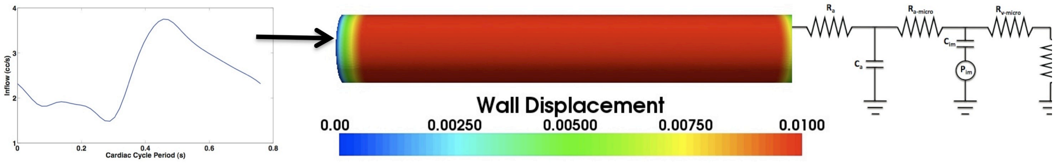

Figure 4.5: Typical coronary flow waveform applied at inlet and coronary boundary condition applied at outlet. Significant wall displacements are observed during systole.

In the second case, a more physiologic simulation was performed with a typical coronary flow waveform being applied at the inlet of a cylinder of radius, a = 0.3 cm, a uniform thickness, h = 0.03 cm and an elastic modulus, E = 4.07x10^6 dynes/cm^2. The geometric and material properties were chosen corresponding to a typical coronary artery[56]. At the outlet, a typical coronary boundary condition was applied as shown in Figure 4.5. In this case, the presence of the deformation produced an additional compliance in the vessel. Figure 4.5 shows that the presence of compliance causes significant changes in the flow and pressure waveforms at the outlets between the rigid and the deformable simulations. The pressure waveform is significantly damped and phase shifted. The flow waveform is also affected during systole and diastole compared to the rigid simulation due to the additional compliance imposed by the vessel wall.

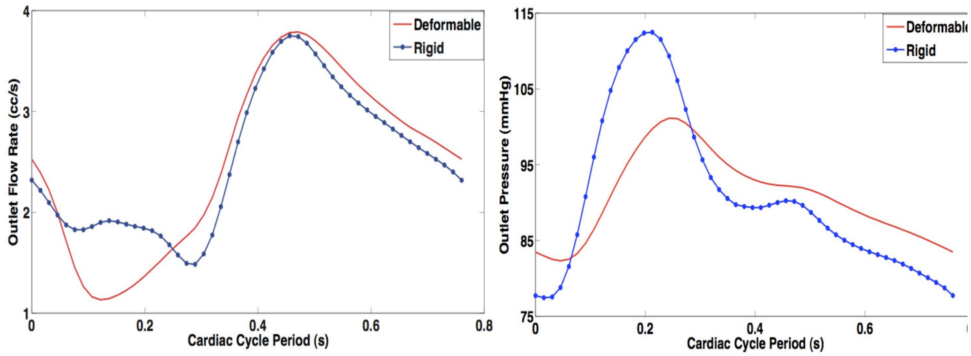

Figure 4.6: Effect of physiological deformation causes increased compliance in the vessel with changes in the peak and phase shift of both flow (left) and pressure (right) waveforms when compared to rigid simulations.

One of the major limitations of this method is the absence of non-uniform wall properties in the deformable simulations. A typical patient specific KD model involves the coronary vasculature, the aorta and the upper subclavian vessels each of which have different wall properties. Non-uniform wall properties need to be applied in future work.

Chapter 5

5. Conclusions and future work

5.1 Conclusions

In this dissertation, we presented the first patient specific hemodynamic simulation on KD patients with coronary artery aneurysms. Hemodynamic simulation in the coronary arteries are challenging because of the physiology of coronary circulation. We implemented a robust finite element framework to perform coronary simulation using the state of the art computational methods following work done by previous research groups[19, 32, 34]. We showed that the lumped parameter boundary conditions were crucial in simulating physiologically realistic flow and pressure profiles in the coronary arteries. The single patient case study discussed in chapter 2 revealed highly altered local hemodynamic characteristics in the aneurysmal regions compared to the normal model, although there were no differences in the global flow and pressure waveforms. The local hemodynamic features in the aneurysms cannot be obtained by conventional imaging modality and simulation provides a non-invasive method to compute these quantities from the CT scans of KD patients with coronary aneurysms. The aneurysms caused regions of abnormally low WSS and high recirculation compared to the normal model with the hemodynamics being in the level that is known to cause thrombosis and inflammation as described in chapter 2.

In order to perform patient-specific coronary simulations, appropriate tuning of the parameters in the LPN is essential. The outlet boundary conditions for the coronary simulations consisted of a combination of Windkessel RCR circuit for the non-coronary outlets and custom coronary circuit connected to an external lumped parameter heart model for the coronary outlets. Tuning all the parameters of the LPN on a patient-specific basis to match the appropriate clinical data can be challenging and might need multiple expensive CFD simulations. We devised a tuning algorithm as described in chapter 3 which is a combination of 0D and 0D-3D tuning to obtain the correct parameters for the LPN at relatively cheap computational cost. The CFD simulations done on multiple patients using this method were able to capture the patient's clinical parameters correctly as described in the study.

The simulations performed on multiple patients revealed several non-intuitive relationships between the hemodynamics, aneurysm geometry and clinical outcomes. Current AHA guidelines for patient management of KD patients with coronary aneurysms are solely based on maximum aneurysmal diameter. However, the simulation results on multiple patients in chapter 3 showed that aneurysms with similar diameter had markedly varying hemodynamics and different clinical outcomes. A combination of hemodynamic parameters and other geometric parameters in addition to the maximum aneurysmal diameter were better predictors of thrombosis than maximum aneurysmal diameter. Results also suggested that KD patients with fusiform coronary aneurysms had higher propensity for thrombus formation than those with sacculer aneurysms, which is contrary to the current clinical thinking. The findings questioned the current treatment strategies of anticoagulation therapy for KD patients with coronary aneurysms.

The thesis provided a means to risk stratify a group of KD patients with coronary aneurysms according to the risk of a clinical fatality. This presents the first systematic characterization of hemodynamic and geometric features of coronary aneurysms in KD patients. Simulations provide a non-invasive method to obtain critical hemodynamic parameters in the coronary arteries on patient-specific basis. The multiscale simulation framework developed in this thesis can be used in simulating patient-specific coronary flow in other coronary artery diseases including coronary artery bypass grafts (CABG).

5.2 Future work

5.2.1 Closed loop multiscale coronary flow simulation with deformable walls

The multiscale boundary condition used in the thesis relied on an open loop configuration where the heart model is explicitly coupled to the coronary boundary conditions. However, the physiologic realism can be improved even further in the simulation of coronary flow. Recently more advanced implementation of closed loop lumped parameter network model of the coronary circulation has been implemented that includes venous feedback[15]. The LPN model for the closed loop model implicitly couples the coronary boundary conditions with the aorta and the sublavian branches (in the upper aorta). Such boundary conditions have been successfully applied to adult coronary artery bypass patients[15] where the inlet aortic flow waveform was imposed directly by the lumped parameter heart model and no MRI derived aortic flow waveform is necessary. The parameters of the closed loop LPN model can be iteratively tuned using robust optimization method and can be applied to patient-specific simulations of KD patients with coronary aneurysms. Furthermore, the coronary arteries undergo substantial motion during ventricular contraction and relaxation as they are located on the myocardium[47]. Hence incorporating deformable vessel walls with variable wall properties in the computational modeling using fluid-structure interaction methods[81] are also necessary in simulating realistic flow conditions in the coronary arteries.

5.2.2 Development of a risk stratification index

A risk stratification index may be developed using quantitative data obtained from simulations. The index may improve guidelines for clinical decision-making and has the potential to patient outcomes. However, in order to construct such a risk index, a larger number of patient-specific simulations need to be performed and the simulation results should be correlated to the clinical outcomes of the patients in a statistically significant manner. Despite known relationships between abnormal hemodynamic parameters and the incidence of thrombus[73, 75] it is unclear how strongly these parameters influence the formation of thrombus. Advanced statistical analysis should be performed on large number of simulation results to uncover the detailed relationships between hemodynamics and thrombosis. The statistical relationship may be used in performing better patient management for KD patients with coronary aneurysms by ranking them according to thrombotic risk, which may enable clinicians in deciding on anticoagulant therapy effectively.

5.2.3 Application of uncertainty quantification

The patent-specific coronary flow simulations are performed under a number of assumption based on literature data[51]. These assumptions may influence the results of the simulations significantly. In order to address the sensitivity of the simulation results systematic uncertainty quantification should be performed to obtain confidence intervals of the simulation results[93]. These methods will be able to demonstrate the reliability and robustness of simulation results. Furthermore, the effect of exercise on the clinical parameters and the boundary conditions of the patient-specific simulations should be considered.

5.2.4 Validation using experiments

The hemodynamic conditions such as the coronary flow and pressure waveform obtained from simulations also need to be validated against in-vivo catheter flow and pressure wire data for multiple patients. The validation will increase the reliability of the simulation results. Besides this, the cellular level response of the endothelial cells in response to the abnormal hemodynamics should be considered. Thrombosis formed in the coronary aneurysms of KD patients may be caused by several biochemical processes in addition to the abnormal hemodynamics[75]. In vivo or in vitro experiments performed on the endothelial cells under the flow conditions similar to those in the aneurysmal models may be able to reveal the underlying biological processes involved.

5.2.5 Application of clot models

Recent developments in the usage of mathematical clot models in modeling thrombosis may be further used in the coronary simulations of KD patients with coronary aneurysms. Clot models have been successfully implemented in CFD simulations in earlier studies related to vessel injury[79]. However, implementing a clot model with a three dimensional patient-specific coronary simulation is computationally expensive because of widely differing time scales. Advanced GPU computing may be used to carry out faster computation to simulate clot formation in a patient-specific geometry in a coupled CFD simulation of KD patients with coronary aneurysms.

Appendix I

This appendix provides the equations for the lumped parameter boundary conditions that were coupled to the finite element flow solver, following previous work. First, the equations for the lumped parameter heart model are provided. The heart model was used off-line to provide intra-myocardial pressure information for the lumped parameter coronary boundary conditions. Second, the lumped parameter coronary boundary conditions are described in detail.

Heart Model

Phase I: t = 0 to t_1 – Isovolumetric Contraction (Valve 1 and valve 2 closed)

$$\frac{dQ_1}{dt} = 0$$
$$\frac{dV_V}{dt} = 0$$
$$P_V(t) = E(t)(V_V(t) - V_0)$$

Phase II: t = t_1 to t_2 – Ejection (Valve 1 closed and valve 2 open)

$$\frac{dQ_1}{dt} = 0$$
$$\frac{dV_V}{dt} = -Q_a$$
$$P_V(t) = E(t)(V_V(t) - V_0)$$

Phase III: t = t_2 to t_3 – Isovolumetric relaxation (Valve 1 and valve 2 closed)

$$\frac{dQ_1}{dt} = 0$$
$$\frac{dV_V}{dt} = 0$$
$$P_V(t) = E(t)(V_V(t) - V_0)$$

Phase IV: t = t_3 to t_4 – Filling (Valve 1 open and valve 2 closed)

$$\frac{dQ_1}{dt} = \frac{1}{L_{AV}}[P_A - R_{AV}Q_1(t) - E_2(t)(V_V(t) - V_0)]$$
$$\frac{dV_V}{dt} = Q_1(t)$$
$$P_V(t) = E(t)(V_V(t) - V_0)$$

In the above equations, E(t) is the patient specific elastance function, $Q_1(t)$ is the flow rate through valve 1, $V_V(t)$ is the ventricular blood volume, $P_V(t)$ is the ventricular pressure, P_A is the atrial pressure, R_{AV} is the atrio-ventricular valvular resistance and L_{AV} is the ventriculo-arterial inductance.

Valve 1 is open when $P_A > P_V(t)$ and is closed when $P_A \leq P_V(t)$.

Valve 2 is open when $Q_A > 0$ and $\frac{dQ_A}{dt} > 0$ and is closed when $Q_A = 0$ and $\frac{dQ_A}{dt} < 0$ where Q_A is the flow rate through valve 2.

The Intra-myocardial pressure is $P_{im}(t) = \lambda_1 P_{LV}(t) + \lambda_2 P_{RV}(t)$ where $P_{LV}(t)$ and $P_{RV}(t)$ represent the pressure of the left and the right ventricles respectively.

For the left coronary artery outlets, $\lambda_1 = 1.0$ and $\lambda_2 = 0.0$, since these outlets supply blood only to the left ventricle. However, the right coronary arteries supply blood to both the right and left ventricles, with the longest branch of the RCA supplying blood to the left ventricle, and the others supplying the right ventricle. The weights of the myocardial pressure for the right coronary artery outlets are therefore calculated based on the outlet areas of the branches in the RCA, resulting in a right:left perfusion ratio of approximately 7:3 (i.e. $\lambda_1 = 0.3$ and $\lambda_2 = 0.7$). Figure A1 shows the right and the left ventricular pressures, as well as the pressure volume loop for the patient under consideration.

MATLAB Code Snippet for Heart Model during Ejection Phase (Phase II)

```
% Ejection
options = odeset('Events', ...
        @(t,y)aortic_valve_closing_test(t, y) ...
        ,'Maxstep',0.01);
[t_ode_soln,y_ode_soln,t_event,y_event,i_event] = ode23( ...
    @(t,y)dydt_mitral_valve_closed_aortic_valve_open(t,y), ...
    [t_soln(end) final_t], [Q_la_soln(end) v_lv_soln(end)], options);
t_soln = [t_soln; t_ode_soln(2:end)];
Q_la_soln = [Q_la_soln; y_ode_soln(2:end,1)];
v_lv_soln = [v_lv_soln; y_ode_soln(2:end,2)];
t_ejection = size(t_ode_soln,1);
if cycle ==1
  for i=1:t_ejection
  e_sys(i) = (p_a(t_ode_soln(i)) + scale_aortic_flow*Q_a(t_ode_soln(i))*Rvart + dQadt(t_ode_soln(i))*Lvart)/(elastance(t_ode_soln(i))*(y_ode_soln(i,2)-v_lv0));
  end
  max_value_e_sys = max(e_sys)
  E_sys_max = mean(e_sys)
end
for i=1:t_ejection
p_lv(i) =scale_e_sys*E_sys_max*elastance(t_ode_soln(i))*(y_ode_soln(i,2)-v_lv0);
end
p_lv = p_lv';
```

```
    if cycle ==1
    p_lv_soln = p_lv;
    else
    p_lv_soln = [p_lv_soln; p_lv(2:end)];
    end
    clear p_lv
    E_dias_max = e_sys (end)
      vlv_plot = [vlv_plot; y_ode_soln(2:end,2)];

%       end
%Aortic Valve closing test
 function [value,stop,dir] = aortic_valve_closing_test(t_current, y_current)
    scale_aortic_flow = 1.344;
    value = scale_aortic_flow*Q_a(t_current);
   stop = 1;
   dir = -1;
% ODE function
function dydt = dydt_mitral_valve_closed_aortic_valve_open(t_current,y_current)
scale_aortic_flow = 1.344;
dydt(1,1) = 0;
dydt(2,1) = -scale_aortic_flow*Q_a(t_current);
```

MATLAB Code for RCR Parameter Estimation

```
clc
close all
clear all
res_scale = 1.7;
ratio = 0.05;
cap_scale = 1.4;
R = ratio*res_scale*1410.70732449662; % Input params
Rd = (1-ratio)*res_scale*1410.70732449662;
C = cap_scale*1150e-6;
tau = Rd*C;
p0 =0*1333; %initial pressure
T = 1.43; % Cardiac cycle time
load aor_flow
load LV_press.mat
Q = aor_flow(:,2);
Q=Q';
Q = Q*1;
t = 0:T/1000:T;
Pd = pchip(lvp(:,1),lvp(:,2),t);
Pd = Pd*0;
p = zeros(1001,1);
p(1) = p0;
for k=1:10
for i=2:1001
```

```
  tbar = t(1:i);
  Qtemp = Q(1:i);
  Qconv = exp(-(t(i) - tbar)/tau).*Qtemp/C;
  Qconv_integral = trapz(tbar,Qconv);
  p(i) = (p(1) - R*Q(1)-Pd(1))*exp(-t(i)/tau) + R*Q(i) + Pd(i) + Qconv_integral;
%   Pd(i)
end
p(1) = p(end);
end
plot(t(2:1001),p(2:1001)/1333);
fid = fopen('aor_press','w');
fprintf(fid,'%7.4f\n',p);
fclose(fid);
A1 = 1.58;
A2 = 0.70944;
A3 = 0.3433;
A4 = 0.4563;
A = A1 + A2 + A3 + A4;
R1 = A/A1*R;
R2 = A/A2*R;
R3 = A/A3*R;
R4 = A/A4*R;
Rd1 = A/A1*Rd;
Rd2 = A/A2*Rd;
Rd3 = A/A3*Rd;
```

```
Rd4 = A/A4*Rd;

C1 = A1/A*C;

C2 = A2/A*C;

C3 = A3/A*C;

C4 = A4/A*C;

fp = fopen('rcrt.dat','w');

fprintf(fp,'2\n');

fprintf(fp,'2\n');

fprintf(fp,'%f\n',R1);

fprintf(fp,'%f\n',C1);

fprintf(fp,'%f\n',Rd1);

fprintf(fp,'0.000000 0.000000\n');

fprintf(fp,'1.000000 0.000000\n');

fprintf(fp,'2\n');

fprintf(fp,'%f\n',R2);

fprintf(fp,'%f\n',C2);

fprintf(fp,'%f\n',Rd2);

fprintf(fp,'0.000000 0.000000\n');

fprintf(fp,'1.000000 0.000000\n');

fprintf(fp,'2\n');

fprintf(fp,'%f\n',R3);

fprintf(fp,'%f\n',C3);

fprintf(fp,'%f\n',Rd3);

fprintf(fp,'0.000000 0.000000\n');

fprintf(fp,'1.000000 0.000000\n');
```

```
fprintf(fp,'2\n');
fprintf(fp,'%f\n',R4);
fprintf(fp,'%f\n',C4);
fprintf(fp,'%f\n',Rd4);
fprintf(fp,'0.000000 0.000000\n');
fprintf(fp,'1.000000 0.000000\n');
% figure(2)
% plot(t(2:1001),Q(2:1001))
% load p_cor.mat
% J = 0;
% for i=2:101
%     J = J + 1/100*(p_cor(i)-p(i))^2;
% end
```

Coronary Boundary Condition

In the finite element solver, the coronary boundary condition couples the pressure P(t) with the flow rate Q(t) at the coronary outlet boundaries through the following equation using the coupled multi-domain method of Vignon et al[20]

$$P(t) = (RQ(t) + \int_0^t e^{\lambda_1 (t-s)} Z_1 Q(s)ds) - \int_0^t e^{\lambda_2 (t-s)} Z_2 Q(s)ds + (Ae^{\lambda_1 t} - Be^{\lambda_2 t})$$

$$+(\int_0^t e^{\lambda_1 (t-s)} Y_1 P_{im}(s)ds - \int_0^t e^{\lambda_2 (t-s)} Y_2 P_{im}(s)ds)$$

where

$$\lambda_1 = \frac{-p_1 + \sqrt{p_1^2 - 4p_0p_2}}{2p_2}$$

$$\lambda_2 = \frac{-p_1 - \sqrt{p_1^2 - 4p_0p_2}}{2p_2}$$

$$A = \frac{-1}{\sqrt{p_1^2 - 4p_0p_2}}[(q_2\lambda_1 + q_1)Q(0) + q_2\frac{dQ}{dt}(0) + b_1P_{im}(0) + p_2(\lambda_2P(0) - \frac{dP}{dt}(0))]$$

$$B = \frac{-1}{\sqrt{p_1^2 - 4p_0p_2}}[(q_2\lambda_2 + q_1)Q(0) + q_2\frac{dQ}{dt}(0) + b_1P_{im}(0) + p_2(\lambda_1P(0) - \frac{dP}{dt}(0))]$$

$$R = \frac{q_2}{p_2}$$

$$Z_1 = \frac{q_2\lambda_1^2 + q_1\lambda_1 + q_0}{\sqrt{p_1^2 - 4p_0p_2}}$$

$$Z_2 = \frac{q_2\lambda_2^2 + q_1\lambda_2 + q_0}{\sqrt{p_1^2 - 4p_0p_2}}$$

$$Y_1 = \frac{b_1\lambda_1 + b_0}{\sqrt{p_1^2 - 4p_0p_2}}$$

$$Y_2 = \frac{b_1\lambda_2 + b_0}{\sqrt{p_1^2 - 4p_0p_2}}$$

$$p_0 = 1$$

$$p_1 = R_{a-micro}C_a + (R_V + R_{V-micro})(C_a + C_{im})$$

$$p_2 = C_aC_{im}R_{a-micro}(R_V + R_{V-micro})$$

$$q_0 = R_a + R_{a-micro} + R_V + R_{V-micro}$$

$$q_1 = R_aC_a(R_{a-micro} + R_V + R_{V-micro}) + C_{im}(R_a + R_{a-micro})(R_V + R_{V-micro})$$

$$q_2 = C_aC_{im}R_aR_{a-micro}(R_V + R_{V-micro})$$

$$b_0 = 0$$

$$b_1 = C_{im}(R_V + R_{V-micro})$$

MATLAB Code for Coronary Parameter Estimation

```
clc

clear all

load Pim.mat

load aor_press

res_scale = 1.55;

cap_scale_cim = 3;

cap_scale_ca = 0.8;

Q_scale = 1.0;

A1 = 0.0164;

A2 = 0.0102;

A3 = 0.011;

A4 = 0.025;

A = A1 + A2 + A3 + A4;

Ra = res_scale*12.6e3;

Ramicro = res_scale*20.55e3;

Rv = res_scale*7.2e3;

Ca = cap_scale_ca*4.44e-6;

Cim = cap_scale_cim*37.6e-6;

p2 = Ca*Cim*Ramicro*Rv;

p1 = Ramicro*Ca +Rv*(Ca+Cim);

p0 = 1;

q2 = Ca*Cim*Ra*Ramicro*Rv;

q1 = Ra*Ca*(Ramicro+Rv)+Cim*(Ra+Ramicro)*Rv;

q0 = Ra+Ramicro+Rv;
```

```
b2 = 0;

b1 = Cim*Rv;

b0 = 0;

n=10000;

k=n/1000;

Q = zeros(1,n-2);

Plv = ones(1,n);

for i=1:k

   for j=1:1000

       P(1000*(i-1)+j) = aor_press(j);

       Plv(1000*(i-1)+j) = Pim(j,2);

   end

end

cardiac_cycle_period = 1.000;

dt = cardiac_cycle_period/1000;

t_final = n*dt;

t = 0:dt:t_final-3*dt;

for i=1:n-1

   dPdt(i) = (P(i+1)-P(i))/dt;

   dPlvdt(i) = (Plv(i+1)-Plv(i))/dt;

end

for i=1:n-2

   d2Pdt2(i) = (dPdt(i+1)-dPdt(i))/dt;

   d2Plvdt2(i) = (dPlvdt(i+1)-dPlvdt(i))/dt;

end
```

```
Qini = 0.1;
Q(1) = Qini;
G = -30; %dp/dt (t =0)
for i=1:n-2
   f(i) = p2*d2Pdt2(i) + p1*dPdt(i) + p0*P(i) - b2*d2Plvdt2(i) - b1*dPlvdt(i) - b0*Plv(i);
end
for i=1:n-3
   if i == 1
      Q(i+1)=(f(i)-(q0-2*q2/(dt*dt))*Q(i)+G*dt*(q2/(dt*dt)-q1/(2*dt)))/(2*q2/(dt*dt));
   else
      Q(i+1)=(f(i)-(q0-2*q2/(dt*dt))*Q(i)-(q2/(dt*dt)-q1/(2*dt))*Q(i-1))/(q2/(dt*dt)+q1/(2*dt));
   end
end
figure(1)
plot(t,Q)
figure(2)
plot(t(8001:9001) - 8*cardiac_cycle_period,Q(8000:9000))
total_lca_flow=trapz(0:cardiac_cycle_period/1000:cardiac_cycle_period,(Q(8000:9000)))
cor_flow = Q(8000:9000);
for i=1:4
   area(i) = 0;
end
area(1) = A1; area(2) = A2; area(3) = A3; area(4) = A4;
```

```
for i=1:4
   Ra(i) = (A/area(i))*res_scale*12.6e3;
   Ramicro(i)=(A/area(i))*res_scale*20.55e3;
   Rv(i) = (A/area(i))*res_scale*7.2e3;
   Ca(i) = (area(i)/A)*cap_scale_ca*4.44e-6;
   Cim(i) = (area(i)/A)*cap_scale_cim*37.6e-6;
   p2(i) = Ca(i)*Cim(i)*Ramicro(i)*Rv(i);
   p1(i) = Ramicro(i)*Ca(i) +Rv(i)*(Ca(i)+Cim(i));
   p0(i) = 1;
   q2(i) = Ca(i)*Cim(i)*Ra(i)*Ramicro(i)*Rv(i);
   q1(i) = Ra(i)*Ca(i)*(Ramicro(i)+Rv(i))+Cim(i)*(Ra(i)+Ramicro(i))*Rv(i);
   q0(i) = Ra(i)+Ramicro(i)+Rv(i);
   b2(i) = 0;
   b1(i) = Cim(i)*Rv(i);
   b0(i) = 0;
end
save cor_flow cor_flow
left_ventricular_pressure = [Pim(:,1)';Pim(:,2)'];
fp = fopen('cort_lca.dat','w');
fprintf(fp,'1001\n');
for i=1:4
   fprintf(fp,'1001\n');
   fprintf(fp,'%f\n',q0(i));
   fprintf(fp,'%f\n',q1(i));
   fprintf(fp,'%f\n',q2(i));
```

```
    fprintf(fp,'%f\n',p0(i));
    fprintf(fp,'%f\n',p1(i));
    fprintf(fp,'%f\n',p2(i));
    fprintf(fp,'%f\n',b0(i));
    fprintf(fp,'%f\n',b1(i));
    fprintf(fp,'%f\n',b2(i));
    fprintf(fp,'0\n');
    fprintf(fp,'100\n');
    fprintf(fp,'%1.15f %f\n',left_ventricular_pressure);
end
TT = linspace(0,cardiac_cycle_period,1001);
systole_lca = trapz(TT(1:331),Q(8000:8330));
diastole_lca = trapz(TT(332:1001),Q(8331:9000));
lca_systole_flow_percent = systole_lca/diastole_lca*100
```

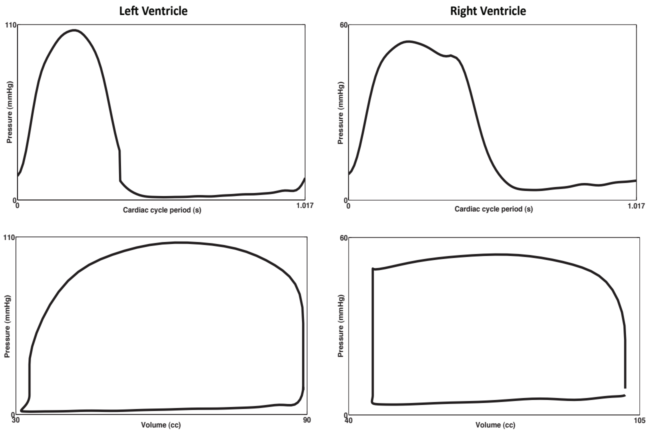

Figure A1: Left ventricular pressure (top left), right ventricular pressure (top right), left ventricular pressure-volume loop (bottom left) and right ventricular pressure-volume loop (bottom right)

Appendix II:

Equations for Cumulative Exposure Time (CET)

For an isotropic tetrahedral mesh, CET is computed at each element e based on the following equation

$$CET_e = \frac{1}{N_t V_e} \sum_{p=1}^{N_t} \int_0^{\infty} H_e^p(t)dt$$

V_e is the volume of the tetrahedral element e

N_t is the total number of particles released in the domain

$$H_e^p(t) = \begin{cases} 1\, if\ \ particle\ \ p\ is\ inside\ element\ e \\ 0\ otherwise \end{cases}$$

In the case of an anisotropic mesh, as in the present study, CET is scaled with the average length of the tetrahedral elements, and the volume V_e is replaced by the cube root of V_e.

To achieve adequate resolution in the CET computation, particle tracking was performed with over 10 million particles in the right and the left coronary arteries in each cardiac cycle. Particles were released once at the start of simulation, and particle tracking continued until all the particles were washed from the domain

References

1. Burns JC, Glode MP. Kawasaki syndrome. *Lancet*. 2004;364:533-544

2. Holman RC, Belay ED, Christensen KY, Folkema AM, Steiner CA, Schonberger LB. Hospitalizations for kawasaki syndrome among children in the united states, 1997-2007. *Pediatric Infectious Disease Journal*. 2010;29:483-488

3. Nakamura Y, Yashiro M, Uehara R, Sadakane A, Chihara I, Aoyama Y, Kotani K, Yanagawa H. Epidemiologic features of kawasaki disease in japan: Results of the 2007-2008 nationwide survey. *Journal of Epidemiology*. 2010;20:302-307

4. Wilder MS, Palinkas LA, Kao AS, Bastian JF, Turner CL, Burns JC. Delayed diagnosis by physicians contributes to the development of coronary artery aneurysms in children with kawasaki syndrome. *Pediatric Infectious Disease Journal*. 2007;26:256-260

5. Kato H, Sugimura T, Akagi T, Sato N, Hashino K, Maeno Y, Kazue T, Eto G, Yamakawa R. Long-term consequences of kawasaki disease - a 10- to 21-year follow-up study of 594 patients. *Circulation*. 1996;94:1379-1385

6. Newburger JW, Takahashi M, Beiser AS, Burns JC, Bastian J, Chung KJ, Colan SD, Duffy CE, Fulton DR, Glode MP, Mason WH, Meissner HC, Rowley AH, Shulman ST, Reddy V, Sundel RP, Wiggins JW, Colton T, Melish ME, Rosen FS. A single intravenous-infusion of gamma-globulin as compared with 4 infusions in the treatment of acute kawasaki syndrome. *New England Journal of Medicine*. 1991;324:1633-1639

7. Gordon JB, Kahn AM, Burns JC. When children with kawasaki disease grow up myocardial and vascular complications in adulthood. *Journal of the American College of Cardiology*. 2009;54:1911-1920

8. Newburger JW, Takahashi M, Gerber MA, Gewitz MH, Tani LY, Burns JC, Shulman ST, Bolger AF, Ferrieri P, Baltimore RS, Wilson WR, Baddour LM, Levison ME, Pallasch TJ, Falace DA, Taubert KA. Diagnosis, treatment, and long-term management of kawasaki disease - a statement for health professionals from the committee on rheumatic fever, endocarditis and kawasaki disease, council on cardiovascular disease in the young, american heart association. *Circulation*. 2004;110:2747-2771

9. Samada K, Shiraishi H, Sato A, Momoi MY. Grown-up kawasaki disease patients who have giant coronary aneurysms. *World Journal of Pediatrics*. 2010;6:38-42

10. Shadden SC, Taylor CA. Characterization of coherent structures in the cardiovascular system. *Annals of Biomedical Engineering*. 2008;36:1152-1162

11. Yang W, Feinstein JA, Shadden SC, Vignon-Clementel IE, Marsden AL. Optimization of a y-graft design for improved hepatic flow distribution in the fontan circulation. *Journal of biomechanical engineering*. 2013;135:011002-011002

12. Marsden AL, Bernstein AJ, Reddy VM, Shadden SC, Spilker RL, Chan FP, Taylor CA, Feinstein JA. Evaluation of a novel y-shaped extracardiac fontan baffle using computational fluid dynamics. *J Thorac Cardiovasc Surg*. 2009;137:394-U187

13. Yang W, Feinstein JA, Marsden AL. Constrained optimization of an idealized y-shaped baffle for the fontan surgery at rest and exercise. 2010

14. Bazilevs Y, Gohean JR, Hughes TJR, Moser RD, Zhang Y. Patient-specific isogeometric fluid-structure interaction analysis of thoracic aortic blood flow due to implantation of the jarvik 2000 left ventricular assist device. *Computer Methods in Applied Mechanics and Engineering*. 2009;198:3534-3550

15. Sankaran S, Moghadam ME, Kahn AM, Tseng EE, Guccione JM, Marsden AL. Patient-specific multiscale modeling of blood flow for coronary artery bypass graft surgery. *Annals of Biomedical Engineering*. 2012;40:2228-2242

16. Les AS, Shadden SC, Figueroa CA, Park JM, Tedesco MM, Herfkens RJ, Dalman RL, Taylor CA. Quantification of hemodynamics in abdominal aortic aneurysms during rest and exercise using magnetic resonance imaging and computational fluid dynamics. *Annals of Biomedical Engineering*. 2010;38:1288-1313

17. Ford MD, Stuhne GR, Nikolov HN, Habets DF, Lownie SP, Holdsworth DW, Steinman DA. Virtual angiography for visualization and validation of computational models of aneurysm hemodynamics.24:1586-1592

18. Wang JJ, Parker KH. Wave propagation in a model of the arterial circulation. *Journal of Biomechanics*. 2004;37:457-470

19. Taylor CA, Vignon-Clementel IE, Figueroa CA, Jansen KE. Outflow boundary conditions for three-dimensional finite element modeling of blood flow and pressure in arteries. *Computer Methods in Applied Mechanics and Engineering*. 2006;195:3776-3796

20. Taylor CA, Figueroa CA, Vignon-Clementel IE, Jansen KE, Hughes TJR. A coupled momentum method for modeling blood flow in three-dimensional deformable arteries. *Computer Methods in Applied Mechanics and Engineering*. 2006;195:5685-5706

21. Rideout VC, Dick DE. Difference-differential equations for fluid flow in distensible tubes. *Ieee Transactions on Biomedical Engineering*. 1967;BM14:171-&

22. Formaggia L, Veneziani A. *Reduced and multiscale models for the human cardiovascular system*. 7th VKI Lecture Series on "Biological fluid dynamics"; 2003

23. Formaggia L, Quarteroni A, Veneziani A. *Cardiovascular mathematics*. 2009.

24. Sagawa K, Lie RK, Schaefer J. Translation of frank,otto paper the basic shape of the arterial pulse - 1st treatise - mathematical-analysis - translators introduction. *Journal of Molecular and Cellular Cardiology*. 1990;22:253-254

25. Vignon-Clementel IE, Figueroa CA, Jansen KE, Taylor CA. Outflow boundary conditions for three-dimensional finite element modeling of blood flow and pressure in arteries. *Computer Methods in Applied Mechanics and Engineering*. 2006;195:3776-3796

26. De Pater L, Van Denberg J. An electrical analogue of the entire human circulatory system. *Med Electronics and Biol Engng*. 1964;2:161-166

27. Westerho.N, Bosman F, Devries CJ, Noorderg.A. Analog studies of human systemic arterial tree. *Journal of Biomechanics*. 1969;2:121-&

28. Whitehead KK, Pekkan K, Kitajima HD, Paridon SM, Yoganathan AP, Fogel MA. Nonlinear power loss during exercise in single-ventricle patients after the fontan - insights from computational fluid dynamics. 2007;116:I165-I171

29. Suga H, Sagawa K, Shoukas AA. Load independence of instantaneous pressure-volume ratio of canine left ventricle and effects of epinephrine and heart-rate on ratio. *Circulation Research*. 1973;32:314-322

30. Suga H, Sagawa K. Instantaneous pressure-volume relationships and their ratio in excised, supported canine left-ventricle. *Circulation Research*. 1974;35:117-134

31. Senzaki H, Chen CH, Kass DA. Single-beat estimation of end-systolic pressure-volume relation in humans - a new method with the potential for noninvasive application. *Circulation*. 1996;94:2497-2506

32. Kim HJ, Vignon-Clementel IE, Figueroa CA, LaDisa JF, Jansen KE, Feinstein JA, Taylor CA. On coupling a lumped parameter heart model and a three-dimensional finite element aorta model. *Annals of Biomedical Engineering*. 2009;37:2153-2169

33. Segers P, Stergiopulos N, Westerhof N, Wouters P, Kolh P, Verdonck P. Systemic and pulmonary hemodynamics assessed with a lumped-parameter heart-arterial interaction model. *Journal of Engineering Mathematics*. 2003;47:185-199

34. Kim HJ, Vignon-Clementel IE, Coogan JS, Figueroa CA, Jansen KE, Taylor CA. Patient-specific modeling of blood flow and pressure in human coronary arteries. *Annals of Biomedical Engineering*. 2010;38:3195-3209

35. Krams R, Sipkema P, Westerhof N. Varying elastance concept may explain coronary systolic flow impediment. *American Journal of Physiology*. 1989;257:H1471-H1479

36. Vis MA, Sipkema P, Westerhof N. Modeling pressure-area relations of coronary blood-vessels embedded in cardiac-muscle in diastole and systole. *American Journal of Physiology-Heart and Circulatory Physiology*. 1995;268:H2531-H2543

37. Vis MA, Sipkema P, Westerhof N. Modeling pressure-flow relations in cardiac muscle in diastole and systole. *American Journal of Physiology-Heart and Circulatory Physiology*. 1997;272:H1516-H1526

38. Wan J, Steele B, Spicer SA, Strohband S, Feijoo GR, Hughes TJR, Taylor CA. A one-dimensional finite element method for simulation-based medical planning for cardiovascular disease. *Computer methods in biomechanics and biomedical engineering*. 2002;5:195-206

39. Marsden A, Reddy V, Shadden S, Chan F, Taylor C, Feinstein J. A new multiparameter approach to computational simulation for fontan assessment and redesign. *Congenital Heart Disease*. 2010;5:104-117

40. Sundareswaran KS, Pekkan K, Dasi LP, Whitehead K, Sharma S, Kanter KR, Fogel MA, Yoganathan AP. The total cavopulmonary connection resistance: A significant impact on single ventricle hemodynamics at rest and exercise. *American Journal of Physiology-Heart and Circulatory Physiology*. 2008;295:H2427-H2435

41. Piccinelli M, Veneziani A, Steinman DA, Remuzzi A, Antiga L. A framework for geometric analysis of vascular structures: Application to cerebral aneurysms.28:1141-1155

42. Ku JP, Draney MT, Arko FR, Lee WA, Chan FP, Pelc NJ, Zarins CK, Taylor CA. In vivo validation of numerical prediction of blood flow in arterial bypass grafts. *Annals of Biomedical Engineering*. 2002;30:743-752

43. Dutta A, Tarbell JM. Influence of non-newtonian behavior of blood on flow in an elastic artery model. *Journal of Biomechanical Engineering-Transactions of the Asme*. 1996;118:111-119

44. LaDisa JF, Jr., Olson LE, Douglas HA, Warltier DC, Kersten JR, Pagel PS. Alterations in regional vascular geometry produced by theoretical stent implantation influence distributions of wall shear stress: Analysis of a curved coronary artery using 3d computational fluid dynamics modeling. *Biomedical Engineering Online*. 2006;5

45. Yang WG, Feinstein JA, Marsden AL. Constrained optimization of an idealized y-shaped baffle for the fontan surgery at rest and exercise. *Computer Methods in Applied Mechanics and Engineering*. 2010;199:2135-2149

46. Hundley WG, Lange RA, Clarke GD, Meshack BM, Payne J, Landau C, McColl R, Sayad DE, Willett DL, Willard JE, Hillis LD, Peshock RM. Assessment of coronary arterial flow and flow reserve in humans with magnetic resonance imaging. *Circulation*. 1996;93:1502-1508

47. Johnson KR, Patel SJ, Whigham A, Hakim A, Pettigrew RI, Oshinski JN. Three-dimensional, time-resolved motion of the coronary arteries. *Journal of Cardiovascular Magnetic Resonance*. 2004;6:663-673

48. Earls JP, Berman EL, Urban BA, Curry CA, Lane JL, Jennings RS, McCulloch CC, Hsieh J, Londt JH. Prospectively gated transverse coronary ct angiography versus retrospectively gated helical technique: Improved image quality and reduced radiation dose. *Radiology*. 2008;246:742-753

49. Dubini G, deLeval MR, Pietrabissa R, Montevecchi FM, Fumero R. A numerical fluid mechanical study of repaired congenital heart defects. Application to the total cavopulmonary connection (vol 29, pg 111, 1996). *Journal of Biomechanics*. 1996;29:839-839

50. Lagana K, Dubini G, Migliavacca F, Pietrabissa R, Pennati G, Veneziani A, Quarteroni A. Multiscale modelling as a tool to prescribe realistic boundary conditions for the study of surgical procedures. *Biorheology*. 2002;39:359-364

51. Sengupta D, Kahn AM, Burns JC, Sankaran S, Shadden SC, Marsden AL. Image-based modeling of hemodynamics in coronary artery aneurysms caused by kawasaki disease. *Biomechanics and Modeling in Mechanobiology*. 2012;11:915-932

52. Lonyai A, Dubin A, Feinstein J, Taylor C, Shadden S. New insights into pacemaker lead-induced venous occlusion: Simulation-based investigation of alterations in venous biomechanics. *Cardiovascular Engineering*. 2010;10:84-90

53. Schmidt JP, Delp SL, Sherman MA, Taylor CA, Pande VS, Altman RB. The simbios national center: Systems biology in motion. *Proceedings of the Ieee*. 2008;96:1266-1280

54. McCrindle BW, Li JS, Minich LL, Colan SD, Atz AM, Takahashi M, Vetter VL, Gersony WM, Mitchell PD, Newburger JW, Pediatric Heart N. Coronary artery involvement in children with kawasaki disease - risk factors from analysis of serial normalized measurements. *Circulation*. 2007;116:174-179

55. Sahni O, Jansen KE, Shephard MS, Taylor CA, Beall MW. Adaptive boundary layer meshing for viscous flow simulations. *Engineering with Computers*. 2008;24:267-285

56. Kung EO, Les AS, Figueroa CA, Medina F, Arcaute K, Wicker RB, McConnell MV, Taylor CA. In vitro validation of finite element analysis of blood flow in deformable models. *Annals of Biomedical Engineering*. 2011;39:1947-1960

57. Kung EO, Les AS, Medina F, Wicker RB, McConnell MV, Taylor CA. In vitro validation of finite-element model of aaa hemodynamics incorporating realistic outlet boundary conditions. *Journal of Biomechanical Engineering-Transactions of the Asme*. 2011;133

58. Courant R, Friedric.K, Lewy H. On partial difference equations of mathematical physics. *Ibm Journal of Research and Development*. 1967;11:215-&

59. Moghadam ME, Bazilevs Y, Hsia T-Y, Vignon-Clementel IE, Marsden AL, Modeling Congenital Hearts A. A comparison of outlet boundary treatments for prevention of backflow divergence with relevance to blood flow simulations. *Computational Mechanics*. 2011;48:277-291

60. Vignon-Clementel IE, Figueroa CA, Jansen KE, Taylor CA. Outflow boundary conditions for 3d simulations of non-periodic blood flow and pressure fields in deformable arteries. *Computer Methods in Biomechanics and Biomedical Engineering*. 2010;13

61. Bogren HG, Klipstein RH, Firmin DN, Mohiaddin RH, Underwood SR, Rees RSO, Longmore DB. Quantitation of antegrade and retrograde blood-flow in the human aorta by magnetic-resonance velocity mapping. *American Heart Journal*. 1989;117:1214-1222

62. Johnson K, Sharma P, Oshinski J. Coronary artery flow measurement using navigator echo gated phase contrast magnetic resonance velocity mapping at 3.0 t. *Journal of Biomechanics*. 2008;41:595-602

63. Marcus JT, Smeenk HG, Kuijer JPA. Flow profiles in the left anterior descending and the right coronary artery assessed by mr velocity quantification: Effects of through-plane and in-plane motion of the heart. *Journal of Computer Assisted Tomography*. 1999;23:567-576

64. Dewey FE, Rosenthal D, Murphy DJ, Froelicher VF, Ashley EA. Does size matter? Clinical applications of scaling cardiac size and function for body size. *Circulation*. 2008;117:2279-2287

65. Zamir M, Sinclair P, Wonnacott TH. Relation between diameter and flow in major branches of the arch of the aorta. *Journal of Biomechanics*. 1992;25:1303-1310

66. Ku DN, Giddens DP, Zarins CK, Glagov S. Pulsatile flow and atherosclerosis in the human carotid bifurcation - positive correlation between plaque location and low and oscillating shear-stress. *Arteriosclerosis*. 1985;5:293-302

67. Giannoglou GD, Soulis JV, Farmakis TM, Louridas GE. Wall shear stress in normal left coronary artery tree. *Journal of Biomechanics*. 2006;39:742-749

68. Gijsen FJH, Wentzel JJ, Thury A, Lamers B, Schuurblers JCH, Serruys PW, Van der Steen AF. A new imaging technique to study 3-d plaque and shear stress distribution in human coronar arter bifurcations in vivo. *Journal of Biomechanics*. 2007;40:2349-2357

69. Torii R, Keegan J, Wood NB, Dowsey AW, Hughes AD, Yang G-Z, Firmin DN, Thom SAM, Xu XY. Mr image-based geometric and hemodynamic investigation of the right coronary artery with dynamic vessel motion. *Annals of Biomedical Engineering*. 2010;38

70. Sriramarao P, Languino LR, Altieri DC. Fibrinogen mediates leukocyte-endothelium bridging in vivo at low shear forces. *Blood*. 1996;88:3416-3423

71. Kroll MH, Hellums JD, McIntire LV, Schafer AI, Moake JL. Platelets and shear stress. *Blood*. 1996;88:1525-1541

72. Passerini AG, Polacek DC, Shi CZ, Francesco NM, Manduchi E, Grant GR, Pritchard WF, Powell S, Chang GY, Stoeckert CJ, Davies PF. Coexisting proinflammatory and antioxidative endothelial transcription profiles in a disturbed flow region of the adult porcine aorta. *Proceedings of the National Academy of Sciences of the United States of America*. 2004;101:2482-2487

73. Hwang J, Ing MH, Salazar A, Lassegue B, Griendling K, Navab M, Sevanian A, Hsiai TK. Pulsatile versus oscillatory shear stress regulates nadph oxidase subunit expression - implication for native ldl oxidation. *Circulation Research*. 2003;93:1225-1232

74. Nagel T, Resnick N, Dewey CF, Gimbrone MA. Vascular endothelial cells respond to spatial gradients in fluid shear stress by enhanced activation of transcription factors. *Arteriosclerosis Thrombosis and Vascular Biology*. 1999;19:1825-1834

75. Nesbitt WS, Westein E, Tovar-Lopez FJ, Tolouei E, Mitchell A, Fu J, Carberry J, Fouras A, Jackson SP. A shear gradient-dependent platelet aggregation mechanism drives thrombus formation. *Nature Medicine*. 2009;15:665-U146

76. Wootton DM, Ku DN. Fluid mechanics of vascular systems, diseases, and thrombosis. *Annual Review of Biomedical Engineering*. 1999;1:299-329

77. Tanaka N, Naoe S, Masuda H, Ueno T. Pathological-study of sequelae of kawasaki-disease (mcls) - with special reference to the heart and coronary arterial lesions. *Acta Pathologica Japonica*. 1986;36:1513-1527

78. Johnston BM, Johnston PR, Corney S, Kilpatrick D. Non-newtonian blood flow in human right coronary arteries: Transient simulations. *Journal of Biomechanics*. 2006;39:1116-1128

79. Zhiliang X, Nan C, Kamocka MM, Rosen ED, Alber M. A multiscale model of thrombus development. *Journal of the Royal Society Interface*. 2008:705-722

80. Kaichi S, Tsuda E, Fujita H, Kurosaki K, Tanaka R, Naito H, Echigo S. Acute coronary artery dilation due to kawasaki disease and subsequent late calcification as detected by electron beam computed tomography. *Pediatric Cardiology*. 2008;29:568-573

81. Bazilevs Y, Hsu MC, Benson DJ, Sankaran S, Marsden AL. Computational fluid-structure interaction: Methods and application to a total cavopulmonary connection. *Computational Mechanics*. 2009;45:77-89

82. Baretta A, Corsini C, Yang W, Vignon-Clementel IE, Marsden AL, Feinstein JA, Hsia TY, Dubini G, Migliavacca F, Pennati G, Modeling Congenital Hearts A. Virtual surgeries in patients with congenital heart disease: A multi-scale modelling test case. *Philosophical Transactions of the Royal Society a-Mathematical Physical and Engineering Sciences*. 2011;369:4316-4330

83. Marsden AL, Vignon-Clementel IE, Chan FP, Feinstein JA, Taylor CA. Effects of exercise and respiration on hemodynamic efficiency in cfd simulations of the total cavopulmonary connection.35:250-263

84. Bazilevs Y, Hsu MC, Zhang Y, Wang W, Kvamsdal T, Hentschel S, Isaksen JG. Computational vascular fluid-structure interaction: Methodology and application to cerebral aneurysms. *Biomechanics and Modeling in Mechanobiology*. 2010;9:481-498

85. Cebral JR, Castro MA, Burgess JE, Pergolizzi RS, Sheridan MJ, Putman CM. Characterization of cerebral aneurysms for assessing risk of rupture by using patient-specific computational hemodynamics models. *American Journal of Neuroradiology*. 2005;26:2550-2559

86. Cebral JR, Castro MA, Appanaboyina S, Putman CM, Millan D, Frangi AF. Efficient pipeline for image-based patient-specific analysis of cerebral aneurysm hemodynamics: Technique and sensitivity. *Ieee Transactions on Medical Imaging*. 2005;24:457-467

87. Sankaran S, Marsden AL. The impact of uncertainty on shape optimization of idealized bypass graft models in unsteady flow. *Physics of Fluids*. 2010;22

88. Min J, Berman D, Shaw L, Mauri L, Koo B-K, Erglis A, Leipsic J. Fractional flow reserved derived from computed tomographic angiography (ffrct) for intermediate severity coronary lesions: Results from the defacto trial (determination of fractional flow reserve by anatomic computed tomographic angiography). *Journal of the American College of Cardiology*. 2012;60:B6-B6

89. Lagana K, Dubini G, Migliavacca F, Pietrabissa R, Pennati G, Veneziani A, Quarteroni A. Multiscale modelling as a tool to prescribe realistic boundary conditions for the study of surgical procedures. 2002:359-364

90. Whiting CH, Jansen KE, Dey S. Hierarchical basis for stabilized finite element methods for compressible flows. *Computer Methods in Applied Mechanics and Engineering*. 2003;192:5167-5185

91. Burattini R, Sipkema P, Vanhuis GA, Westerhof N. Identification of canine coronary resistance and intramyocardial compliance on the basis of the waterfall model. *Annals of Biomedical Engineering*. 1985;13:385-404

92. Ohkubo T, Fukazawa R, Ikegami E, Ogawa S. Reduced shear stress and disturbed flow may lead to coronary aneurysm and thrombus formations. *Pediatrics International*. 2007;49

93. Sankaran S, Marsden AL. A stochastic collocation method for uncertainty quantification and propagation in cardiovascular simulations. *Journal of Biomechanical Engineering-Transactions of the Asme*. 2011;133

94. Choi JH, Min JK, Labounty TM. Intracoronary transluminal attenuation gradient in coronary ct angiography for determining coronary artery stenosis (vol 4, pg 1149, 2011). *Jacc-Cardiovascular Imaging*. 2012;5:129-129

95. Shuman WP, Branch KR, May JM, Mitsumori LM, Lockhart DW, Dubinsky TJ, Warren BH, Caldwell JH. Prospective versus retrospective ecg gating for 64-detector ct of the coronary arteries: Comparison of image quality and patient radiation dose. *Radiology*. 2008;248:431-437

96. Sandhu R, Georgiou T, Tannenbaum A. A new distribution metric for image segmentation. *Proceedings of the SPIE - The International Society for Optical Engineering*. 2008;6914

97. Rao CR, Chakraborty R. Handbook of statistics vol. 8. Statistical methods in biological and medical sciences. *Rao, C. R. and R. Chakraborty (Ed.). Handbook of Statistics, Vol. 8. Statistical Methods in Biological and Medical Sciences. Xvi+554p. Elsevier Science Publishers B.V.: Amsterdam, Netherlands; (Dist. in the USA and Canada by Elsevier Science Publishing Co., Inc.: New York, New York, USA). Illus*. 1991:XVI+554P-XVI+554P

98. Komarek P, Moore AW. Making logistic regression a core data mining tool with tr-irls. *Proceedings. Fifth IEEE International Conference on Data Mining*. 2006:4 pp.-4 pp.